5-2013

EMPLACEMENT MECHANISMS AND MAGMA DRIVING PRESSURE OF THE PROTEROZOIC CURECANTI PLUTON; THE BLACK CANYON OF THE GUNNISON, COLORADO

Gordon Leonard Hicks
The University of Tennessee, Knoxville, ghicks2@utk.edu

To the Graduate Council:

I am submitting herewith a thesis written by Gordon Leonard Hicks entitled "EMPLACEMENT MECHANISMS AND MAGMA DRIVING PRESSURE OF THE PROTEROZOIC CURECANTI PLUTON; THE BLACK CANYON OF THE GUNNISON, COLORADO." I have examined the final electronic copy of this thesis for form and content and recommend that it be accepted in partial fulfillment of the requirements for the degree of Master of Science, with a major in Geology.

Micah J. Jessup, Major Professor

We have read this thesis and recommend its acceptance:

Robert D. Hatcher Jr., Harry Y. McSween

Accepted for the Council:
Dixie L. Thompson

Vice Provost and Dean of the Graduate School

(Original signatures are on file with official student records.)

EMPLACEMENT MECHANISMS AND MAGMA DRIVING PRESSURE OF THE PROTEROZOIC CURECANTI PLUTON; THE BLACK CANYON OF THE GUNNISON, COLORADO

A Thesis Presented for the
Master of Science
Degree
The University of Tennessee, Knoxville

Gordon Leonard Hicks
May 2013

DEDICATION

To Kali

For all the spark;

To Annie

For finding me in the dark;

To Jamey

For the massive head start

ACKNOWLEDGEMENTS

The ideas presented in this paper have benefitted significantly from many discussions with James V. Jones III. Field assistance was provided by Remy Leger during summer 2010. Sources of funding for this research included the Geological Society of America, Four Corners Geological Society, Tobacco Root Geologic Society, and The University of Tennessee – Earth and Planetary Sciences Swingle Award, several graduate teaching assistantships, and a graduate research assistantship. I would like to thank my committee members, Dr. Robert D. Hatcher, Jr. and Dr. Harry Y. McSween, for providing critical feedback and revisions. I thank Dr. Micah J. Jessup for his patience, understanding, and insights regarding structural geology and life. Kyle White, Tim Diedesch, and Remy Leger provided edits, clarifications, and ideas regarding the structural models presented in this thesis. Ken Stahlnecker was instrumental in providing access to the Black Canyon of the Gunnison National Park and the Curecanti National Recreation Area for field work. Sue Newman of Sister Kenny provided belief and encouragement in the spaces between, and Liz Lee provided PBR and R&R on the other side of the country. There are obviously far too many individuals and groups to properly acknowledge, but please know that your thoughts, efforts, and love is recognized and appreciated.

ABSTRACT

There is significant obliquity between the margins of the Curecanti pluton, an internal foliation, a coeval swarm of ~400 pegmatite dikes just west of the pluton, and the host rock foliation. This pluton is a 5 km-long, 3 km-wide, and 0.4 km-thick sheet of monzogranite exposed in the Black Canyon of the Gunnison, CO. The pluton is discordant along most of its length, but has a >100-m-thick root at its western margin subparallel to the foliation in the host rock gneisses. A cordierite + anthophyllite + staurolite + garnet schist from the Vernal Mesa pluton aureole was previously dated (1.4 Ga) and indicates emplacement occurred at 600*C [degrees C] ± [plus or minus] 50*C and 300 ± 100 MPa. We present evidence that indicates emplacement of the Curecanti pluton, 25 kilometers-southeast of the Vernal Mesa pluton, may have occurred during similar conditions. The Vernal Mesa pluton was intruded subparallel to, and contemporaneous with movement on the NE-striking, subvertical Black Canyon shear zone. In contrast, Curecanti monzogranite was emplaced as a tongue-shaped sheet that tapers out in the hinge zone of the kilometer-scale F2 Curecanti antiform. The discordance between the pluton margins, an internal foliation, and the host rock foliation is contrary to observations of many other tabular granitoids worldwide that are emplaced parallel to host rock foliation and display a margin-parallel foliation. Three transects through the Curecanti pluton display evidence for solid-state foliation development localized in the pluton floor and in correlative dikes just beneath the pluton. Evidence for submagmatic flow is preserved near the roof of the pluton. Strain accumulated in the pluton at least 75 m above the floor, but did not result in the development of a foliation. The decoupling of wall-rock fabric and Curecanti pluton foliations, along with the presence of high-temperature quartz deformation mechanisms in the pluton, indicate high-temperature subsolidus deformation. In addition, Curecanti pluton geochemistry and magma driving pressure are evaluated to show that a combination of neutral buoyancy, depth to the magma source region, and a rheological impediment are necessary conditions to form this partly discordant peraluminous pluton.

TABLE OF CONTENTS

LIST OF TABLES

LIST OF FIGURES

FIGURE PAGE

LIST OF ATTACHMENTS

CHAPTER 1
INTRODUCTION AND STATEMENT OF PROBLEM

1.1 Granitoid emplacement controversy

1.1.1 Granite versus granitoid

While the term "granite" implies a specific composition of rock, and is often a misnomer, "granitoid" refers to any coarse-grained felsic rock, and is the preferred umbrella-term (Winter, 2001). The Earth's continental crust contains a great deal of granitoid rock that has remained stable and above sea level for several billion years (Taylor and McLennan, 1995). Large volumes of granitoid magma are extracted from and ascend through the lower crust to be emplaced at structurally higher levels, leaving behind a dehydrated and refractory lower crust (Petford et al., 2000). The four steps of this process – generation, segregation, ascent, and emplacement of melt – can be quantified volumetrically and temporally (Brown, 1994). In the past several decades, the focus of research regarding granitoids has built on the foundation of these geochemical studies to addresses the four physical processes listed above. This shift has resulted in the recognition of granitoid magmatism not as a slow equilibrium process operating on timescales of millions of years, but as a dynamic process often occurring on timescales of months to centuries (Tikoff and Vigneresse, 1999; Petford et al., 2000; Vigneresse and Clemens, 2000; Cruden and McCaffrey, 2000; Demartis et al., 2011).

Many plutons classically interpreted as diapirs which rose through the crust as hot Stokes bodies (Marsh, 1982) have been reevaluated, and their geometries and internal fabrics are now thought to have formed due to emplacement-related processes rather diapiric ascent (Ramsay, 1989). While diapirism still may be an important process in the lowermost crust (Miller and Paterson, 1999), diking and/or deformation-driven transport of flow are likely more viable mechanisms of melt transport in the middle and upper crust (Petford and Atherton, 1992; Petford et al., 1993).

1.1.2 Diking

Diking refers to magma ascending, usually vertically, through fractures in elastic rock along the plane parallel to the maximum compressive principal stress direction (σ_1, which is vertical during a lithostatic-stress state and extension; Lister and Kerr, 1991; Vigneresse et al., 1999). Because of this, vertical diking, sensu stricto, is inhibited during local shortening and assisted during extension (Brown and Solar, 1999). Though Zoback and Zoback (1980) showed one principal stress to be vertical in the upper ~15 kilometers of the crust within both shortening and extending regions, the dynamic nature of stress means that local tensional environments can develop during regional shortening, and vice-versa (Means, 1976; Tikoff and Teyssier, 1992). It is a well-established phenomenon that favorably oriented fractures (i.e. Griffith cracks) can develop a tensional stress even during an applied compressive stress (McClintock and Walsh, 1962). A diking model was described by Clemens and Mawer (1992), based on the previously established ideas of Pollard (1973), as an alternative to diapirism in which the low tensile strength of rocks is exploited by magmas. If one principal stress in the crust is vertical in both tensional and compressional regions (Zoback and Zoback, 1980), vertical fractures filled with granitoid magma will self-propagate and rise to their level of neutral buoyancy (Clemens and Mawer, 1992; Hogan et al., 1998). Clemens and Mawer (1992) show that the same dike widths commonly observed and mapped in the field (1-3-m-thick) can feed a pluton one order of magnitude smaller than the Curecanti pluton in under a century. One problem with the dike model for granitoid ascent and subsequent growth of large batholiths includes a lack of observed 1-3-m-thick dikes filled with granitoid material which feed into granitoid plutons (Clemens and Mawer, 1992; Brown and Solar, 1999). A mechanism that may compliment, rather than contradict, dike models is deformation-assisted and focused ascent of granitoids.

1.1.3 Deformation

Granitoids are often spatially and temporally associated with lithosphere-scale shortening (Karlstrom, 1989; Brown and Solar, 1998; Solar et al., 1998; Brown and McClelland, 2000; Davidson et al., 2007), despite the fact that diking should be inhibited

during shortening (Section 1.1.2). Due to this granitoid-tectonics correlation, some authors have suggested models in which melt is focused by deformation (Tikoff and Teyssier, 1992; Demartis et al., 2011), and that pluton geometry is in part controlled by regional deformation and ballooning of the pluton (Rosenberg et al., 1995). The deformation and/or displacement of wall rocks to make space for an incoming magma may be distributed broadly as either depression of the floor (Cruden, 1998), lifting of the roof (Grocott et al., 1999), or some combination of the two, though evidence may not be preserved of either process (Clemens and Mawer, 1992). Vertical redistribution of mass in the crust is important, albeit not always preserved, and it has long been recognized that magma is able to lift its roof rocks (i.e. a laccolith) at hypabyssal depths where lithostatic overburden is relatively low (Corry, 1988). However, lifting of roof rocks due to intrinsic magma pressure may occur deeper in the crust than previously thought possible; at least up to 7 km deep (McCaffrey, 1992; Benn et al., 1998; Brown and Solar, 1999; de Saint Blanquat et al., 2001; Wagner et al., 2006).

1.1.4 The search for a unified model

While there are convincing arguments for both diking and deformation as primary mechanisms for melt transport through the crust, Brown and Solar (1998) warn that each granitoid pluton should be considered individually regarding its ascent and emplacement mechanisms. However, Vigneresse et al. (1999) noticed 2 geometries which most plutons fall into: flat-floored pluton's with length:thickness ratios > 5 and one to many feeder zones, and wedge-shaped plutons with length:thickness ratios < 5 and a smaller number of feeder zones. The Vernal Mesa's interpreted geometry and Curecanti pluton's empirically-verified geometry fit into this schema as a wedge-shaped and a flat-floored pluton, respectively (Fig. 1-1). Flat-floored plutons are the result of dynamic principal stress orientations, and thus the opening plane orientation discussed by Clemens and Mawer (1992), which change due to the emplacement of vertical granitoid sheets (Vigneresse et al., 1999). Wedge-shaped plutons, in contrast, are interpreted to represent the infilling of a fracture-controlled dilatancy (Vigneresse et al., 1999).

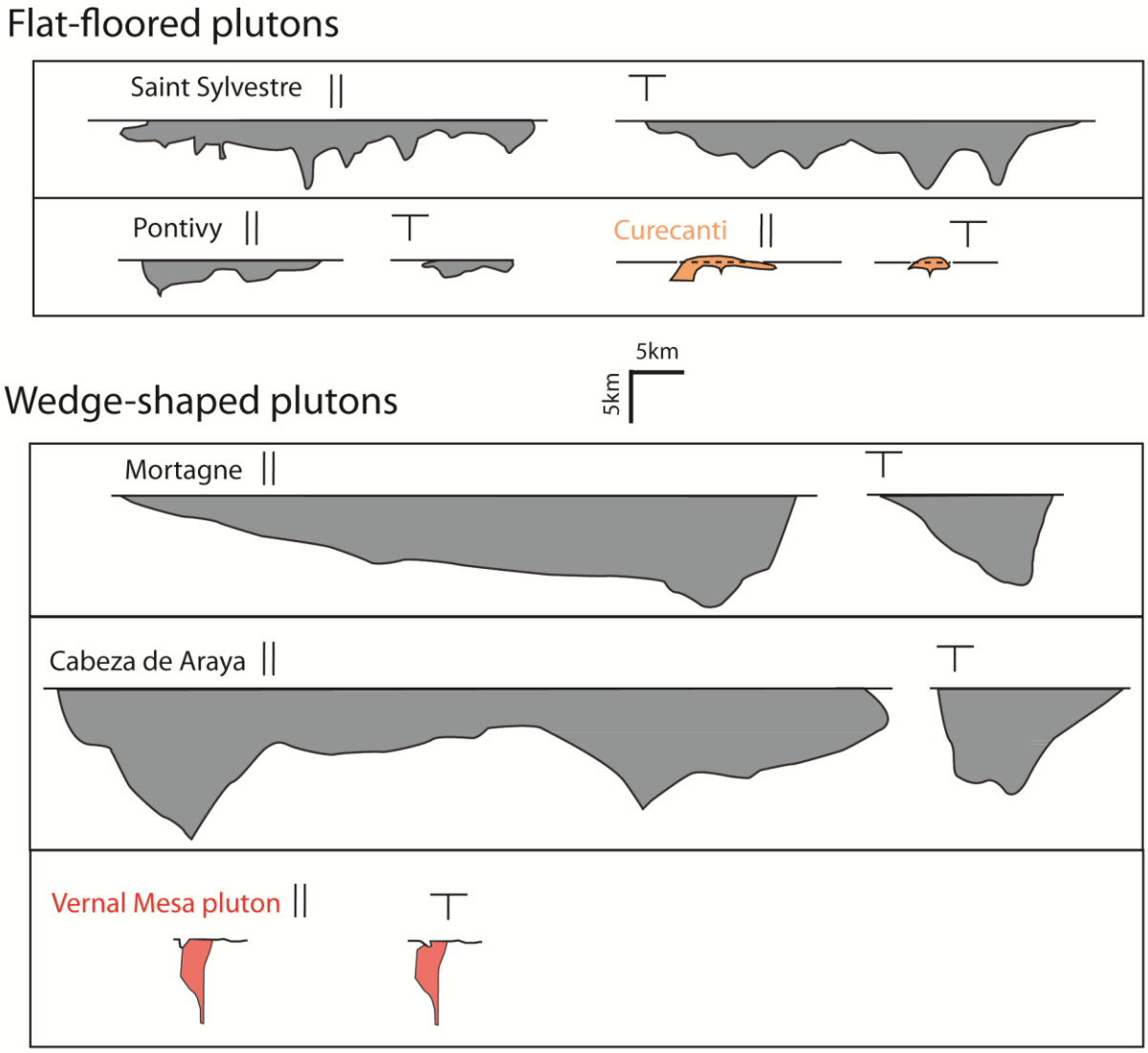

Figure 1-1. Bimodal pluton geometry adapted from Vigneresse et al. (1999) showing cross sections drawn perpendicular (T) and parallel (ll) to the long axis of several plutons. All plutons are drawn at the same scale. Although the Curecanti and Vernal Mesa plutons are relatively small compared to some of these European granitoids, Vigneresse et al. (1999) argued that pluton geometry is scale-invariant, and the two Black Canyon plutons fit nicely into the schema developed by those authors.

A dynamic model which considers both the importance of deformation and the role gravity plays on the ascent of felsic liquid through the crust should be the goal of any granitoid emplacement research. Results summarized in Section 7.6 demonstrate that, during a lithostatic state of stress, liquid Curecanti monzogranite (CMG) could not have ascended within a fracture from its source solely by buoyant forces resulting from differential density between the magma and brittle host rocks. Similarly, Menand (2011) recognized that buoyancy is likely not enough to determine the emplacement depth and mechanisms of many plutons, and instead called upon crustal heterogeneities, rigidity-contrasts between host rocks and infilling magma, and local and far-field stresses. Section 2.1 reviews the state of the lithosphere around the time of Curecanti pluton emplacement.

Furthermore, Miller et al. (2011) reviewed recent models which call upon incremental emplacement of plutons in sheets of crystal-rich host (i.e. crystal mush). These models argue that protracted growth of plutons by many granitoid replenishment events sets up the rigidity contrast responsible for arresting granitoid melts in the mid to upper crust.

1.2 Mesoproterozoic thermal event & controversy

1.2.1 Introduction

The Mesoproterozoic thermal event followed a protracted time of orogenic growth in much of Laurentia and Baltica (terms for Proterozoic assemblies from Whitmeyer and Karlstrom, 2007). This period is characterized by worldwide magmatism, considered "A-type," or anorogenic, due to igneous rocks of this time having high concentrations of high field strength elements, fluorine, and high Fe:Mg ratios (Anderson, 1983; Pearce et al., 1984; Anderson and Morrison, 2005). Compositional variability within the "1.4 Ga suite," discussed at length by Anderson and Morrison (2005), can be summarized by differences in the degree of alumina saturation and Fe-Ti oxide mineralogy. Three petrographic provinces have been identified based on the type of granitoid that typifies them: ilmenite, magnetite, and two-mica granitoids (Fig. 1-2). Long considered anorogenic in origin, their chemistry is interpreted to necessitate partial melting of preexisting Paleoproterozoic crust, mantle upwelling, underplating of the crust

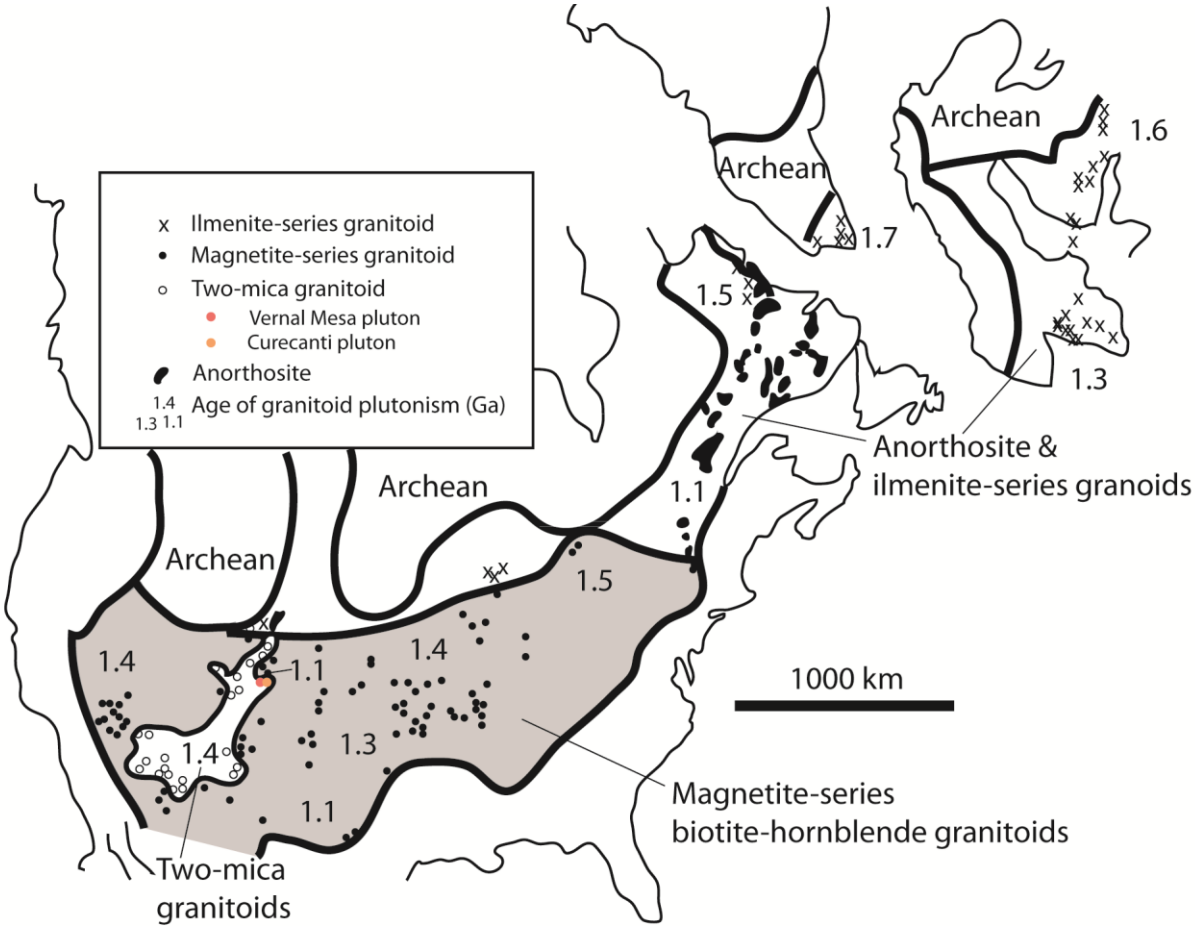

Figure 1-2. Distribution of Proterozoic intrusive rocks in North America and Scandinavia, highlighting the three petrographic provinces of Anderson and Morrison (2005), location of plutons (see *explanation* on figure), Archean crust (bold black lines), present day continental boundaries (thin black lines), and approximate ages of provinces (numbers). Modified from Anderson and Morrison (2005).

by tholeiitic material, and/or regional extension (Anderson, 1983; Hoffman, 1989; Frost and Frost, 1997; Ferguson et al., 2004). However, it is also recognized that some 1.4 Ga granitoids are spatially associated with lithosphere-scale shear zones (Nyman et al., 1994; Kirby et al., 1995; Jessup et al., 2005) and/or contain a pervasive solid-state foliation (Nyman et al., 1994; Ferguson et al., 2004). A recent surge of evidence for regional northwest-directed shortening at 1.4 Ga (Daniel and Pyle, 2006; Jones et al., 2010b; Jones et al., 2011; Andronicos et al., 2012; Aronoff et al., 2012b; Daniel et al., 2012) that is contemporaneous with the ferroan, alkalic magmatism ubiquitous at this time is a problem for the anorogenic model from a petrologic standpoint, because this geochemistry is associated with mantle-derived tholeiite in extensional or hotspot regions (Frost et al., 2001).

1.2.2 Mesoproterozoic: Orogeny or no orogeny?

Evidence for prograde metamorphism, shortening and transpressional structures, and reactivation of lithosphere-scale shear zones along the southern margin of Laurentia at 1.4 Ga continues to emerge (Graubard and Mattinson, 1990; Nyman et al., 1994; Shaw et al., 2001; Daniel and Pyle, 2006; Jones et al., 2010a; Jones et al., 2010b; Jones et al., 2011; Andronicos et al., 2012; Aronoff et al., 2012a, b; Lee et al., 2012; Daniel et al., 2013), though the petrologic conundrum discussed in Section 1.2.1 is still not resolved. Models that interpret 1.4 Ga foliated plutons as syntectonic usually call for a distal convergent plate boundary of unknown location and the transmission of compressive stresses (Nyman et al., 1994; Kirby et al., 1995; Amato et al., 2011). Royden (1996) pointed out that a weakened lower crust and relatively strong upper crust enable compressive stresses to be transmitted >1000 km from a plate boundary, resulting in an orogen with high average elevation but low relative relief (a plateau, sensu lato). During the Mesoproterozoic, the lower crust was weakened by the aforementioned 1.4 Ga magmatism (Shaw et al., 2005; Jones et al., 2010b), and thus allowed for the transmission of compressive stresses along a distal convergent boundary presently not exposed but likely beneath the poorly exposed Grenville province (Fig. 1-3). However, the lack of evidence for sedimentation which accompanied this "orogeny" was problematic until

Mesoproterozoic sediments with locally derived Paleoproterozoic protoliths in the Picuris Mountains of northern New Mexico were documented (Jones et al., 2011; Fig. 1-3). This, along with data (yet to be published in a peer-reviewed journal) from Aronoff et al. (2012b) and Daniel et al. (2013) suggesting prograde metamorphism in the southwestern US at 1.4 Ga, indicates the deformation observed in many 1.4 Ga rocks may indeed be the manifestation of an orogeny at this time. Future models that call for 1.4 Ga orogeny must reconcile the apparent contradiction of ferroan, alkalic magmatism with orogeny.

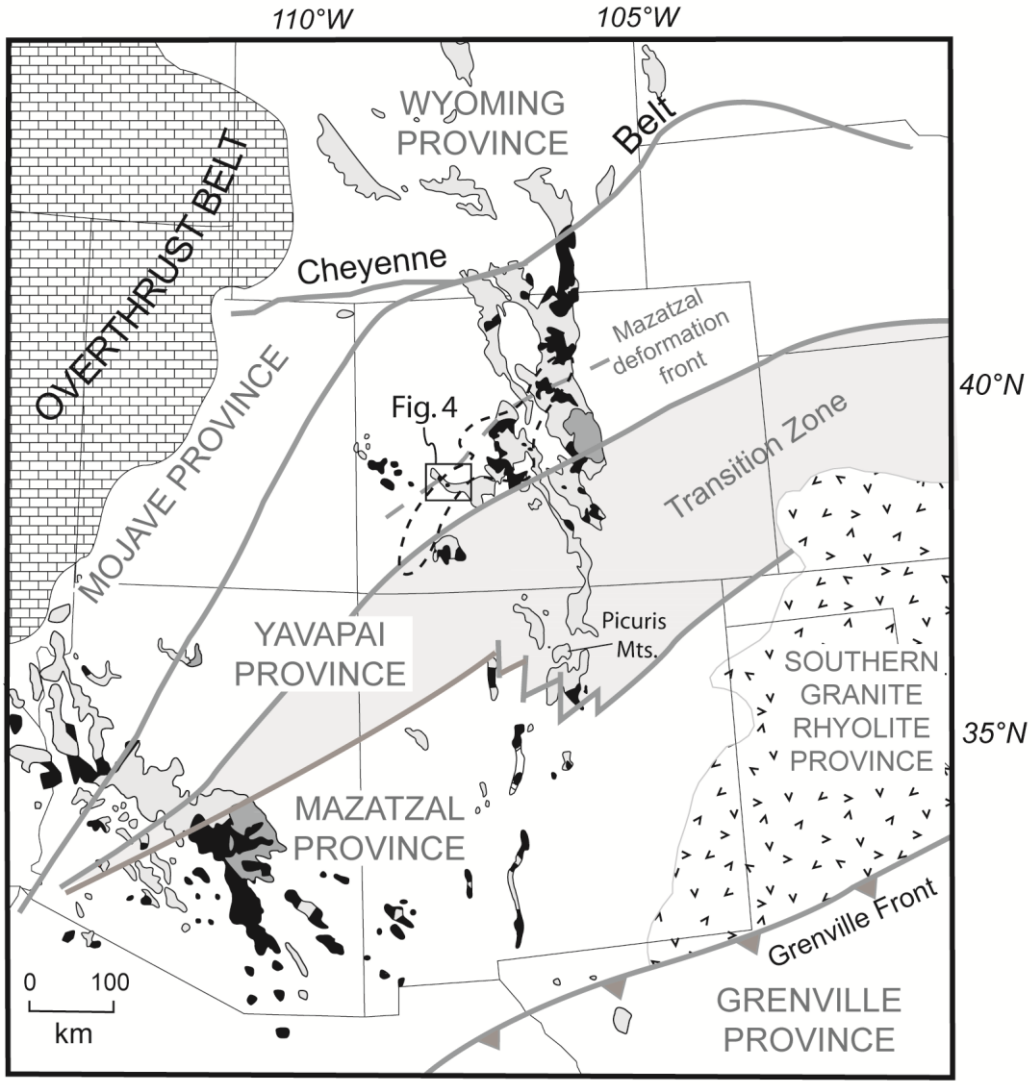

Figure 1-3. Regional geology context map using province nomenclature of Whitmeyer and Karlstrom (2007). Boundaries of Colorado mineral belt (black dashed line) from Tweto and Sims (1963). Proterozoic exposures are outlined in light gray, 1.4 Ga. plutons are black polygons, and 1.1 Ga. plutons are dark gray polygons. The extent of Mazatzal-age deformation is shown as the Mazatzal deformation front. Adapted from Jones et al. (2010).

CHAPTER 2
GEOLOGIC SETTING

2.1 Regional setting: Laurentia in the Proterozoic

Exposures of Precambrian rocks in the southwestern United States consist of a wide variety of metavolcanic, metasedimentary, and mafic and felsic igneous bodies formed and accreted to the southern margin of the Archean Wyoming province from 1.8-1.6 Ga (Condie, 1982; Karlstrom and Bowring, 1988; Reed et al., 1993). During this period of profound crustal growth (Whitmeyer and Karlstrom, 2007), Laurentia records southern margin growth of ~ 1300 kilometers through a series of episodic orogenies and accretion of new material (Bickford et al., 1982; Hoffman, 1989; Bowring and Karlstrom, 1990).

These Precambrian exposures have been divided into three provinces based on rock types and isotopic variation (Bennett and DePaolo, 1987). The Yavapai province is a collage of predominantly juvenile arc terranes with Nd model ages between 2.0-1.8 Ga and were mainly assembled between 1.78-1.70 Ga along a belt stretching from Arizona to Colorado and southern Wyoming (Fig. 1-3; Bennett and DePaolo (1987). A voluminous, post-orogenic magmatic event followed the Yavapai orogeny (Anderson and Cullers, 1999) as well as the unroofing of some regions and voluminous sedimentation (Jones et al., 2009). Southeast of the Yavapai province, the Mazatzal province consists of 1.8-1.7 Ga crust (Bennett and DePaolo, 1987; Bowring and Karlstrom, 1990) interpreted to have formed as continental margin arcs and back-arc supracrustal rocks outboard of the Yavapai province (Whitmeyer and Karlstrom, 2007). These arcs were assembled to the southern margin of the Yavapai province from 1.66-1.60 Ga during the Mazatzal orogeny (Karlstrom and Bowring, 1988; Shaw and Karlstrom, 1999; Amato et al., 2008; Amato et al., 2011). Deformation synchronous with this orogeny extends into present-day south-central Colorado (Shaw and Karlstrom, 1999), and the approximate northern limit of this deformation is represented by the Mazatzal deformation front (Fig. 1-3). After a 150 million year tectonic lull, Laurentia records further south-directed growth during the Mesoproterozoic. The growth is recorded in the Grenville province, a large province with

Nd model ages of 1.5-1.3 Ga extending from Mexico to Labrador (Fig. 1-3; Bennett and DePaolo, 1987; Karlstrom et al., 2001). Following the assembly and accretion of the Grenville province, a large number of granitoid plutons, mafic dikes, and regional high-temperature, low-pressure metamorphism occurred throughout the southwestern United States between 1.47-1.36 Ga (Reed et al., 1993; Williams et al., 1999). Rocks of this age account for nearly 20% of Precambrian exposures in this region (Fig. 1-3).

The model of episodic juvenile arc accretion punctuated by voluminous bimodal magmatism, summarized by Whitmeyer and Karlstrom (2007), is slightly problematic due to zircon ages and Hf isotopic data which may suggest Archean crust was involved (Bickford et al., 2008). If outboard juvenile arc formation and accretion during episodic orogenies does not adequately explain Precambrian exposures in the southwestern US, rifting is usually called upon to produce the bimodal magmatism and pluton compositions presently exposed (Bickford et al., 2008). Alternative models are still being evaluated and debated (Bickford and Hill, 2007; Duebendorfer, 2007; Karlstrom et al., 2007).

2.2 Black Canyon geology

2.2.1 Introduction

The Black Canyon of the Gunnison region in southwestern Colorado provides a ~100 kilometer-long transect of exposed Proterozoic rocks (Figs. 2-1 and 2-2; Hansen and Peterman, 1968; Hansen, 1971; Jessup et al., 2006; Jessup et al., 2005). Metasedimentary rocks are the dominant lithology in the Black Canyon area (Black Canyon succession, 1740-1730 Ma), whereas the metavolcanic Dubois and Cochetopa succession (1770-1960 Ma; Condie, 1982) dominate the eastern portion of the transect (Fig. 2-1). The contact between the two successions is a sheared zone of interlayered volcanics and sediment (Olson and Hedlund, 1973) suggested to have originally been

Figure 2-1. Generalized geologic map (modified from Jessup et al., 2005) of the Black Canyon and Dubois successions (Hedlund and Olson, 1973, 1974, 1976; Hansen, 1971, 1972), axial traces of F_2 folds, trace of S_2 foliation, and location of intrusive rocks (warm colors). Inset cartoon map (lower left) shows the present-day geometry, while the map reconstructs the geometry prior to strike-slip motion on the Red Rocks fault. Inset i. shows Colorado reference map. Inset ii. shows location of Figure 3-1. Black star shows location of sample MJBC-43 used by Jessup et al. (2005) for a pressure temperature estimate (Section 2.2.3 of text). Geochronology from Bickford et al. (1989).

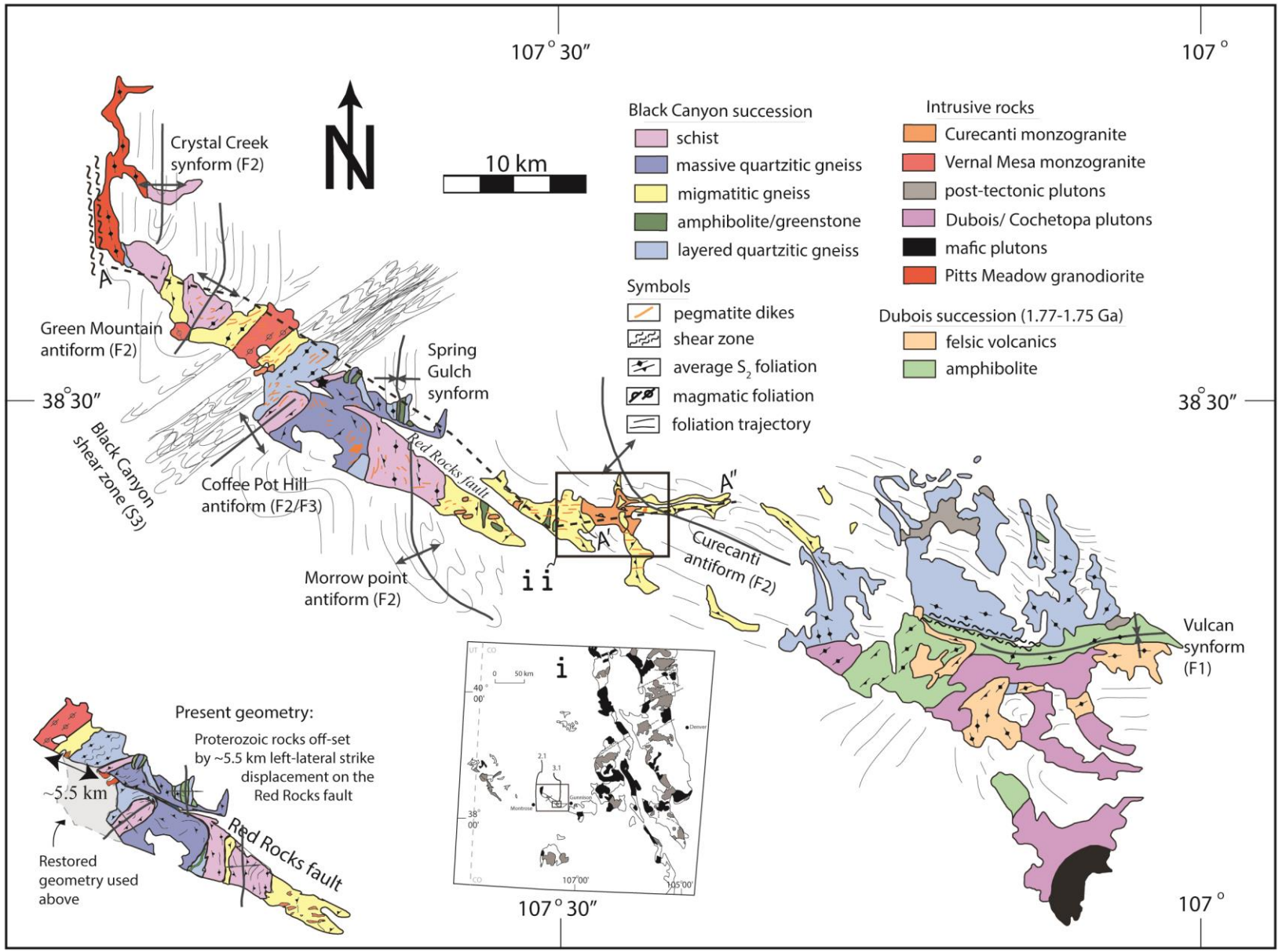
107° 30″
107°
38°30″
Crystal Creek synform (F2)
Green Mountain antiform (F2)
Spring Gulch synform
Black Canyon shear zone (S3)
Coffee Pot Hill antiform (F2/F3)
Red Rocks fault
Morrow point antiform (F2)
Curecanti antiform (F2)
Vulcan synform (F1)
A
A′
A″
i i
10 km
Black Canyon succession
schist
massive quartzitic gneiss
migmatitic gneiss
amphibolite/greenstone
layered quartzitic gneiss
Symbols
pegmatite dikes
shear zone
average S2 foliation
magmatic foliation
foliation trajectory
Intrusive rocks
Curecanti monzogranite
Vernal Mesa monzogranite
post-tectonic plutons
Dubois/ Cochetopa plutons
mafic plutons
Pitts Meadow granodiorite
Dubois succession (1.77-1.75 Ga)
felsic volcanics
amphibolite
Present geometry:
Proterozoic rocks off-set by ~5.5 km left-lateral strike displacement on the Red Rocks fault
~5.5 km
Red Rocks fault
Restored geometry used above
i
UT
CO
0 50 km
40° 00′
38° 00′
107°00′
105°00′
Denver
Gunnison
Montrose
2.1
3.1
4

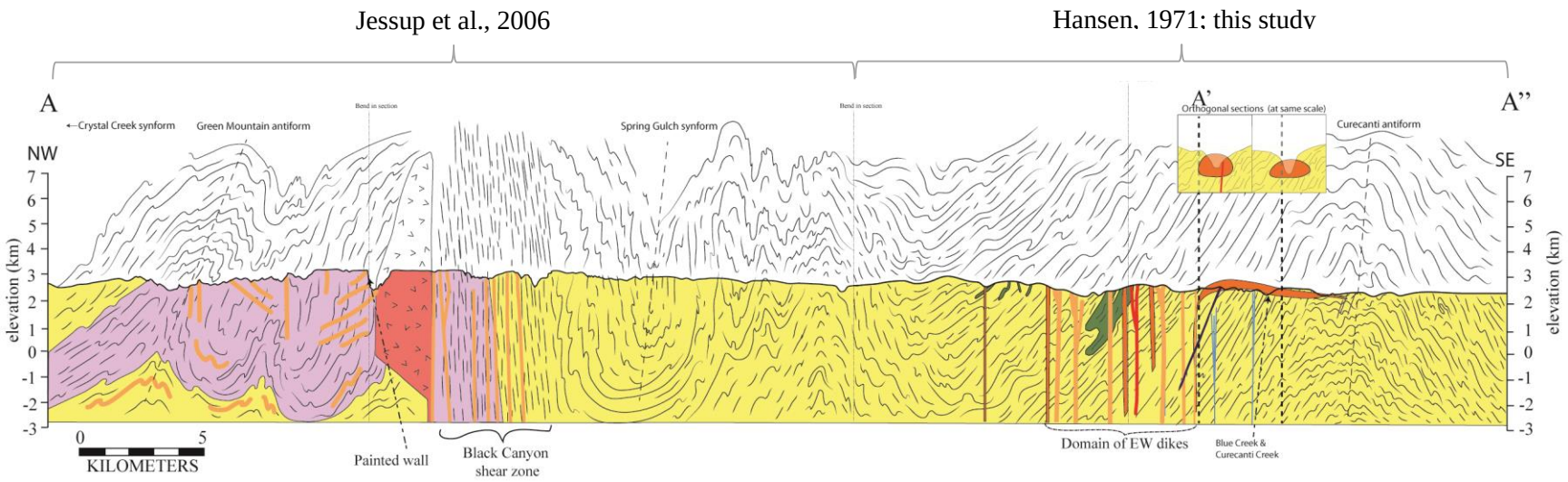

Figure 2-2. Simplified 60 km-long cross section A-A" of Proterozoic rocks exposed in the Black Canyon of the Gunnison, Colorado. Relatively minor Phanerozoic exposures omitted for clarity. Bends in section shown as faint dotted lines. See Figure 2-1 for cross section lines. No vertical exaggeration. Lamprophyre dikes (thin blue), present in the Curecanti Needle area, cross-cut the gneisses but are cross-cut by the Curecanti pluton. Two orthogonal sections show Curecanti pluton geometry. Color scheme consistent with Figure 2-1. Brackets above cross section delimit sources of data.

depositional, with the Black Canyon succession being deposited on top of the Dubois succession (Jessup et al., 2005). The Dubois and Cochetopa successions, representing two distinct age successions, contain metavolcanic rocks with preserved primary structures such as pyroclastic sheets, pillow lavas, and breccias (Bickford and Boardman, 1984; Bickford et al., 1989a). The Black Canyon succession is dominated by quartzofeldspathic metasediments, amphibolites, and schists (Hansen and Peterman, 1968; Hansen, 1971; Bickford and Boardman, 1984; Jessup et al., 2005). Primary sedimentary structures are preserved in some Black Canyon succession paragneisses, including ripple marks and cross-bedding (Jessup et al., 2006), helping to constrain the fold-sequence interpretation discussed in Section 2.3.2. Quartzofeldspathic paragneisses often grade into volumetrically subordinate bodies of pelitic schist. Intrusive rocks, including several generations of pegmatitic dikes and multiple plutons, are common throughout the canyon (Figs. 2-1 and 2-2; Hansen, 1971). The timing of igneous rock intrusion and deformation in the Black Canyon region is discussed in the next section.

2.2.2 Deformational history recorded in the Black Canyon of the Gunnison

Dubois, Cochetopa, and Black Canyon succession rocks record at least four distinct Precambrian ductile deformation events (Jessup et al., 2006). The age of these four deformation events is constrained by cross-cutting relationships and geochronology conducted by Hansen and Peterman (1968), Bickford et al. (1989b), Hill and Bickford (2001), Livaccari et al. (2001), and Jessup et al. (2005, 2006). Their data are summarized here.

(1) D_1 is characterized by isoclinal F_1 folds of sedimentary structures. An S_0-parallel S_1 fabric was developed during D_1, dipping steeply and striking north-south (Jessup et al., 2006). An amphibolite dike sampled from the northwest portion of the Black Canyon transect yielded a U/Pb age of 1741 Ma, and was interpreted by Jessup et al. (2006) to have formed during D_1. (2) S_1 foliation was folded during D_2 into shallowly plunging (1-25˚) northwest-trending upright F_2 folds common in the eastern part of the transect (Afifi, 1981). S_2 is the dominant foliation in much of the canyon, and the axial traces of kilometer-scale F_2 folds in the Black Canyon region are shown in Figure 2-1.

Also at this time, the Pitts Meadow granodiorite (1713 ± 2 Ma) was emplaced, along with many northwest-trending pegmatite dikes, and interpreted as synchronous with D_2 by Jessup et al. (2006). (3) The Black Canyon shear zone (BCSZ), developed during D_3, is a 4 km-wide domain of subvertical northeast-striking (average shear plane 246˚, 84˚ NW) S_3 fabric, subvertical L_3 stretching lineations, and highly transposed isoclinal folds (Tweto and Sims, 1963; Jessup et al., 2006). F_2 axial surfaces become parallel with L_3 as they approach the BCSZ and are interpreted to have been rotated in drag folds (e.g. the Green Mountain antiform and Spring Gulch synform; Fig. 2-1) during dextral shear on the BCSZ during D_3. In-situ monazite geochronology using grains from the matrix and inclusions in cordierite and staurolite in sample MJBC-43 (black star in Fig. 2-1) yield ages of 1403 ± 23 Ma (Jessup et al. 2005, 2006). The assemblage garnet + biotite + plagioclase + cordierite + anthophyllite ± staurolite, demonstrated that this sample reached 300 ± 100 MPa and 600˚± 50˚ C at 1403 ± 23 Ma (Jessup et al., 2006). Using a standard geobaric gradient of 30 MPa per kilometer (Winter, 2001), this assemblage constrains formation to a minimum depth of 6.6 km and a maximum depth of 13.3 km, Using a steeper geobaric gradient of 37 MPa per kilometer (e.g. Chambers et al., 2009), this assemblage formed between 5.4 km and 10.8 km at 1403 ± 23 Ma. Sample MJBC-43 was collected 3.5 km southeast of the Vernal Mesa monzogranite (Jessup et al., 2006), a pluton that was emplaced parallel to the S_3 foliation of the Black Canyon shear zone at 1434 ± 2 Ma (Fig. 2-2). The temporal and spatial proximity of the thermobarometric results for sample MJBC-43 and the geochronologic constraints on the Vernal Mesa pluton are interpreted to represent approximate emplacement pressure (Jessup et al., 2006). Also at this time, the Curecanti pluton (1420 ± 15 Ma; Hansen and Peterman, 1968) was emplaced 20 km southeast of the BCSZ and the Vernal Mesa pluton. (4) D_4 is recorded by northwest-striking moderately dipping pegmatite dikes (292˚, 51˚ NW) emplaced in tension gashes of the BCSZ, a stretching lineation in Black Canyon succession rocks (L_3-parallel; L_4 = 32˚→ 243˚), and reactivation of the BCSZ at 1413±2 Ma (Jessup et al., 2006).

Rocks of the Black Canyon succession reached amphibolite facies during D_1-D_2 (Hansen and Peterman, 1968; Hansen, 1972; Jessup et al., 2005), whereas the Dubois

succession only reached epidote-amphibolite to lowermost amphibolite facies, possibly during D_1 (Afifi, 1981). This variation in metamorphic grade over a 100 km-long transect is typical of Proterozoic rocks in the southwestern U.S., possibly as a result of polyphase metamorphism (Williams and Karlstrom, 1996). However, we don't believe the present exposure of the Black Canyon succession to represent drastically different crustal levels from north to south.

2.2.3 Correlating MJBC-43 to the Curecanti pluton

The Vernal Mesa pluton (1434 ± 2 Ma) was emplaced parallel to the subvertical, northeast-striking BCSZ; its margins are subparallel to S_3 in the BCSZ, and the pluton contains a magmatic foliation parallel to its margins (Fig. 2-1; Jessup et al., 2005). The Curecanti pluton, dated at 1420 ± 15 Ma by Hansen and Peterman (1968) using Rb-Sr, is exposed 20 km southeast. This age is obtained using a different geochronologic method, one that is less reliable and precise, but the age of the two plutons still overlaps with the given error range. The Curecanti pluton has a very different outcrop pattern than the Vernal Mesa pluton (see Section 3), which was emplaced into rocks that were at 600˚± 50˚ C and 300 ± 100 MPa (Section 2.2.2). However, these two plutons may have been emplaced at approximately the same crustal depth, within the error of the thermobarometric estimates provided by Jessup et al. (2006).

Unlike the large change in exposure level (one metamorphic grade) in Paleoproterozoic rocks over a map distance of ~70 km from the northern to southern ends of the Wet Mountains (Jones et al., 2010b), there is little evidence for the Black Canyon transect being a tilted section between the Vernal Mesa and Curecanti plutons (25 km). No major faults are documented that juxtapose drastically different crustal levels of Proterozoic rocks (Hansen and Peterman, 1968; Jessup et al., 2005). In addition, reconstructions of the Phanerozoic exhumation of Black Canyon transect rocks, first during the uplift of the Uncompahgre highland in the Paleozoic, then during the Laramide orogeny in the Tertiary, corroborate the suggestion of similar exposure levels between the Vernal Mesa and Curecanti plutons (Hansen, 1965).

Proterozoic rocks in the Black Canyon region were first uplifted during the early and middle Paleozoic in the ancestral Uncompahgre highland, which spanned from central Utah to New Mexico (Fig. 16 of Hansen, 1965). By the Cretaceous, the Uncompahgre highland was eroded, and was buried by marine sediments (e.g., Mancos Shale), which were subsequently uplifted during the Laramide orogeny (Hansen, 1965). During the Laramide orogeny in the early Tertiary, Black Canyon succession rocks were uplifted along the same faults responsible for Uncompahgre highland uplift (Hansen, 1987). One example of these recycled faults is the Red Rocks fault: a subvertical, northwest-striking, 32 km-long fault which had been active since Proterozoic time. The Vernal Mesa and Curecanti plutons are located on the same side (northeast) of the Red Rocks fault (Fig. 2-1), a section of rocks thought to have acted as a coherent block during Laramide uplift (Hansen, 1987). These reconstructions of uplift in the region, along with observations made between the area of the Vernal Mesa and the Curecanti plutons (Fig. 2-1) of similar patterns of coeval pegmatite dikes, suggests that there is little variation in the exposure level in these two areas, at least less than the 100 MPa margin-of-error for the geothermobarometric data discussed in Section 2.2.2.

CHAPTER 3
THE CURECANTI PLUTON

3.1 Introduction

The Curecanti pluton (1420 ± 15 Ma) is a sublenticular body of Precambrian monzogranite exposed in the Black Canyon of the Gunnison River and its tributaries between Colorado Highway 92, US Highway 50, Nelson Gulch, and Chipeta Falls (Fig. 3-1). Located 50 km west of Gunnison, CO, the pluton is roughly centered on Curecanti Needle, a 200-m-tall spire from which both the pluton and the Curecanti National Recreation Area aptly take their names (Hansen, 1964). Original reconnaissance geologic mapping by Hunter (1925) was augmented by the extraordinary maps of Hansen (1971), published just after the completion of the Blue Mesa and Morrow Point Dams. These dams create the Morrow Point and Blue Mesa Reservoirs and opened in 1966 and 1968, respectively. His published maps include the locations of the aforementioned dams, but their respective reservoirs were not filled when his mapping was completed, so geology now beneath the reservoir is inferred from Hansen's maps (Hansen, 1971). Because of fantastic exposure in both the subvertical walls of the Black Canyon and along the canyon rim, the geometry of the pluton is delimited very well by first-order observations (Fig. 3-1; Plate 1). Several transects through and across the pluton create a three-dimensional perspective of the pluton geometry and contact relationships (Fig. 3-2).

The main body of Curecanti monzogranite (CMG) crops out as a tongue-shaped dike approximately 5.5 km long, 3 km wide, and 0.4 km thick (Fig. 3-1). In addition to the main body, several dikes of CMG exposed in Blue Creek and Curecanti Creek are thought to be correlative because of similar composition and proximity to the main pluton (Hansen, 1964). These relatively small bodies of CMG are weakly foliated, and the two small bodies presently below the main pluton in Curecanti Creek (Fig. 3-1) may have, prior to uplift and erosion of the canyon, fed directly into the Curecanti pluton.

Figure 3-1. Detailed geologic map of Curecanti Needle area with inset explanation, Colorado reference map (inset), axial trace of Curecanti antiform, and cross section A'-A" from Fig. 2-1. Phanerozoic rocks in white. Geology modified from Hansen (1971).

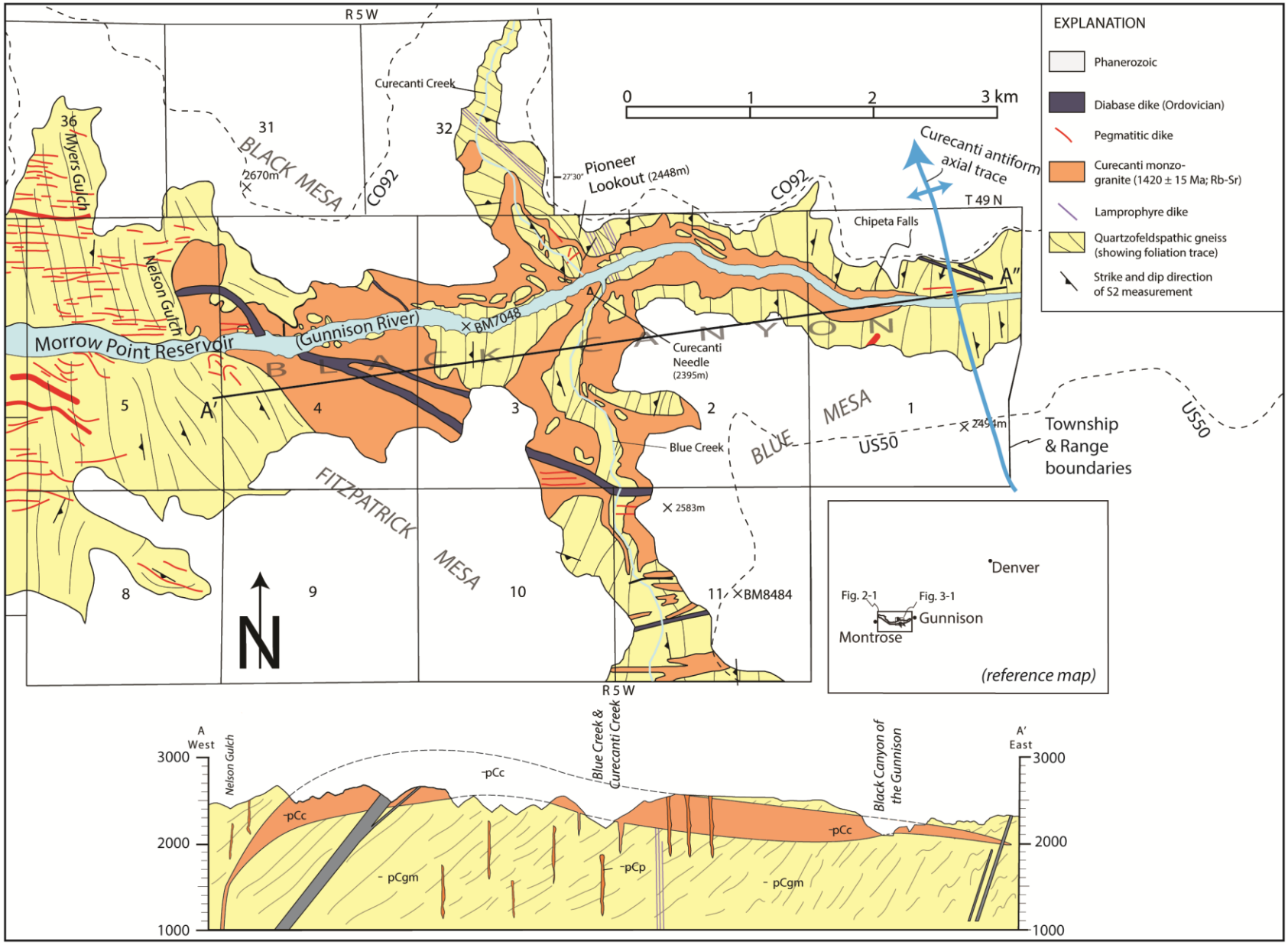
R 5 W
Curecanti Creek
0 1 2 3 km
EXPLANATION
Phanerozoic
Diabase dike (Ordovician)
Pegmatitic dike
Curecanti monzo-granite (1420 ± 15 Ma; Rb-Sr)
Lamprophyre dike
Quartzofeldspathic gneiss (showing foliation trace)
Strike and dip direction of S2 measurement
Curecanti antiform axial trace
T 49 N
Chipeta Falls
Pioneer Lookout (2448m)
27°30'
CO92
BLACK MESA
2670m
Myers Gulch
Nelson Gulch
Morrow Point Reservoir
(Gunnison River)
BM7048
BLACK CANYON
Curecanti Needle (2395m)
A
A'
A"
MESA
BLUE
US50
2494m
Township & Range boundaries
Blue Creek
FITZPATRICK MESA
2583m
BM8484
Denver
Fig. 2-1
Fig. 3-1
Gunnison
Montrose
(reference map)
R 5 W
A West
A' East
Nelson Gulch
Blue Creek & Curecanti Creek
Black Canyon of the Gunnison
3000
2000
1000
pCc
pCgm
pCp

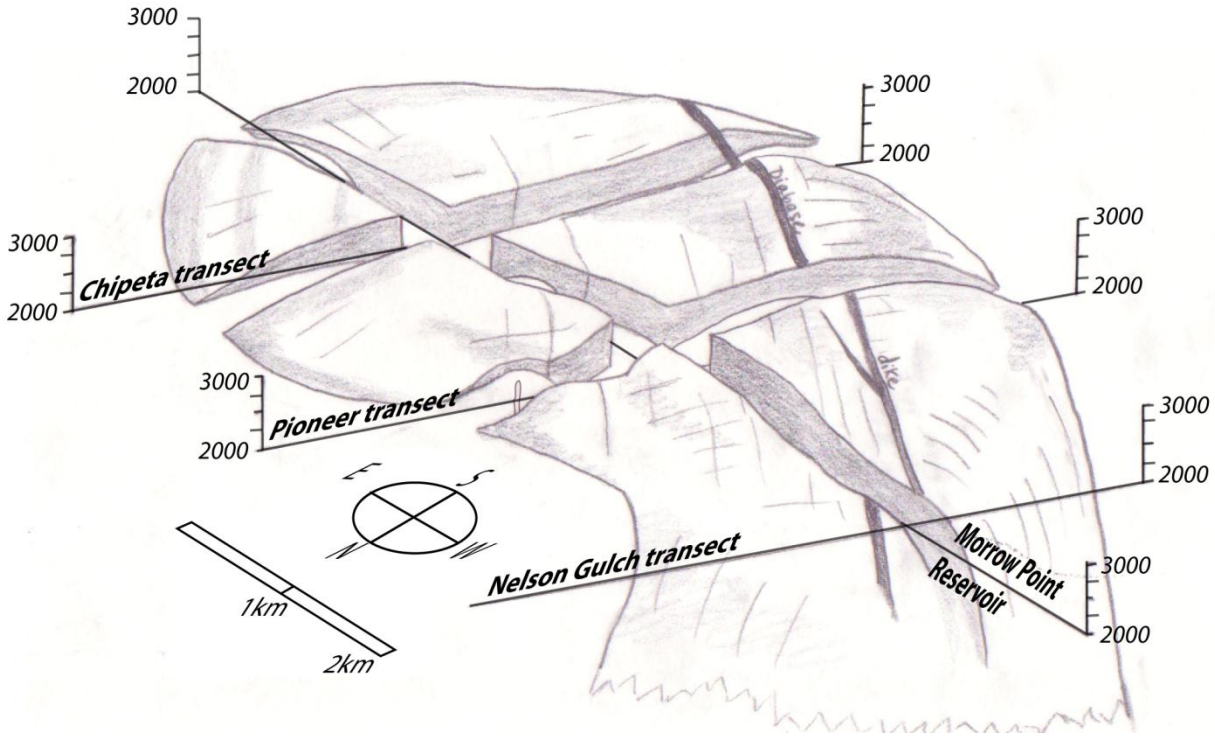

Figure 3-2. Semi-schematic Curecanti pluton stereogram showing location of the three transects described in Chapter 3.2 and approximate elevation above sea level (meters). Modified from Hansen (1964) using data from cross section A'-A" and field relationships described in text.

3.2 Three transects through a mid-crustal pluton

Studies of granitoid melt segregation, transport, ascent, and emplacement are often restricted to "remotely-sensed" geochemical or isotopic studies of correlative dikes and/or extrapolation of pluton geometry from limited surficial outcrop (Vigneresse et al., 1999; Petford et al., 2000). However, salient information regarding magmatic processes is preserved in the nearly complete three-dimensional shape of a crystallized pluton (Petford et al., 2000), something seldom available to observe or possible to accurately constrain. It is rare that pluton geometry is entirely exposed by topography (Vigneresse et al., 1999). On the edge of the Colorado Plateau, however, the Curecanti pluton is a Proterozoic monzogranite whose three-dimensional shape can be inferred from excellent exposures in the Black Canyon of the Gunnison, Blue Creek Canyon, and Curecanti Creek Canyon. Mapping by Hansen (1964, 1971), verified and updated by this study, provides the sublenticular map pattern and tongue-shaped geometry (Fig. 3-1) and the stereogram (Fig. 3-2) presented here.

The tall, steep walls of the Black Canyon of the Gunnison make interpreting a geologic map difficult, as most exposures are on near-vertical walls. In most locations, the orientation of Curecanti pluton floor and roof contacts are subhorizontal and shallowly dipping, and thus subparallel to the canyon topography. The geometry of the Curecanti pluton floor and roof contacts is highlighted by colors that distinguish between host rocks structurally above and below the pluton (Fig. 3-3). In several locations, where both the floor and roof contacts can be mapped in one cliff face (e.g. Pioneer Lookout wall), sample locations are projected across the canyon and onto photos where appropriate (Fig. 3-4). Characteristics of the pluton are presented in three transects representative of the pluton's roof zone, core, floor zone, correlative dikes, and its host rocks: The Nelson Gulch transect (Section 3.2.1) runs oblique to the pluton through its roof to its floor; the Pioneer transect (Section 3.2.2), running parallel to Curecanti and Blue Creeks, provides the most complete picture of the pluton; the Chipeta transect (Section 3.2.3) preserves the roof of

Figure 3-3. Sublenticular shape of Curecanti pluton, emphasizing its roof and floor contacts. Rocks structurally above and below the pluton are distinguished to assist in geologic map visualization. Locations of all samples indicated on map, and projected onto cross section pluton geometry from A'-A".

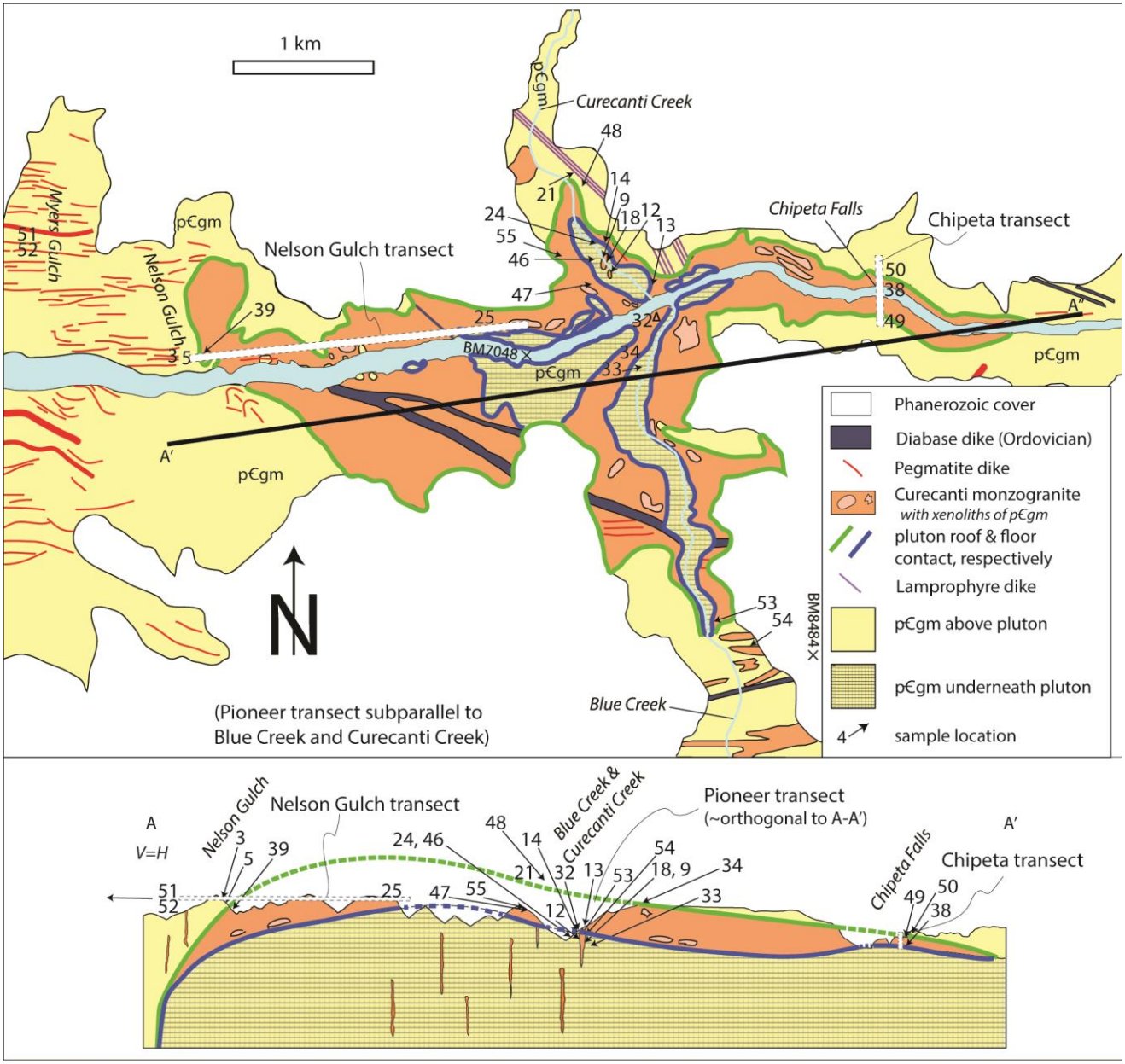
1 km
p€gm
Curecanti Creek
48
14
9
18
12
13
21
24
55
46
47
Chipeta Falls
Chipeta transect
50
38
49
A″
Myers Gulch
Nelson Gulch
Nelson Gulch transect
51
52
39
5
25
32
BM7048
34
33
p€gm
A′
BM8484
53
54
Blue Creek
(Pioneer transect subparallel to
Blue Creek and Curecanti Creek)
Phanerozoic cover
Diabase dike (Ordovician)
Pegmatite dike
Curecanti monzogranite
with xenoliths of p€gm
pluton roof & floor
contact, respectively
Lamprophyre dike
p€gm above pluton
p€gm underneath pluton
4
sample location
A
V=H
Nelson Gulch
Nelson Gulch transect
3
5
39
51
52
24, 46
25
47
55
48
14
21
32
12
Blue Creek &
Curecanti Creek
13
53
54
18, 9
34
33
Pioneer transect
(~orthogonal to A-A′)
A′
Chipeta Falls
Chipeta transect
49
50
38

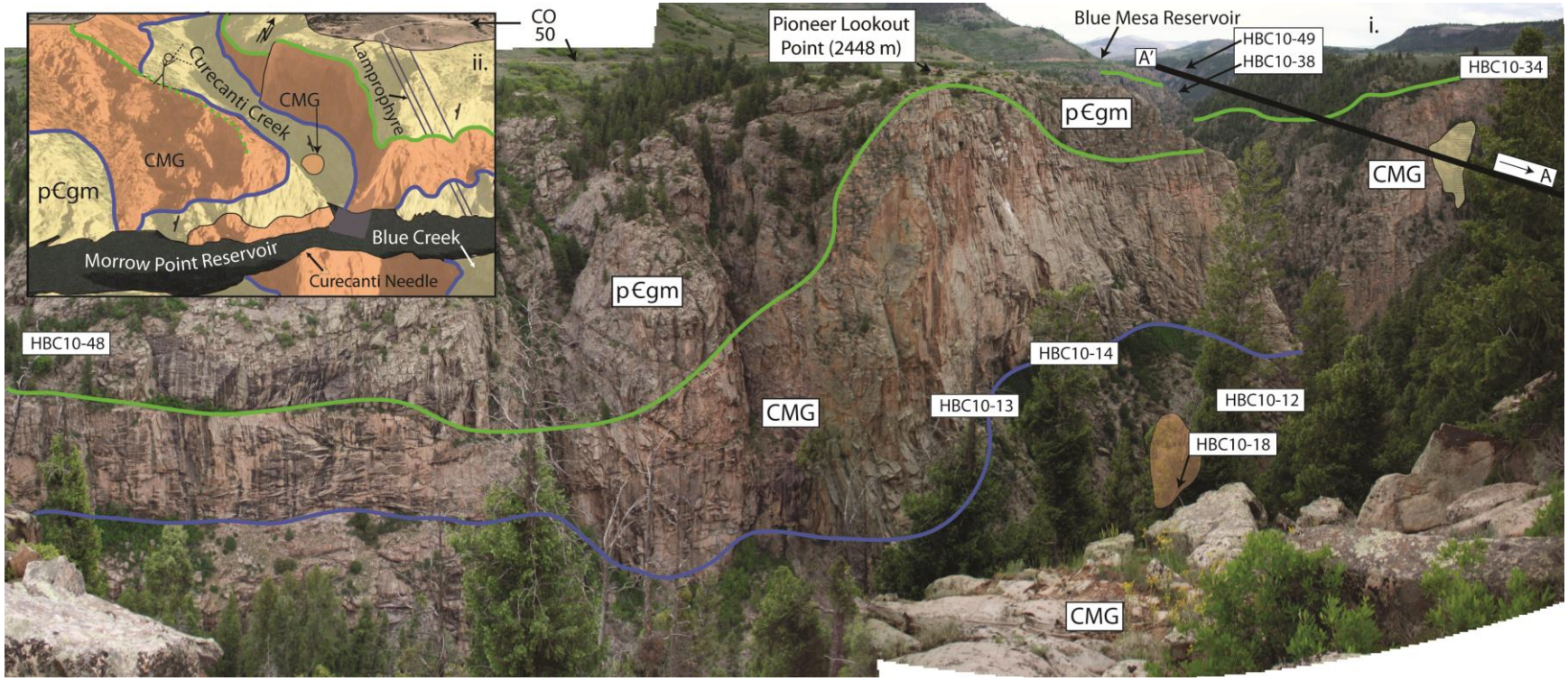

Figure 3-4. Panoramic photo (*i.* view to the east) from the west ridge of Curecanti Creek canyon showing the subhorizontal contacts of the Curecanti pluton, cross section line A'-A" from 3-1, and location of samples projected from the cross section line. Sub-lenticular body containing sample HBC10-18 (semi-transparent orange) may have been connected to the main body prior to erosion of Curecanti Creek canyon. A small building is located just right of the Pioneer Lookout Point label for scale. The Curecanti pluton is 213 m-thick below Pioneer Lookout. Irregularities in the floor and roof contacts are exaggerated by foreshortening of perspective. Inset *ii.* shows orthogonal view (Google Earth) to the north-northwest, strike and dip measurements from S_2 in host rocks, eroded roof (dashed line), and location of perspective for panoramic photo *i.*

the pluton just before it tapers out (Fig. 3-3). Meso- and microscale observations are reported along each transect and then combined to help elucidate the magmatic processes and emplacement mechanisms for this mid-crustal pluton. Fortunately, uncertainties regarding Curecanti pluton three dimensional geometry are chiefly limited to whether the small CMG dikes located in Curecanti Creek were originally feeder dikes to the Curecanti pluton, or whether or not they represent a different system of older dikes, as suggested by Hansen (1964). This distinction may have implications for the geometry of the pluton, i.e. whether it was emplaced as a horizontal sheet with one "root" near Nelson Gulch or was fed from several sources along its length (Section 9).

3.2.1 Nelson Gulch transect

The Nelson Gulch Transect (NGT) provides an oblique traverse through the Curecanti pluton from Nelson Gulch to BM 7048 (Fig. 3-3). It begins near the base of Nelson Gulch, 2182 meters above sea level, where CMG (e.g. HBC10-39) is in contact with garnet-bearing schist (e.g. HBC10-5) and quartzofeldspathic migmatites and gneisses (e.g. HBC10-3). This transect is subparallel to cross-section line A'-A", and sample locations are projected across the canyon onto the cross-section line in Figure 3-3. Line A'-A," a subsection of line A-A" in Figure 2-1, was chosen because it best represented the tongue-shaped geometry of the Curecanti pluton (Fig. 3-2), but the excellent exposure and resulting control over pluton geometry allows sample locations to be projected into the cross-section line A'-A".

At the base of Nelson Gulch quartzofeldspathic gneiss contains a well-developed foliation, equivalent to S_2 of Jessup et al. (2006), with a representative orientation of 330˚, 60˚ SW. Because exposures of the contact between CMG and gneiss are poor at this location, the orientation of the contact is estimated using three-point-problems. Assuming Nelson Gulch is approximately equal to the strike of the Curecanti pluton roof contact here, apparently true due to contrasting lithologies of p_gm and CMG on the west and east sides of the gully, respectively (Fig. 3-5), analysis indicates that the average orientation of the contact is 330˚, 60˚ SW. This contact is subparallel to the local

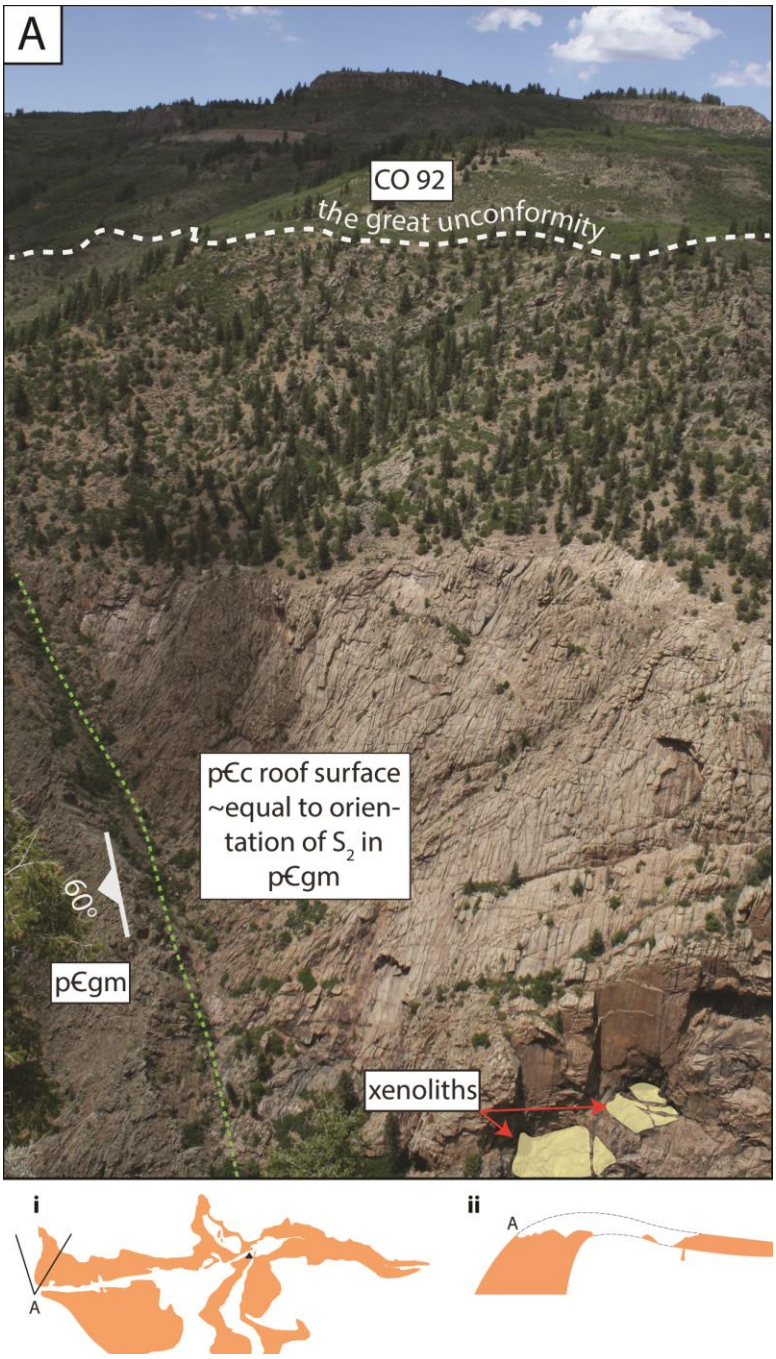

Figure 3-5. (A) View to the north-northeast of Nelson Gulch (left side of picture), Black Mesa (Tertiary volcanics exposed on ridge above CO 92 label), the Great Unconformity (subhorizontal dotted white line). There is 537 m of relief between the base of the photo and CO 92. Here, the Curecanti pluton roof contact (dotted green line) is oriented 330˚, 60˚ SW, subparallel to S_2 in its host rocks. Samples HBC10-5 and -39 were taken just below the field of view. Two angular xenoliths (semi-transparent yellow) of host gneiss can be seen (in the lower right of the photo) suspended by veins of CMG. Insets i. and ii. show locations for view of A (black line).

S_2 foliation. A broad orange surface is composed of CMG and creates a dip slope (Fig. 3-5) approximately equal to the pluton roof contact at this location.

Moving 1.5 km east of this location along the NGT line (Fig. 3-3), CMG extends from reservoir-level (2182 m) to the canyon rim (2496 m; e.g. HBC10-25), where it is unconformably overlain by the Jurassic Wanakah Formation (white on Fig. 3-3). Although the amount of pre-Jurassic erosion of the Curecanti pluton is uncertain, cross-section constructions based on the orientation of the roof contact in Curecanti Creek suggest that CMG located at the canyon rim here is ~70 m above the floor of the pluton (Fig. 3-3). 1.7-km-east of Nelson Gulch along the NGT, the contact between CMG and quartzofeldspathic gneisses changes from its orientation at Nelson Gulch (330˚, 60˚SW) to subhorizontal (Fig. 3-6). Here, the same quartzofeldspathic gneiss found at Nelson Gulch to be above CMG (Fig. 3-5) is found beneath CMG. Assuming that exhumation of this area did not overturn the entire section (Section 2.2.3), this 2.5-km-long transect provides a contact at Nelson Gulch of the pluton roof and a contact near BM 7048 of the pluton floor (Fig. 3-3). Macro- and microscopic observations are discussed in Sections 5.1 and 6.1, respectively.

3.2.2 Pioneer transect

East of BM 7048, contacts between the Curecanti pluton and its host rocks are mainly gently dipping, excluding minor undulations. Trending nearly orthogonal to the NGT, Curecanti and Blue Creek canyons provide transects through the Curecanti pluton roof zone, core, floor zone, and correlative CMG dikes. The Pioneer Transect (PT) traces from 1 km northwest of Pioneer Lookout Point, along Curecanti Creek, across the Morrow Point Reservoir, and south along Blue Creek as far as BM 8484 (Fig. 3-3). This traverse contains the most complete, intact, and accessible transect through pluton. Both the roof and floor contacts of the Curecanti pluton are exposed in the wall just below Pioneer Lookout Point, providing a cross section of the entire pluton (Fig. 3-4).

Various structural positions along the PT are used to characterize this portion of CMG. The structurally highest sample within the Curecanti pluton along this transect is located on a ridge 500-m-southwest of Curecanti Needle (sample HBC10-34 in Fig.

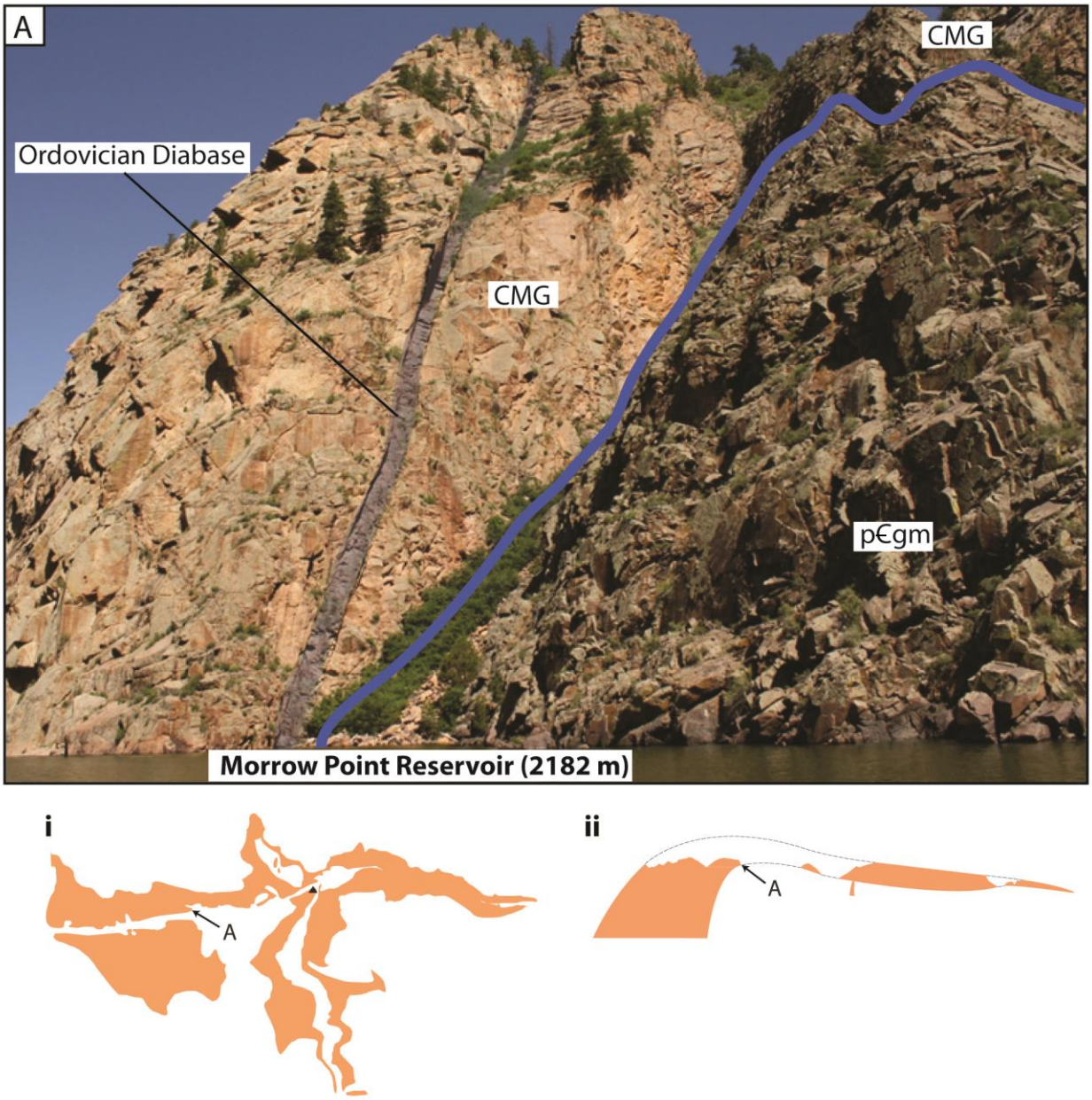

Figure 3-6. View to the north-northwest, 350 m-west of HBC10-25 (Fig. 8), from the Morrow Point Reservoir, of Curecanti pluton floor contact (blue line) as it changes from its orientation at Nelson Gulch of 330˚, 60˚ SW to subhorizontal and an Ordovician diabase dike (semi-transparent blue). There is ~300 m of relief between the Morrow Point Reservoir and the top of the CMG. Insets i. and ii. show location of A.

3-3). Because this is located just across the canyon from Pioneer Lookout wall (Fig. 3-4), the elevation of the pluton roof is known and the location of the sample is projected across the canyon in Fig. 3-5. In addition, the structural style of this location supports the interpretation of being in a pluton roof zone (discussed in Section 5.2.1). Moving down through the pluton, the locations of samples are most easily constrained in Curecanti Creek, where the entire thickness of the pluton is preserved (Fig. 3-4). Two dikes of CMG are exposed <30 meters below the pluton (Fig. 3-3).

3.2.3 Chipeta transect

1.6-km-east of Pioneer Lookout Point, Corral Creek drops 210 m from CO 92 at the Black Canyon rim to the Morrow Point Reservoir in a feature called Chipeta Falls. The canyon through which the waterfall runs, Corral Creek Canyon, provides another transect through the Curecanti pluton and a view back into the Black Canyon of the Gunnison where the Curecanti pluton geometry can again be verified from a distance (Fig. 3-7). Because Morrow Point Reservoir opened in 1968 as the Black Canyon was intentionally flooded by the Morrow Point Dam as part of the Colorado River Storage Project, the floor of the pluton is currently 20 m below the reservoir (Hansen, 1971). Mapping from before the flooding shows the floor contact in this location as subparallel to and 70 m below the roof contact (Hansen, 1971). Thus, the true thickness of the Curecanti pluton is known at this location to be 90 m, and the structural position of samples within the Curecanti pluton that are collected at the level of the Morrow Point Reservoir (e.g. HBC10-38 on Fig. 3-3) are accurately delimited.

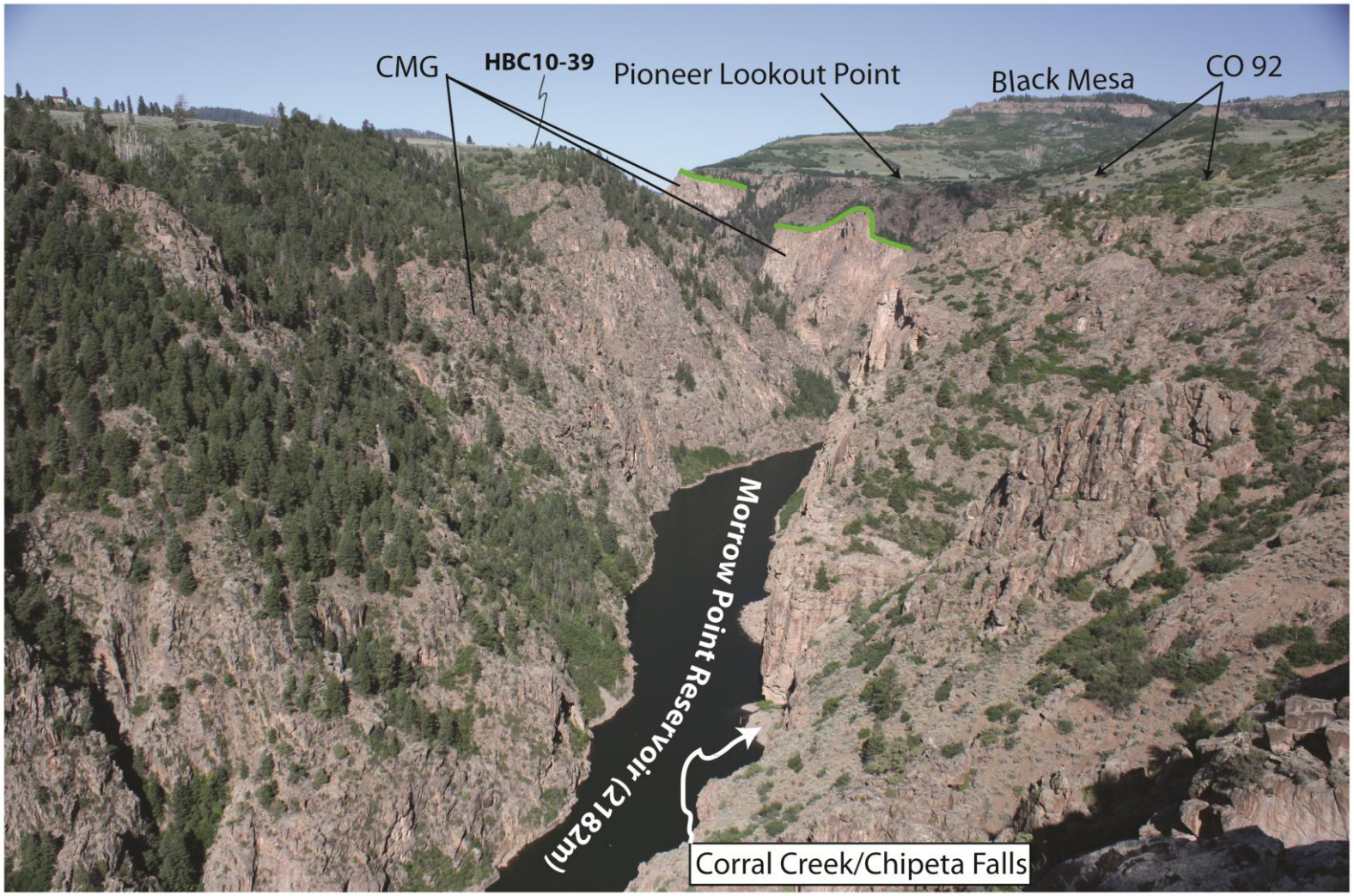

Figure 3-7. View to the west from Black Canyon rim, 300 m-east of Corral Creek (base of Chipeta Falls indicated by white arrow), showing the Morrow Point Reservoir, the ridge from which sample HBC10-39 was sampled (Curecanti pluton's roof zone), and the Curecanti pluton's subhorizontal roof (green lines). South (left) side of canyon consists of CMG in this field of view.

CHAPTER 4
METHODS

4.1 Field work – mesoscale observations

Since the mapping of the Black Canyon of the Gunnison (Hansen, 1971), description of the Curecanti pluton (Hansen, 1964), and geochronology of the igneous rocks (Hansen and Peterman, 1968), there have been major advances in geochemical and isotopic studies, reassessments of physical processes regarding magmatic systems (Petford et al., 2000), a reevaluation of how structural geologists map kinematics in the field (Passchier and Trouw, 2005), and a series of reviews discussing how to distinguish between magmatic and solid-state fabrics in granitoids (Paterson et al., 1989; Bouchez et al., 1992; Miller and Paterson, 1994; Paterson et al., 1998; Vernon, 2000). As such, contacts in the area were confirmed, remapped where necessary, and fabrics were reevaluated using a modern frame of reference regarding structural geology. These are presented on a detailed geologic map of the Curecanti Needle area, which serves to compliment the mapping of Hansen (1971) and provide new observations which elucidate the emplacement mechanisms of the Curecanti pluton (Fig. 3-1).

4.2 Petrography – microscale observations

There has been a longstanding controversy over which structures best distinguish between foliations formed in granitoids due to magmatic flow from those formed by tectonic stresses (Paterson et al., 1998). Magmatic flow is hereby and elsewhere defined as displacement of melt and crystals without sufficient interaction between suspended crystals to cause plastic deformation (Paterson et al., 1989). Contrary to doubts cast by Berger and Pitcher (1970), Paterson et al. (1989) argued that it is possible and important to distinguish between fabrics that form during flow of magma, as the magma reaches some critical level of crystallization that permits solid-state flow, as a result of ballooning, during syntectonic emplacement, as a result of regional tectonic stresses, or by some combination of the above processes. Reviews by Paterson et al. (1989) and Vernon (2000) were used as the basis for studying the petrography of CMG. A summary

of the criteria to distinguish between magmatic (suspension-like behavior), submagmatic (flow with less than enough melt to support suspension-like behavior; i.e. "crystal mush" behavior), and high-temperature (subsolidus plastic deformation) or moderate- to low-temperature solid state flow (Paterson et al., 1989) can be found in Table 4-1. Because pluton emplacement may involve flow of magma oblique to conduit margins (Courrioux, 1987), multiple pulses of melt (Vernon et al., 1989), and a dynamic stress field within and around a pluton (Vigneresse et al., 1999), distinguishing between a magmatic and tectonic foliation is not as simple as determining whether the pluton and host rock foliation are parallel or distinguishing between homogeneous and heterogeneous strain accumulation (Gapais and Barbarin, 1989).

The best evidence for a magmatic flow foliation is the alignment or imbrication of euhedral crystals, usually plagioclase in granitoid rocks, or microgranitoid enclaves without internal deformation (Fig. 4-1A and 4-2B). This implies enough melt is present to prevent crystals from plastically interacting with one another (Vernon, 2000). Another reasonable criterion for distinguishing magmatic flow includes schlieren layering or elongate microgranitoid enclaves, where they record magmatic flow around previously quenched relicts of host magma (Paterson et al., 2004). An argument for magmatic flow is strengthened if any of the aforementioned fabrics are deflected around, rather than pass through, resistant xenoliths. If using these criteria, it is important to distinguish host rock xenoliths derived locally due to magmatic wedging (Hutton, 1996) from microgranitoid enclaves which may be from the pluton's source region and be transported great distances along with the melt (Chappell et al., 1987; Paterson et al., 2004).

Clear evidence for solid-state flow in a granitoid includes internal deformation and recrystallization of primary crystals (Fig. 4-1C-D). In addition, the presence of microcline twinning is typical of potassium feldspar in solid-state-deformed rocks (Bell and Johnson, 1989). While myrmekite was classically thought to form due to solid-state replacement of potassium feldspar (Phillips, 1974), Hibbard (1979) suggested that its presence indicates pressure-quenched crystallization of a water-saturated melt, thus implying a magmatic origin for myrmekite. However, more recent experimental data

Table 4-1. Criteria available to distinguish magmatic vs. solid-state fabrics in granitoids. Adapted and compiled from Paterson et al. (1989) and Vernon (2000).

Magmatic flow	Solid-state flow	Submagmatic flow
1. Alignment of elongate euhedral crystals which are not internally deformed	**1. Internal deformation and recrystallization**	1. Recrystallized feldspar
2. Imbrication of elongate euhedral crystals which are not internally deformed	2. Recrystallized tails on deformed grains	2. Calcic plagioclase in myrmekite
3. Minor solid-state strain in the interstices between euhedral crystals	**3. Elongation of recrystallized aggregates**	3. Evidence for c-slip in quartz or a quartz c-axis point maximum orientation
4. Elongation of microgranitoid enclaves without plastic deformation	**4. Grain size reduction**	4. Recrystallization of hornblende
5. Flow foliation deflected around more resistant xenoliths	5. Fine grained folia deflected around less deformed relicts	**5. Magmatic minerals in pressure shadows or between fragmented grains**
6. Schlieren layering due to velocity gradient flow sorting without plastic deformation	**6. Microcline twinning**	
	7. Myrmekite	
	8. Flame perthite	
	9. Boudinage of strong minerals	
	10. Foliation passes through enclaves	
	11. Highly heterogeneous strain	
	12. Brittle and ductile deformation	
	13. Recrystallized biotite with a younger geochronology age than intrusion age	*nota bena: Criteria used in this document in bold*

Figure 4-1. Representative examples of magmatic and solid-state flow foliations in igneous material. **(A)** Magmatic flow foliation defined by alignment of microgranitoid enclaves without plastic deformation, from (Paterson et al., 1989). **(B)** Thin section from similar microgranitoid enclave as in *(A)* where alignment of plagioclase and hornblende has occurred without plastic deformation of interstitial quartz, again suggesting a magmatic origin for the foliation. From Vernon (2000). **(C)** Evidence of solid-state deformation (i.e. recrystallized quartz; black arrows) without much strain accumulation (e.g. elongation of grains and recrystallized aggregates) in granodiorite. From Vernon (2000). **(D)** Euhedral plagioclase laths (black arrows) showing igneous structure, but kinked biotite and recrystallized quartz (red arrows) suggests solid-state flow. From Vernon (2000). **(E)** Long axis of euhedral plagioclase in lower right of photomicrograph is parallel to the foliation, and an incipient C-surface defined by another tabular plagioclase may be evidence for submagmatic flow in this tonalite. From Miller and Paterson (1994). **(F)** Fractured plagioclase (plag) filled by feldspar (fld) or quartz (qtz) in a granodiorite. Note that host twins extend into feldspar that fills fracture, suggesting submagmatic flow. From Bouchez et al. (1992).

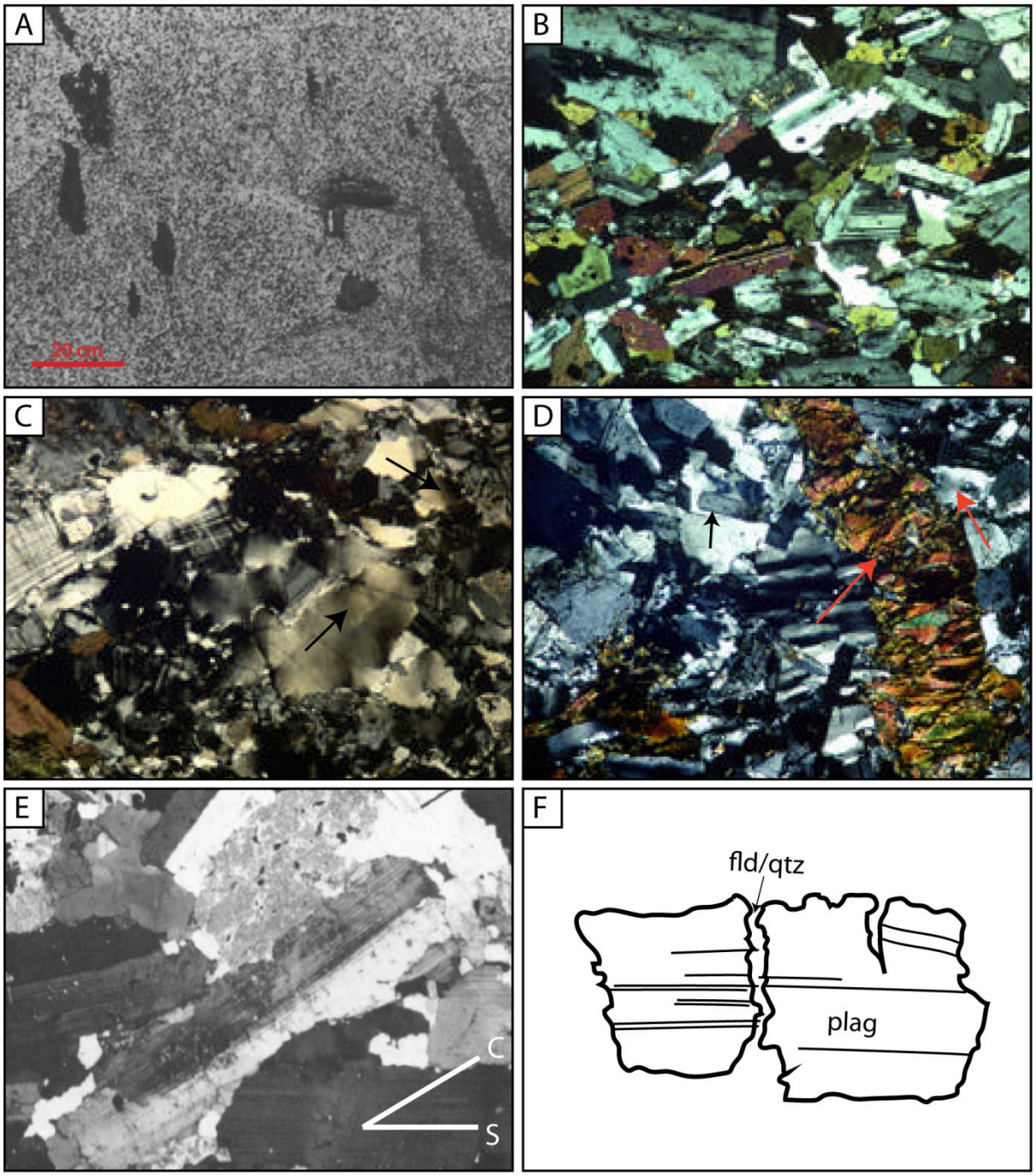
A
20 cm
B
C
D
E
C
S
F
fld/qtz
plag

(Burnham and Nekvasil, 1986) suggests that a solid-state replacement, rather than magmatic, origin for myrmekite is preferable (Vernon, 1991). As such, the presence of myrmekite in granitoids may be an indicator for solid-state flow. Flame perthite is a normal form of alkali feldspar which has undergone solid-state deformation, which may make its presence indicative of solid-state flow. However, flame perthite is considered to be a more ambiguous indicator of solid-state flow in a granitoid (Pryer and Robin, 1996; Vernon, 2000).

Although these end-member deformation conditions (magmatic and solid-state) are relatively easy to distinguish between, there theoretically exists a continuum between the two. This continuum may be a result of either tectonic shortening (Castro, 1987) or ballooning of a pluton as its interior is still magmatic (Paterson et al., 1989). While criteria that unambiguously indicate this so-called submagmatic flow are difficult to observe, the best criteria for submagmatic flow are likely recrystallized feldspar with exsolution lamellae, calcic plagioclase in myrmekite, c-slip in quartz or a point maximum of quartz c-axis orientations, S-C foliation arrangements (Fig 4-1E), and late magmatic minerals (i.e. quartz and/or feldspars) in areas between fragmented primary grains (Fig 4-1F; Paterson et al., 1989; Bouchez et al., 1992; Vernon, 2000). The criteria to distinguish these transitional fabrics (i.e. submagmatic foliation) are more tentative than criteria to distinguish the end-members processes, but are beginning to gain acceptance in the geologic community (Vernon, 2000).

Relative deformation temperatures within the Curecanti pluton were assessed using quartz deformation textures. The three phases of grain-boundary mobility are bulging (BLG, 280-400 °C), subgrain rotation (SGR, 400-500 °C), and grain-boundary migration (GBM, >500 °C; Hirth and Tullis, 1992; Stipp et al., 2002). These microstructures reflect quartz recrystallizing by dislocation glide and creep (BLG), climb-accommodated dislocation creep (SGR), and high-temperature grain-boundary migration (GBM; Stipp et al., 2002). While these three temperature-dependent quartz recrystallization mechanisms were observed and described for quartz veins in pelitic rocks (Stipp et al., 2002), they have also been used for granitoid rocks with similar results

(Inglis et al., 2005; Passchier et al., 2005; Saha and Chakraborti, 2007; Kilian et al., 2011; Zibra, 2012).

4.3 Magma driving pressure

Gravity is a well-accepted mechanism for vertical transport of melt though the crust (Petford et al., 2000). However, the traditional idea of buoyant granitoid melts ascending through a cold crust as diapirs has shifted towards models invoking narrow conduits that feed into plutons as their ascent is arrested (Petford et al., 1993; Clemens and Petford, 1999). Weertman (1971) used dislocation theory to derive a series of equations that show a liquid-filled crack within an elastic plate has a hydrostatic pressure at its tip (P), causing the liquid to rise within the plate if P > the lithostatic pressure at the base of the crack (P') in the elastic plate. These ideas were extended to model vertical transport of magma beneath oceanic spreading centers (Weertman, 1971). Two types of liquid-filled cracks exist: fractures that become isolated from their source region and fractures that maintain connectivity with their source reservoir. Isolated cracks may transport buoyant liquid and/or be arrested by a subhorizontal anisotropy (Weertman (1971). In contrast, fractures which maintain connectivity with their source chamber ascend in part due to their "magma driving pressure" (Baer and Reches, 1991). Magma driving pressure (P_d) is hereby and elsewhere defined as the difference between the sum of forces supporting dike propagation and the stresses perpendicular to the dike wall. P_d is represented by

$$P_d = P_h + P_o - P_{vis} - S_h \quad \textbf{(1)}$$

where P_h is the hydrostatic pressure, P_o is the magma chamber overpressure, P_{vis} is the viscous resistance to flow in the dike, and S_h is the tectonic stress perpendicular to the dike wall (Weertman, 1971; Weertman and Chang, 1977; Hogan and Gilbert, 1995). Exponential increase of magma viscosity as temperature falls within a melt is the chief problem for modelling magma ascent using P_d. Clemens and Mawer (1992), however, demonstrated that a rising viscosity due to falling temperature may be offset by the rise in melt H_2O that accompanies crystallization. Others have verified that narrow conduits can indeed transport enough granitoid material to fill large plutons relatively rapidly without freezing (Petford et al., 1993; Petford et al., 1994; Petford et al., 2000).

4.3.1 Hydrostatic pressure (Ph)

For dikes that maintain connectivity with their source magma chamber, P_h is the difference between the lithostatic pressure on the top of the source region at depth D and the pressure at the dike's tip at some depth Z. The differential hydrostatic pressure at depth Z is written as

$$[P_h]_Z = (p_c - p_m)g(D - Z) \quad \textbf{(2)}$$

where p_c and p_m are the density of the crustal and magma columns, respectively. $[P_h]z$ should be zero at the depth of the source (D), because the difference between D and Z here is zero, and $[P_h]z$ will increase as the dike ascends from the source magma chamber.

4.3.2 Magma chamber overpressure (Po)

Pressure may be generated in a magma chamber when vapor saturation is reached in the melt, causing bubble nucleation (Burnham, 1979). If bulk H_2O-content in a magma is higher than that which can be accommodated by hydrous minerals crystallizing from the melt, a volume increase of up to 60% at 0.5 kbar, or 20% at 2 kbar, may result (Burnham, 1979). This process, also called resurgent or second boiling, is recognized as important for the generation of pegmatites and pegmatite swarms (Jahns and Burnham, 1969) and explosive volcanism (Burnham, 1979). Resurgent boiling causes a pressure increase which is quantifiable and represented by P_o.

4.3.3 Viscous pressure drop (P_{vis})

The parameter that quantifies the resistance to flow of magma within a dike as it moves away from its source region is the viscous pressure drop (P_{vis}). At a distance, l, from the chamber at depth, Z, P_{vis} is

$$P_{vis} = \Delta P_{vis}\left([l^2 + (D - Z)^2]^{\frac{1}{2}}\right) \quad \textbf{(3)}$$

where ΔP_{vis} is the viscous pressure drop per unit distance (Baer and Reches, 1991). This value can be quantified when the dike thickness, magma viscosity, and flow rate are all known; it is also likely that all three of these variables change along the length of a dike. Geologically reasonable values for P_{vis} are on the order of 1.0 MPa km^{-1} (Reches and Fink, 1988; Baer and Reches, 1991).

4.3.4 Horizontal stress (S_h)

The horizontal normal stress acting on a plane (e.g. a liquid-filled fracture) in the crust is the sum of the tectonic stress and lithostatic overburden (S_v) acting on that plane. The value of P_d for a magma emplaced during a purely lithostatic state of stress in the crust when

$$\sigma_1 = \sigma_2 = \sigma_3 = \rho_c g Z \qquad \textbf{(4)}$$

can be calculated by substituting **(4)** for S_h in **(1)**. Disregarding the relatively minor components of P_o and P_{vis}, this modified equation represents a stress-regime where the level of neutral buoyancy (i.e. when $\rho_m = \rho_c$) determines the level to which a magma may ascend. In order for the liquid to rise at all, however, an assumption must be made that the crack will remain open and that no additional horizontal normal stress acts on the crack walls. The driving pressure of this magma is represented by P_m and is used as a reference (Hogan et al., 1998). However, when the state of crustal stress is known, the issue of calculating P_d becomes a structural geology problem; the most interesting case is perhaps when the crust is extending and is thought to be at its tensile yield strength, quantifiable by a crustal strength curve (e.g. Maggi et al., 2000). In this case, disregarding the relatively minor effects of P_{vis} and P_o, the value of P_d can be estimated by adding the strength curve (which is equal to S_h in this case) to the differential hydrostatic pressure curve $[P_h]z$ (Fig. 4-2).

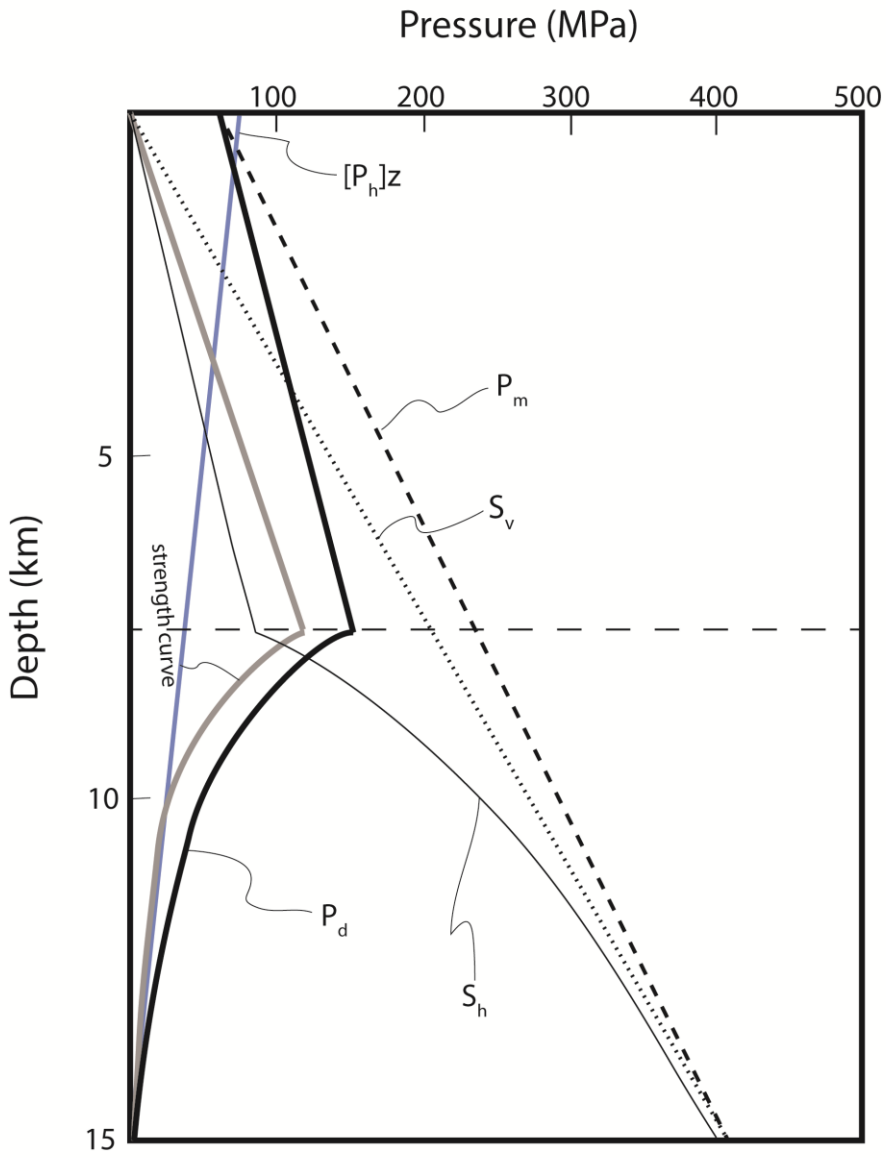

Figure 4-2. Compilation of data from (Hogan and Gilbert, 1995) and (Hogan et al., 1998) showing lithostatic overburden (S_v, dotted line), differential hydrostatic pressure ($[P_h]_z$, dashed line), crustal strength curve (gray line), horizontal normal stress (thin black line; $S_h = S_v$ + strength curve), differential hydrostatic pressure ($[P_h]z$; blue line), and magma driving pressure (thick black line; $P_d=[P_h]_z + S_h$,). Magma was sourced from 15 km depth, hence $[P_h]_z$ is zero here. Note that magma driving pressure (P_d) exceeds lithostatic overburden (S_v) at a depth of about 4 km and maintains a positive value at the Earth's surface, indicating the potential for this magma to erupt as a volcano if it is not arrested by an anisotropy between 4 and 0 km depth (Hogan and Gilbert, 1995; Hogan et al., 1998)

4.3.5 Example of a calculated magma driving pressure

Hogan and Gilbert (1995) calculated P_d for two magmas located on the southern Oklahoma aulocogen (SOA). These authors had quantitative constraints regarding depth to the magma source region, final emplacement depths, and the state of stress in the crust at the time of emplacement. After using geologic models of the crust beneath the SOA (Coffman et al., 1986) to model crustal density at various depths, they used geochemical data to calculate the density of their magma (Hogan and Gilbert, 1995). They determined there to be a zero-value for P_o due to intrinsically low H_2O content of the magma (Section 4.3.2 discusses the relationship between water content and P_o) and used a maximum value of 0.75 MPa km^{-1} for ΔP_{vis}. Because they were able to determine that the crust was at its tensile strength during emplacement of the magma in question, they simply used pressures (in MPa) from differential strength at failure (a yield strength profile) of for a crust in tension from (Lynch and Morgan, 1987) to approximate the horizontal normal stress on the dike walls during ascent. Because $S_h = S_v$ + tectonic stresses (Section 4.3.4), S_h was quantified by the addition of the yield strength profile curve to the lithostatic overburden curve (S_v). P_d was calculated at a number of depths, and these data are reproduced (Fig. 4-2). P_d reaches a maximum value at the brittle-ductile transition, which was about 8 kilometers deep in this region at this time. The subsequent magma driving pressure exceeded the lithostatic overburden pressure at a depth of about 4 kilometers, indicating the potential for the magma to reach the Earth's surface unless a horizontal anisotropy, or "crack-stopper" (Weertman, 1971), is reached (Fig. 4-2). P_d for four end-member magmas were proposed by Hogan et al. (1998): (1) P_d might become negligible at some depth, resulting in a magma freezing as a vertical dike; (2) magma might reach a horizontal anisotropy while it still has a positive value for P_d, but its P_d is insufficient to make space by vertical displacement of roof rocks; (3) magma might maintain a positive P_d to the Earth's surface without encountering anisotropies sufficient to stop dike propagation, and may erupt as a volcano; (4) magma might encounter a horizontal anisotropy while it is ascending, and its P_d may be high enough at this depth to lift its roof rocks (Fig. 4-3).

Note that assumptions must be made that the magma remains entirely liquid and that the crack is able to remain open and propagate upward, though the hydrostatic pressure (and thus the driving pressure) is far lower than the lithostatic overburden. Weertman (1971) considered this to be a non-issue, as glacier crevasses partly filled by water remain open and water is permitted to propagate up from the bottom of these cracks even when the lithostatic stress is higher than the differential stress at this point. In extension, the value of S_h can be far lower than S_v due to the subtractive effect of tensile stresses when calculating S_h (Section 4.3.4). Also of consideration is the "tectonic squeezing" effect of stress on fluids moving through fractures.

The tectonic squeezing effect was first discussed at length by Pitcher (1975). Areas of local dilatancy can also focus melt in the crust (Hutton, 1996) and faults can rapidly redistribute fluids (Sibson et al., 1975), providing potential solutions to the age-

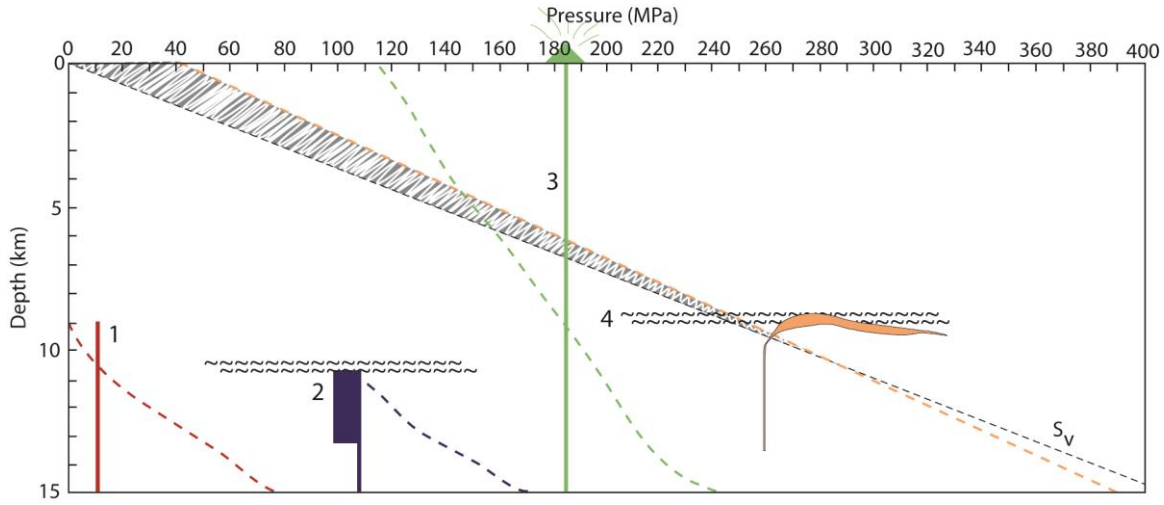

Figure 4-3. Four end-member results of magma driving pressures (dotted lines) and their associated magma/pluton shapes (solid polygons), adapted from Hogan et al. (1998). **(1)** P_d might become negligible at some depth (dotted red line), resulting in a magma freezing as a vertical dike (red line). **(2)** Magma (blue polygon) might reach a horizontal anisotropy (~~~ symbols) while its P_d (blue dotted line) is still positive, but insufficient to make space by vertical displacement of roof rocks. **(3)** Magma (green line) might maintain a positive P_d (dotted green line) to the Earth's surface without encountering anisotropies sufficient to stop dike propogation, and may erupt as a volcano. **(4)** Magma (orange polygon) might encounter a horizontal anisotropy (~~~ symbols) while it is ascending, and its P_d (dotted orange line) may be larger than S_v and the magma may lift its roof rocks.

old “space problem” of granite emplacement and offering a solution to how fluids might travel along fractures when their hydrostatic or buoyant forces are far less than the lithostatic overburden. This phenomenon includes emplacement in transtensional stepovers in strike-slip faults (Schmidt et al., 1990), emplacement in Mohr-Coulomb fractures within shear zones (Castro, 1987; Jessup et al., 2006), and emplacement in dilatational areas associated with shear-zone folds (McCaffrey, 1992). However, the magma driving pressure model, based on derivations by Weertman (1971), only considers the normal stress perpendicular to a dike wall to either be prohibitive to dike-propagation (for a compressive stress) or to assist its ascent (for tensile normal stresses; Reches and Fink, 1988; Baer and Reches, 1991; Hogan and Gilbert, 1995; Hogan et al., 1998).

4.4 Stress field during emplacement

Once calculated, magma driving pressure indicates a pressure exerted on the walls of the dike through which it is being transported. This force acts on the local principal stresses in the crust around the dike, and thus can be used during the construction of Mohr circle diagrams while evaluating the instantaneous stress field around an ascending magma (Vigneresse et al., 1999). Mohr circle diagrams are a common tool that can be used to represent a state of stress in the crust by plotting shear stress against normal stress (Fig. 4-4A).

4.4.1 Mohr circle construction

The usual notation for the three principal stress components (the planes in a body which only experience a normal stress and no shear stress; Means, 1976) – are $\sigma_1 > \sigma_2 > \sigma_3$, with the differential stress ($\sigma_1 - \sigma_3$) defining the diameter of the Mohr circle (Jaeger and Cook, 1979). Failure occurs in Mohr space when the Mohr circle intersects the failure envelope, a line that plots the equivalent normal and shear stresses on a failure plane over a range of differential stresses (Fig. 4-4A.). Fracture plane orientations are predicted in real space (Fig. 4-4B) by the angle 2Θ (angles are doubled in Mohr space) between a line perpendicular to the tangent line where the Mohr circle intersects the failure envelope and the x-axis (Fig. 4-4C). Θ represents the angle between σ_1 and the failure plane in brittle

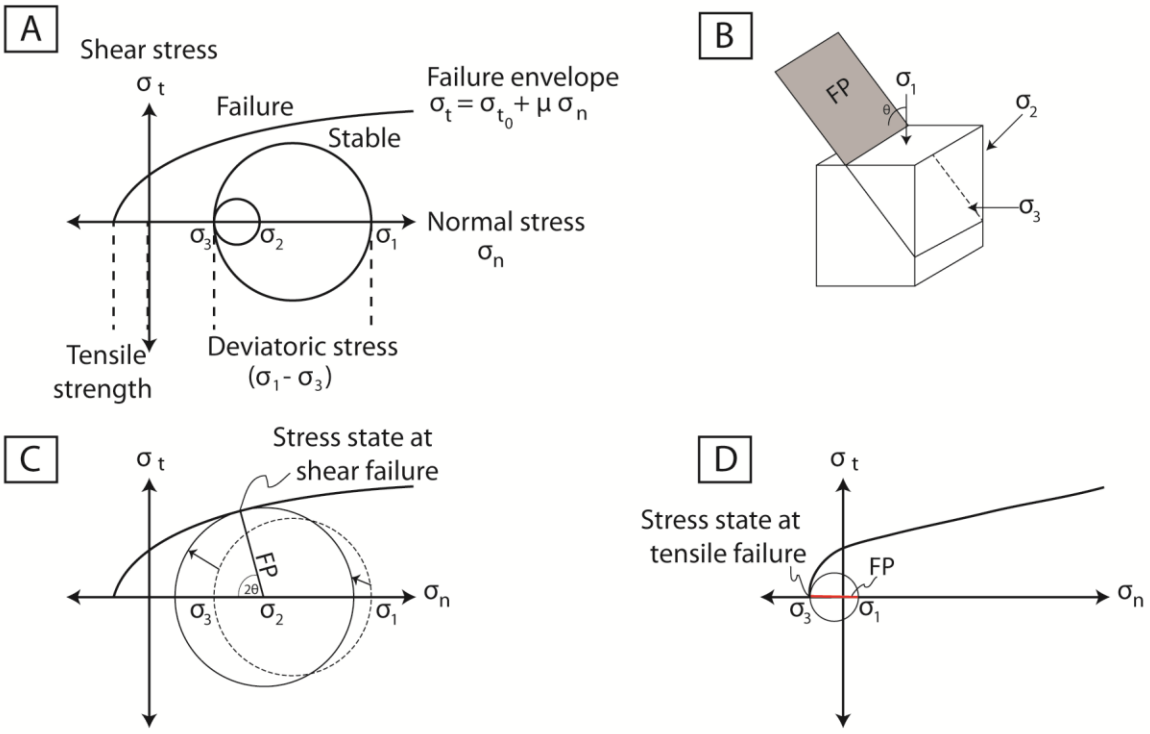

Figure 4-4. Explanation of Mohr space, a plot of shear stress (σ_t) and normal stress (σ_n). (A) Deviatoric stress is the difference between the greatest (σ_1) and least (σ_3) compressive stresses, which plot along the x-axis (σ_n) of Mohr space. The failure envelope for any rock is the line that divides Mohr space between stable and failure, and if the failure envelope plots in the negative normal stress side, that particular rock has tensile strength. (B) The failure plane (perpendicular to the tangent line where a Mohr circle intersects the failure envelope) orientation (Θ° from σ_1) plots as 2Θ in Mohr space. (C) A decrease in both principal stresses results in a translation and change of deviatoric stress that may be sufficient for the Mohr circle to intersect the failure envelope. 2Θ in the compressive field is usually ~60˚, regardless of rock type (Byerlee, 1978). (D) If tensile strength is exceeded, the failure plane may be parallel to σ_1.

rocks that are subjected to σ_{diff} sufficiently high to cause a Mohr circle to intersect its failure envelope. In compression, Θ is typically 30˚ from σ_1, regardless of rock type; this is controlled by the angle of internal friction, which is effectively lithology-independent (Byerlee, 1978; Fossen, 2010). Rocks possess a small amount of tensile strength, shown by the parabolic portion of the failure envelope on the negative side of Mohr space (Fig. 4-4A). This implies that a rock is stable when a differential stress, albeit a small one, includes a negative principal stress. When a differential stress causes a Mohr circle to reach the tensile strength of a material, the angle between the line perpendicular to the tangent of this intersection and the x-axis (Θ) is zero; failure in the tensile field results in fractures that are parallel to σ_1 (Fig. 4-4D; Byerlee, 1978)

Two factors commonly affect the position of a Mohr circle constructed for brittle rocks behaving in the crust. First, a pore pressure (p_o) reduces all stress components by the same value, shifting the Mohr circle to the left, towards the failure envelope, by simple translation (Hubbert and Rubey, 1959). Second, when only one principal stress increases, one side of the circle will shift to the right along the x-axis of a Mohr diagram by σi units, and the other stresses will also change by a quantity $\nu\sigma_i$, where ν is the Poisson coefficient (Fig. 4-4C). Values for ν range from 0.25 to 0.29 for crustal material (Christensen, 1996). This change is not a simple translation of the circle along the x-axis, because the size of the circle will also change. Three basic stress environments occur in the crust: (1) tension, characterized by normal faulting (Fig. 4-5A); (2) compression, characterized by thrust faulting (i.e. reverse faulting; Fig. 4-5B); and (3) simple shear stress, characterized by strike-slip faulting (Fig. 4-5C; Anderson, 1951). These stress regimes can control the transport of felsic magma if the opening plane of magma-transporting dikes is along the σ_1- σ_2 plane (Fig. 4-5), as suggested by the magma-wedging model (Clemens and Mawer, 1992; Petford et al., 1993; Vigneresse et al., 1999).

Whether magma is transported along the σ_1- σ_2 plane (orange lines in Fig. 4-5A-C) or along the Andersonian failure plane (gray lines and planes in Fig. 4-5A-C), orientated ~30˚ from σ_1, depends partly on the intrinsic strength of the rocks through which magma is being transported (Fig. 4-5A-F), which controls the type of failure a rock will undergo with sufficient differential stress. Mode I fractures (e.g. opening

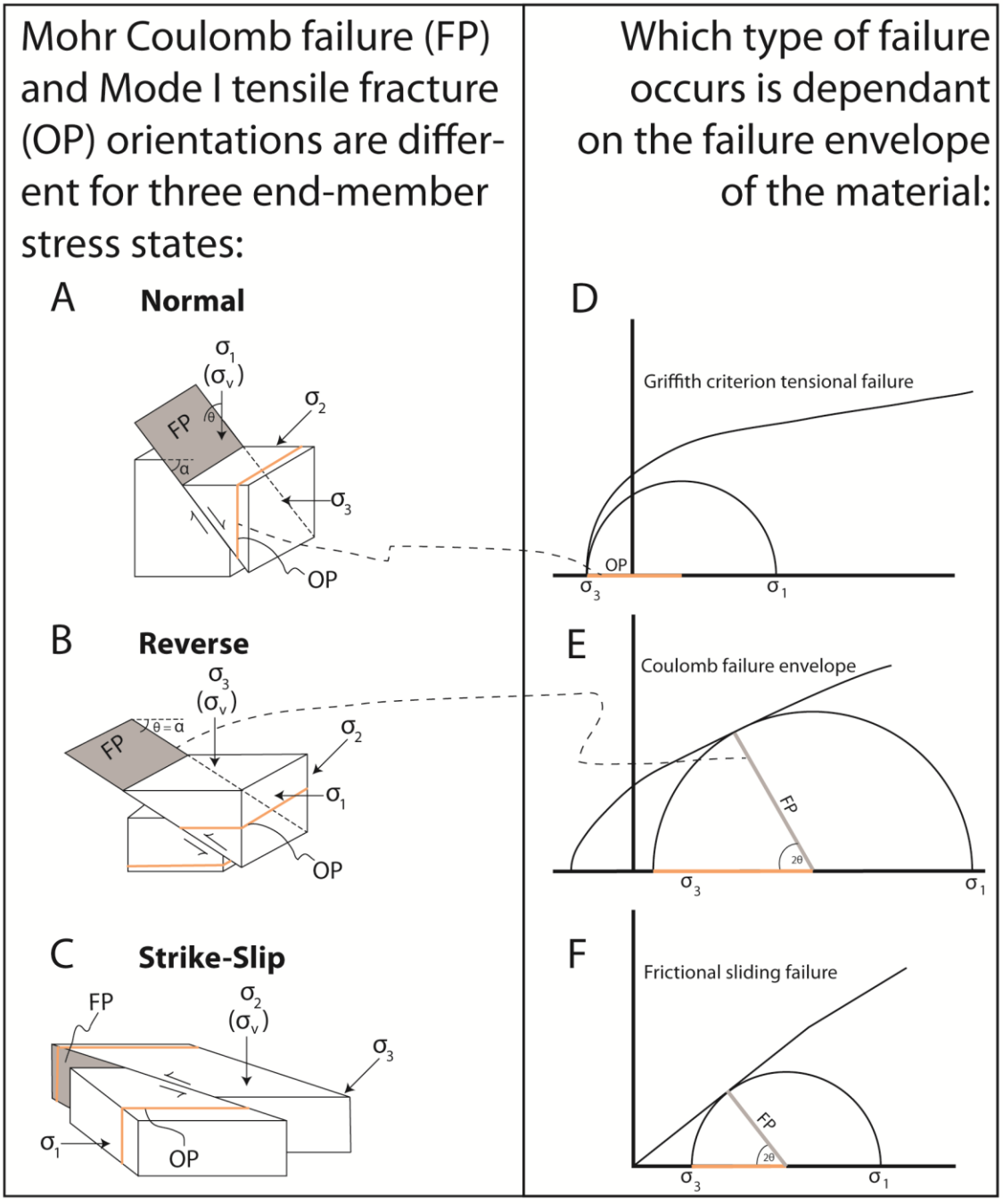

Figure 4-5. Explanation of opening-plane (orange lines, OP) orientation and failure planes (grey lines and planes, FP) using block diagrams and Mohr space. The three end-member faulting scenarios, (A) normal, (B) reverse, and (C) strike-slip (Anderson, 1951), result in a fracture plane is always oriented Θ ~30˚ from σ_1, where α is the dip of the fracture plane. This plane might be oblique to the σ_1- σ_3 magma wedging plane (OP; orange color) of Clemens and Mawer (1992), which open as (D) Griffith tensional fractures. (E) Coulomb failure results when a deviatoric stress is sufficiently high for a Mohr circle to intersect the failure envelope, resulting in 2Θ ~ 60˚ for all rock types (Byerlee, 1978). (F) Frictional sliding failure results when rocks contain preexisting weaknesses and no tensile strength.

planes in Fig. 4-5A-C) occur when rocks with tensional strength are subjected to differential stress sufficient for the Mohr circle to reach the tensile strength in Mohr space (Fig. 34-4A). Griffith cracks are microscopic preexisting fractures rocks which can contain a local stress field different than the overall applied stress field (Twiss and Moores, 1992). This local stress field is tensional, even during applied compression, allowing Mode I fractures to form even when confining pressure is high (Fig. 4-6). Mohr-Coulomb failure (e.g. failure planes in Fig. 4-5A-C) planes result when, during compression, differential stress is sufficiently high for the Mohr circle to reach the Coulomb failure envelope in the positive normal stress half of Mohr space (fracture planes in Fig. 4-5; Anderson, 1951). Rocks with preexisting weaknesses such as original sedimentary structures, a foliation, or a fault, may not possess any tensional strength,

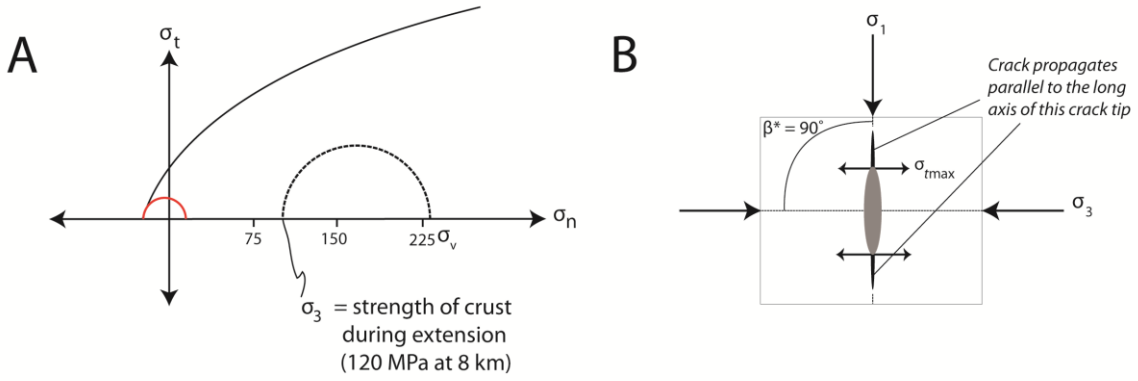

Figure 4-6. Explanation of *applied* versus *local* stress using crust in extension as an example. Crust experiencing extension with rocks at yield strength (Hogan et al., 1998) may result in a differential stress of ~ 110 MPa at 8 km depth. **(A)** This differential stress (dotted half circle with σ_v at 230 MPa and σ_3 at 120 MPa) is not enough to cause failure, as the Mohr circle is well within the stable field beneath the Mohr failure envelope of (Myrvang, 2001). However, **(B)** preexisting cracks with the proper orientation (β*) have a locally tensional stress field (σ_{tmax}) at their tips parallel to the least applied stress (σ_3). This local stress (solid red half circle) may plot in the tensional field of Mohr space and result in a Mode I fracture, though the applied stress (dotted half circle) is compressive and stable.

resulting in the frictional sliding envelope (Fig. 4-5F; Handin, 1969; Donath, 1972; Fossen, 2010), which has a slope of ~ 40˚ for $0 < \sigma_n < 200$ MPa and 31˚ for $\sigma_n > 200$ MPa, regardless of rock type (Byerlee, 1978).

Space for magma might not be directly accommodated by one of these types of failure. "Far field" space-creating mechanisms might have operated, such as the cantilever (Fig 4-7Ai.) or piston (Fig. 4-7B) mechanisms of Cruden (1998), may provide room for either Mohr-Coulomb fractures (Fig. 4-5B) or Mode I fractures (Fig. 4-5A) to form by displacing a fracture's host rocks vertically and/or horizontally (Tikoff et al., 1999; Tikoff and Vigneresse, 1999). In addition, source region compaction (Fig. 4-7C.) may have acted as a space-creating mechanism (Cruden, 1998). Other space creating mechanisms include emplacement into a dilatational fold hinge (i.e. a phaccolith; Fig. 4-7D), in-situ melting (Fig. 4-7E), and the classic ballooning of Ramsay (1989; Fig. 4-7F).

4.4.2 Magma driving pressure and principal stresses

Magma driving pressure exerts a hydrostatic stress that acts on the walls of the dike through which the magma is being transported (Weertman, 1971; Hogan et al., 1998). Because this force acts perpendicular to the dike walls, its net effect is to act on the total principal stress that is oriented perpendicular to the dike walls (Parsons and Thompson, 1991; Ablay et al., 2008). If an assumption is made that no free surface exists in the direction of this principal stress, P_d will serve to increase this stress. During extension, for a material experiencing a differential stress sufficient to cause failure, this serves to translate the Mohr circle to the right; Parsons and Thompson (1991) speculated on the ability of a magma to stabilize an otherwise unstable medium (e.g. to suppress earthquakes). The types of failure types are evaluated – along with the magma driving pressure – for CMG ascending through both an extending crust and a crust with a lithostatic stress state, and are discussed in Chapter 7.

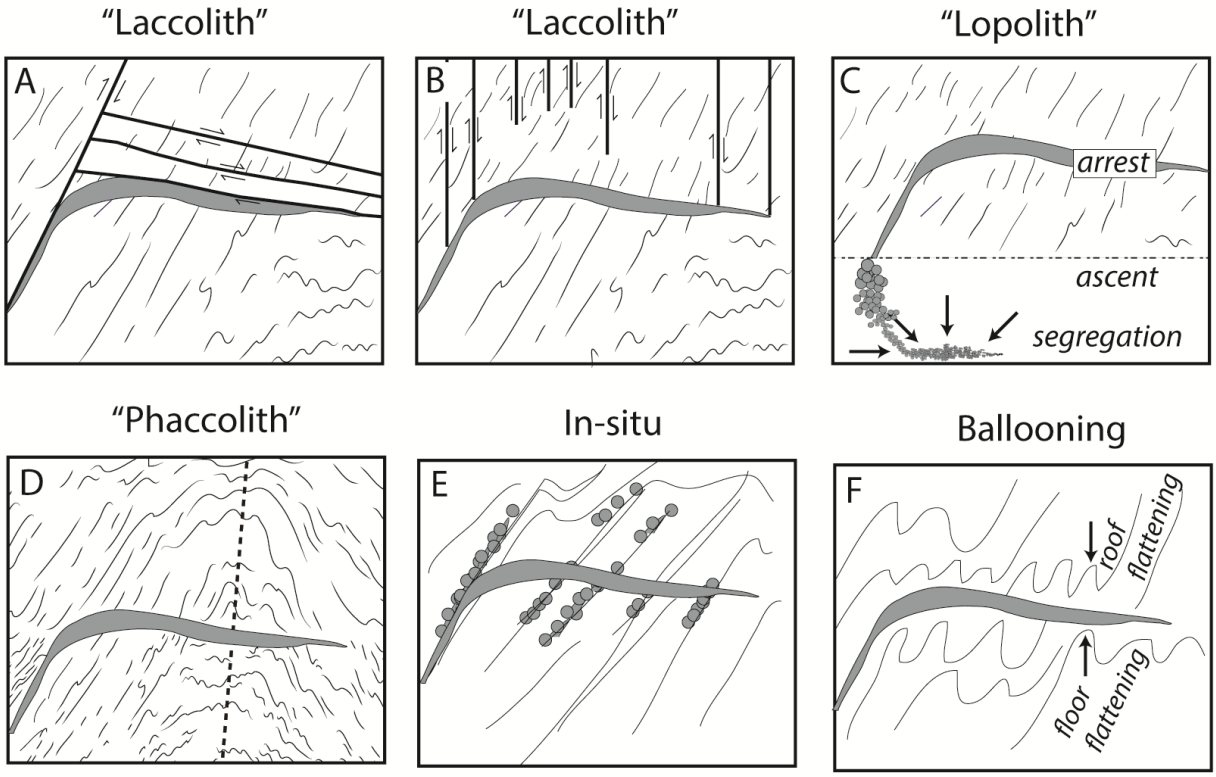

Figure 4-7. End member space creating mechanisms. A) Cantilever and B) piston roof lifting mechanisms of Cruden (1998), creating laccoliths. C) Source region compaction, causing floor subsidence and lopolith formation. D) Emplacement into a dilatational fold hinge, creating a phaccolith. E) Chen et al. (2007) argued that granitoids need not ascend far from their source, instead preferring in-situ melting, which makes the "room problem" negligible. F) Floor or roof flattening, or "ballooning" mechanism of Ramsay (1987). These processes may work individually or together, and be distributed or partitioned on all scales of the crustal column above or below the pluton.

4.5 Geochemistry

Bulk geochemical analysis of rocks can reveal subtle characteristics and patterns that cannot be observed in field or petrographic studies (Rollinson, 1993). Geochemical data from granitoid rocks are used to corroborate interpretations of the tectonic setting that accompanied emplacement (Frost et al., 2001). Furthermore, geochemical analyses can be used to quantitatively compare igneous rocks. The geochemistry of several CMG samples is analyzed following the methods described in Section 4.4.1; the data are presented and discussed in Chapter 9.

4.5.1 Methodology

Representative samples of CMG from different structural positions in the pluton were collected from the Curecanti Needle area for geochemical analysis (HBC10-18, 38, and 55 on Fig. 3-3). Care was taken to collect the freshest samples possible. After representative outcrops were identified and selected, samples were broken down into 10-15 cm diameter pieces and taken to The University of Tennessee, Knoxville. Equipment at The University of Tennessee, Knoxville was scrubbed with a wire brush, cleaned with acetone, and precontaminated by passing first bull quartz and a small amount of each sample through machinery before the "analysis-ready" sample was processed. The specimens were broken down with a "Chipmunk" jaw crusher, reducing them to pea-sized gravel. Finally, samples were powdered using a SPEX SamplePrep™ 8530 Shatterbox® equipped with a tungsten carbide grinding mill. Larger quantities (approximately 750 ml) of each specimen of CMG were powdered and mixed before filling a ~30 gram vial of each sample, ensuring the sample that was sent to a professional lab for whole-rock geochemical analysis was representative. The processed samples were analyzed at Activation Laboratories of Ancaster, Ontario. Activation Laboratories used inductively coupled plasma mass spectrometry (ICP-MS), total digestion inductively coupled plasma (TD-ICP), fusion methods mass spectrometry (FUS-MS), and instrumental neutron activation analysis (INAA) to determine the major, trace, and rare earth elemental compositions of the 3 samples. CIPW norms for each sample were calculated using an Excel spreadsheet (Hollocher, 2000).

4.5.2 Selection of samples

Three representative samples of CMG from the Curecanti Needle area were sampled, processed, and sent to Activation Laboratories for geochemical analysis (as described in Section 4.4.1). The samples, from west to east, are HBC10-39, -55, and -18. Sample HBC10-39 (2183 m above sea level) was selected as a representative sample of CMG near in the pluton's roof zone at Nelson Gulch, where the Curecanti pluton emerges from the Morrow Point Reservoir (Fig. 3-5). 2.8 km east-northeast of this, sample HBC10-55 (2317 meters above sea level) was sampled on the west ridge of Curecanti Creek canyon from one of a series of 20 m tall pinnacles, which are composed of CMG. Although the roof contact is not exposed at this location, ~300 m east, across Curecanti Creek canyon, is an excellent exposure of the pluton's floor and roof (the photo used in Fig. 3-4 was taken approximately 10 m uphill and east from sample HBC10-55). Cross-section construction delimits the Curecanti pluton to around 320 m thick at this location, making sample HBC10-55 120 m above the pluton floor (Figure 3-3). 450 meters southeast of HBC10-55, HBC10-18 (2225 m above sea level) was sampled from one of the subcyllindrical dikes structurally beneath the Curecanti pluton, thought to be related and originally connected to the main pluton (Hansen, 1964). The results of these analyses are discussed in Chapter 8.

CHAPTER 5
RESULTS OF FIELD WORK/MESOSCALE OBSERVATIONS

5.1 Nelson Gulch transect mesoscale observations

Of the three transects discussed above, the Nelson Gulch transect (NGT) contains the best exposures of the Curecanti pluton roof zone (upper 10 m of pluton) and core (all but the top and bottom 10 m), and the least accessible exposures of the pluton floor zone (lower 10 m of pluton; Fig. 3-6).

5.1.1 NGT/Curecanti pluton roof mesoscale observations

It is now apparent (Section 3.2.1) that the Curecanti pluton was first emplaced subparallel to the local S_2 foliation at Nelson Gulch, rotated horizontal, and intruded as the tongue-shaped body presently exposed in the Black Canyon of the Gunnison (Figs. 3-1 and 3-2). This is corroborated by observations along the Pioneer transect near the pluton roof and floor that show that CMG veinlets inject xenoliths subparallel to S_2 (see Sections 5.2.1 and 5.2.3). Stoping or foundering of roof/floor rocks is a common observation between most granitoid emplacement models, at least at some scale (Marsh, 1982; Hutton, 1996). A common mesoscale observation of granitoid plutons is that felsic material appears to infiltrate first along preexisting weaknesses in its host rocks (e.g. bedding, foliation, faults, etc.) as elongate "fingers" of magma, which eventually will connect (given enough infiltration), resulting in the process of stoping (Marsh, 1982; Hutton, 1996; Tikoff et al., 1999; Acocella, 2002; Bartley et al., 2012; Bons et al., 2012; Ferwerda, 2012; Pownall et al., 2012).

The Curecanti pluton lacks a mesoscopic foliation at this location. Numerous large angular xenoliths, composed of layered gneiss, mesoscopically identical to the gneisses 50 m west above the pluton, are surrounded by CMG in the roof zone of the pluton (Fig. 3-5), consistent with the roof zone exposed in the Pioneer transect (Section 5.2.1). These xenoliths have clearly rotated from some original orientation, as just west of the Nelson Gulch roof contact, S_2 is oriented 330˚, 60˚ SW. However, some

xenoliths suspended by CMG have a near-vertical fabric, and the fabric in other blocks is subhorizontal (Fig. 3-5).

5.1.2 NGT/Curecanti pluton core mesoscale observations

1 km east of A', cross section A'-A" crosses CMG for 1.7 km. This mass of CMG, sporadically exposed near the canyon rim, and well exposed, but inaccessible in the steep walls of the canyon (Figs. 3-5 and 3-6), provides an oblique transect through the pluton core (Fig. 3-3). CMG does not contain a foliation or xenoliths in the core of the Curecanti pluton along this transect, but appears as a fine-grained, homogeneous monzogranite. A series of NW-trending (305-320˚) Ordovician diabase dikes cross-cut the Curecanti pluton core along the NGT (Fig. 3-3), providing reference-planes that assist in reconstructions of pluton geometry (Fig. 3-2). Near the location where diabase cross-cuts CMG along the NGT (Fig. 3-3), no xenoliths or microgranitoid enclaves exist in the Curecanti pluton.

5.1.3 NGT/Curecanti pluton floor mesoscale observations

The floor of the Curecanti pluton, as exposed 2.3 km east of Nelson Gulch (Fig. 3-6), does not contain a mesoscale foliation or xenoliths of quartzofeldspathic gneiss that are suspended by CMG. A contact between CMG and p_gm was documented along the NGT to be 292˚, 70˚ NE near a diabase dike, then turns to subhorizontal 50 m east (Fig. 3-6). 350 m east of this observation, sample HBC10-25 was sampled from the canyon rim; this sample comes from 75 m up from the Curecanti pluton floor (Fig. 3-6), and does not contain a mesoscale foliation. Petrographic observations for this sample are discussed in Section 6.1.2.

5.1.4 NGT/Curecanti pluton host rock mesoscale observations

As discussed in Section 2.2.1, this portion of the Black Canyon of the Gunnison is dominated by quartzofeldspathic paragneiss and migmatite. The western edge of the NGT is no exception, and the gneiss in contact with CMG in Figure 3-5 is layered quartzofeldspathic gneiss with an S_2 foliation oriented 330˚, 60˚ SW. However, this location also contains a very small (not resolved on map scale) outcrop of garnet +

sillimanite + muscovite schist (e.g. HBC10-5). Microscale observations of this sample are discussed in Section 6.1.3.

5.2 Pioneer transect mesoscale observations

Contrary to the NGT, the PT provides both the most accessible and most complete data set on CMG (Figs. 3-1 and 3-3) by access along the Curecanti Creek trail, which traverses through the entire Curecanti pluton. The trail heads north from Pioneer Lookout Point along the cliff line, then switchbacks though the pluton near where it intersects Curecanti Creek (Fig. 3-4). It should be noted that, while the Curecanti pluton roof contact is generally subhorizontal, there is a large cupola-shaped deflection in the roof at Pioneer Lookout Point (Fig. 3-4). Hansen (1964) interpreted this undulation in the pluton roof contact, resulting in a very steep roof contact just west (left in photo) of Pioneer Lookout point (Fig. 3-4), as an infilling of magma as a roof pendant was rafted from the pluton's roof.

5.2.1 PT/Curecanti pluton roof mesoscale observations

The roof zone of the Curecanti pluton, as exposed on a ridge 500 m southwest of Curecanti Needle, is exposed as a pavement outcrop (Figs. 5-1A). CMG here does not contain a mesoscopic foliation, but abundant xenoliths and/or microgranitoid enclaves were observed and are described here. Some of these blocks (e.g. Fig. 5-1B) are quartzofeldspathic gneiss whose foliation is preserved; these blocks are identical to the quartzofeldspathic gneiss in contact with the Curecanti pluton roof at Nelson Gulch and the xenoliths just beneath the roof contact (see red arrows of Fig. 3-5). CMG clearly injects blocks subparallel to the foliation within these xenoliths (Fig. 5-1C). More wispy mafic blocks were also observed that do not have a clear internal foliation (Fig. 5-1D) and resemble microgranitoid enclaves, features described in detail by Paterson et al. (2004). Microgranitoid enclaves here do not have an internal mesoscopic foliation and have aspect ratios between 2:1 (Fig. 5-1D) and 1:1 (Fig. 5-1E). Interestingly, these enclaves have asymmetric rims of light-colored CMG (e.g. Fig. 5-1D) that define a planar

Figure 5-1. Various stages of xenolith/microgranitoid enclave assimilation observed within 10 m of the Curecanti pluton roof contact (insets i. and ii. show reference map with location of pictures as red star). (A) View to the west of approximate field of view from which photos B-F are sourced; 30 cm-long hammer for scale in all photos; 3 m-wide, EW-striking, vertically dipping pegmatite dike can be seen cross cutting CMG at this location. (B) 40 cm-long xenolith of quartzofeldspathic gneiss (thin black line) likely derived from the Curecanti pluton roof and rafted into pluton; CMG can be seen injecting along foliation (arrow; foliation is S_2 if this is a locally derived piece of gneiss wedged from the pluton roof); location of close-up in C outlined. (C) Close up of B showing CMG clearly injecting parallel to the foliation in the xenolith (dashed line). (D) Wispy microgranitoid enclave (thin black line) with no discernible internal foliation, but asymmetric rim of more felsic CMG (dashed outline) defines a steeply dipping foliation along this pavement outcrop (average orientation: 282˚, 85˚ NE). (E) Subrounded mafic granitoid enclave (thin black line) dissected by CMG. (F) Foliated gneiss (thin black line, foliation highlighted with dashed line) suspended by CMG with felsic reaction rim (dashed outline); CMG injects approximately along what would be S_2 if this is a locally derived gneiss.

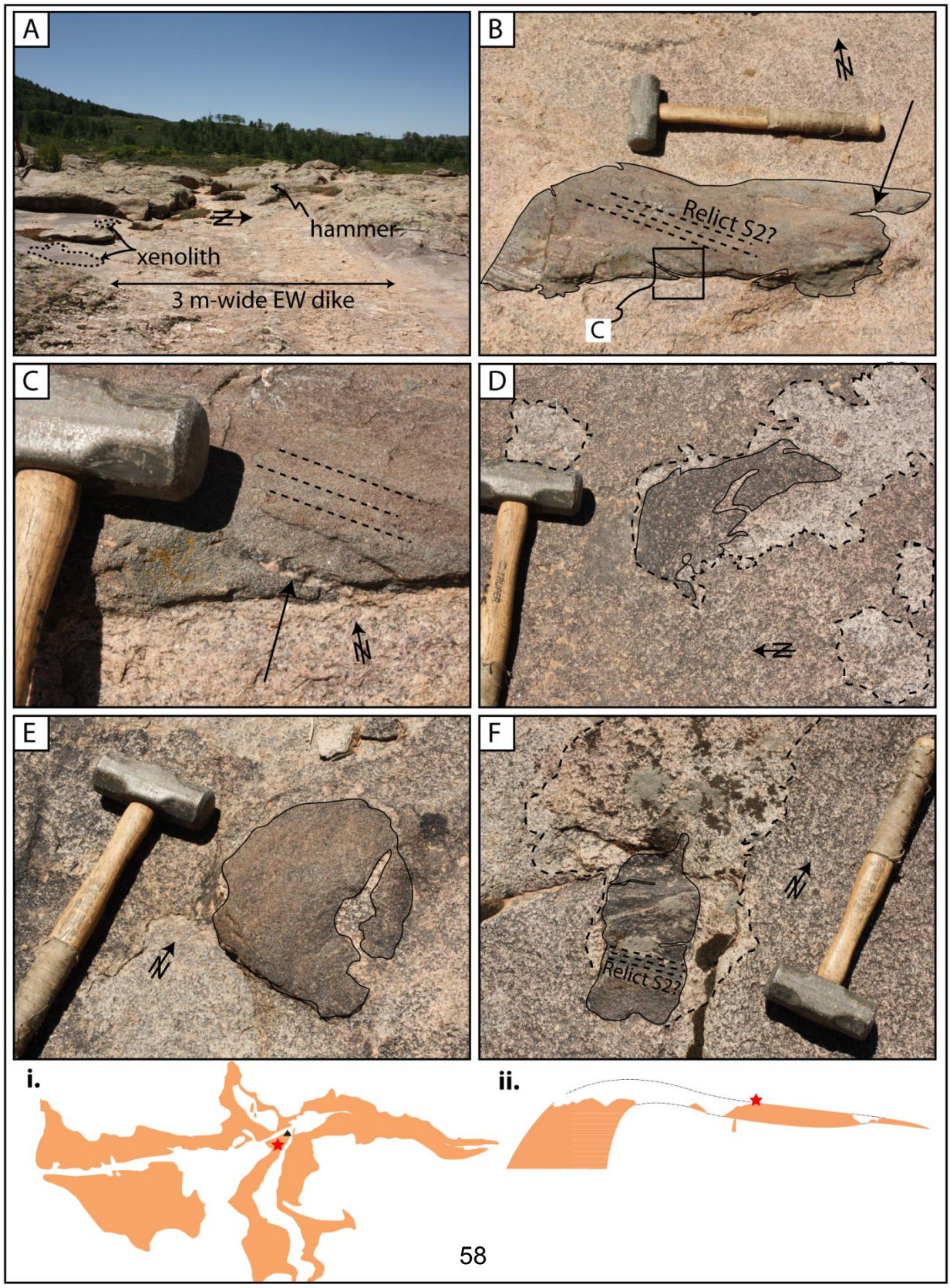
A
hammer
xenolith
3 m-wide EW dike
B
Relict S2?
C
C
D
E
F
Relict S2?
i.
ii.

fabric dipping steeply to the northeast (average orientation: 298˚, 86˚ NE). These rims are not exclusive of wispy microgranitoid enclaves, and were also documented around tabular xenoliths of quartzofeldspathic gneiss (Fig. 5-1F). Also exposed at this location are several 3 m-wide, east-west-striking, vertically dipping pegmatite dikes that cross-cut CMG (Fig. 5-1A). These pegmatite dikes (see Fig. 6 using inset i. of Fig. 5-1 for approximate location) have an average orientation of 272˚, 90˚ (n=6).

The roof zone of the Curecanti pluton should also be exposed at Pioneer Lookout Point, where a cupola of CMG intersects a tourist overlook (Fig. 3-4). Although the roof contact of the Curecanti pluton was mapped at the overlook, no foliation, xenoliths, or microgranitoid enclaves were observed in CMG exposures here.

5.2.2 PT/Curecanti pluton core mesoscale observations

The core of the Curecanti pluton is accessed by the Curecanti Creek trail as it switchbacks from the canyon rim to Morrow Point Reservoir. Characteristics of the pluton core are represented by sample HBC10-55: non-foliated, homogeneous, garnet-bearing monzogranite (Fig. 5-2). No xenoliths or microgranitoid enclaves exist in this portion of the pluton. Petrographic observations in the pluton core do reveal some strain

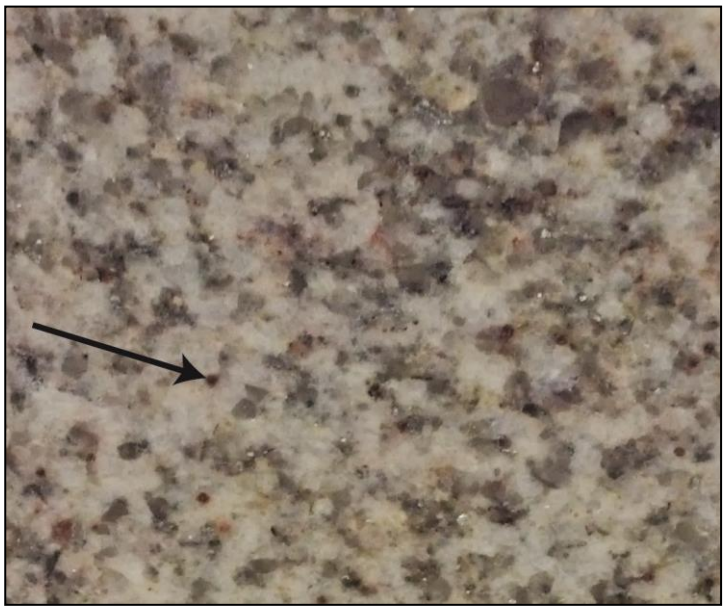

Figure 5-2. Sample HBC10-55 (see Fig. 3-3 for location) showing fine grained homogeneous CMG representative of the Curecanti pluton core; arrow is 1 centimeter-long and identifies a subhedral magmatic garnet.

accumulation, however, and are discussed in Section 6.2.3.

5.2.3 PT/Curecanti pluton floor mesoscale observations

The floor of the Curecanti pluton, exposed above the confluence of Curecanti Creek and the Morrow Point Reservoir (Fig. 5-3A), has an average orientation of 315˚, 33˚N along the PT. The floor zone is characterized by a weak foliation defined by the alignment of millimeter-scale biotite porphyroblasts (Fig. 5-3B), which can only be reliably measured in the field along the Curecanti pluton floor contact and correlative dikes beneath the pluton along this transect. 48 measurements of foliations in CMG yield an average plane of 272˚, 30˚N (Fig. 5-3C) with a 67˚ dihedral angle between this plane and the average S_2 plane along the PT. There is a 23˚ dihedral angle between the average CMG foliation plane and the Curecanti pluton contacts, and an 83˚ dihedral angle between the pluton contacts and local S_2. In addition, decimeter-scale xenoliths at the pluton's floor yield approximately the same orientation (Fig. 5-3D). The similar orientation measured by these two types of fabric in the field support the interpretation that biotite was aligned during magmatic flow rather than by gravity settling or due to tectonic stress (Tobisch et al., 1997). Also at the Curecanti pluton floor along the PT are instances where CMG veinlets connected to the pluton above are both parallel- and oblique-to S_2 in the host rock just beneath (Fig. 5-3E), similar to the observation made in the Curecanti pluton's roof zone (Section 5.2.1 and Fig. 5-3).

5.2.4 PT/CMG dikes mesoscale observations

Along the PT, there are two small dikes of CMG structurally beneath the Curecanti pluton (Fig. 3-3). The weak foliation mapped in these dikes is subparallel to the foliation mapped in the floor zone of the Curecanti pluton, and, as such, foliation data from these dikes are included on the stereonet in Fig. 5-3D. The average foliation plane for the biotite aggregates is 288˚, 31˚N (Fig. 5-4A, n=27). The dikes have gently dipping "roofs" (330˚, 15˚ NE), subvertical margins (70-85˚), aplitic border phases, and biotite-rich margins (Fig. 5-4B). Their geometry is hereby interpreted as sybcyllindrical. Fine-grained border phases are a common feature reported in igneous

Figure 5-3. (A) The floor of the Curecanti pluton (black line) in Curecanti Creek canyon is discordant with respect to S2 (dashed black lines) in the gneiss beneath CMG. A 5 m by 3 m block of floor material is seen near the center of the photograph completely supported by CMG. Location of E is shown with black box. (B) Subtle foliation (dashed black lines) in CMG from the floor of the Curecanti pluton (see insets i. and ii. for location) with an orientation of 264˚, 35˚N here. (C) Lower hemisphere equal area projection of poles to planes of Curecanti pluton floor and roof contacts from the Curecanti Needle area (x's), contacts of correlative dikes beneath the pluton (open circles), CMG foliations measured in both the pluton and correlative dikes beneath the pluton (black squares), and average orientation of aforementioned fabrics (dashed and solid lines, respectively) and S2 in quartzofeldspathic gneisses (dotted line) around Curecanti Creek. There is a 63˚ dihedral angle between the average CMG foliation plane and average S2 plane, and 23˚ dihedral angle between the average CMG foliation plane and the Curecanti pluton contacts. Intersection lineations are indicated by the red triangle (29˚ →010˚), green triangle (26˚ →325˚), and blue triangles (13˚ →335˚). D) Tabular xenoliths of floor gneiss (black lines) with relict foliation (dashed lines) suspended and dissected by CMG subparallel to preexisting foliation; 30 cm-long hammer for scale. (E) CMG veinlets connected to the Curecanti pluton (upper right part of photo) both parallel- and oblique-to S2 in host gneiss (dashed lines).

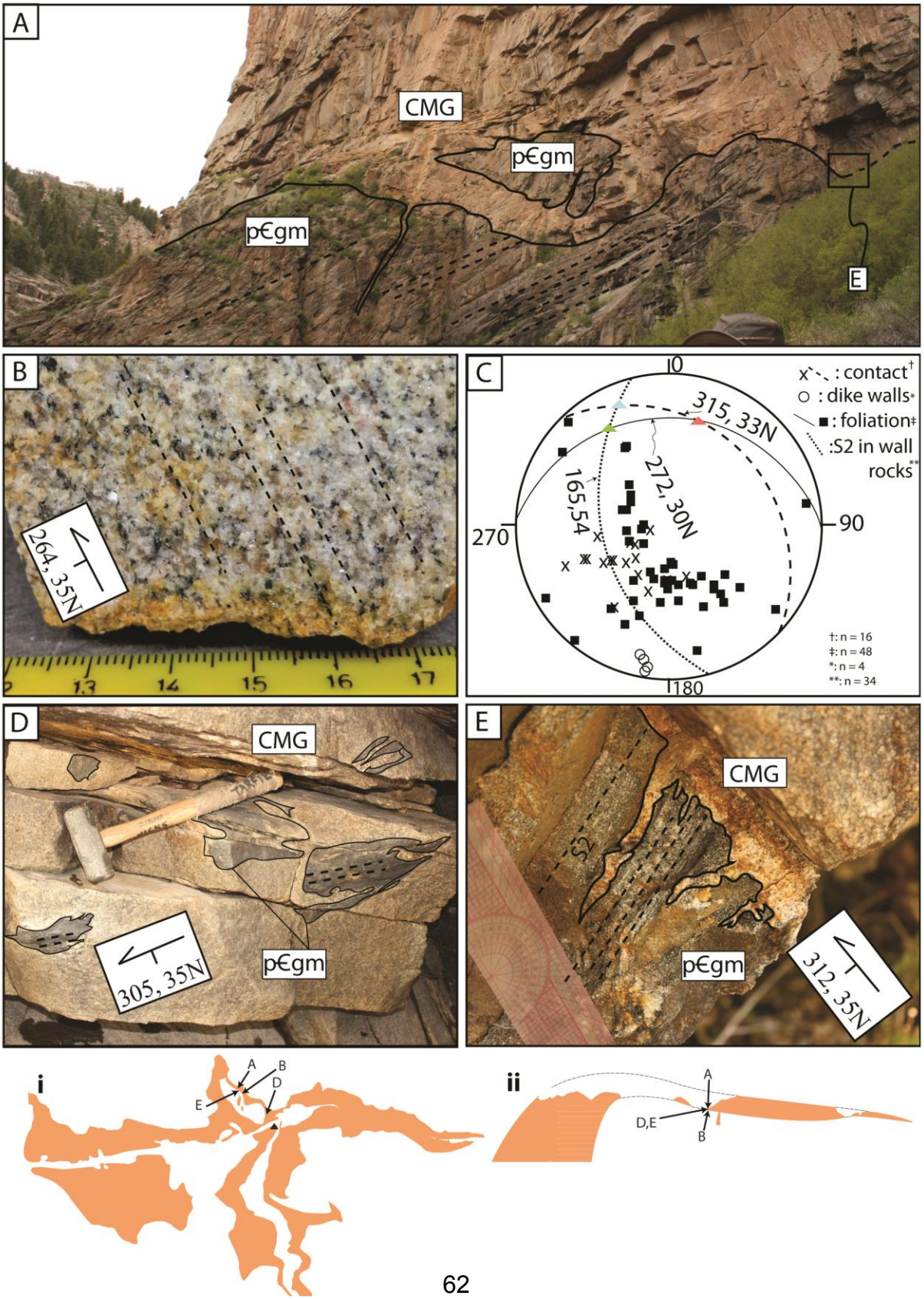
A
CMG
p€gm
p€gm
E
B
264, 35N
C
0
315, 33N
272, 30N
165,54
270
90
180
: contact†
: dike walls*
: foliation‡
:S2 in wall rocks**
†: n = 16
‡: n = 48
*: n = 4
**: n = 34
D
CMG
305, 35N
p€gm
E
CMG
S2
p€gm
312, 35N
i
A
B
D
E
ii
A
D,E
B

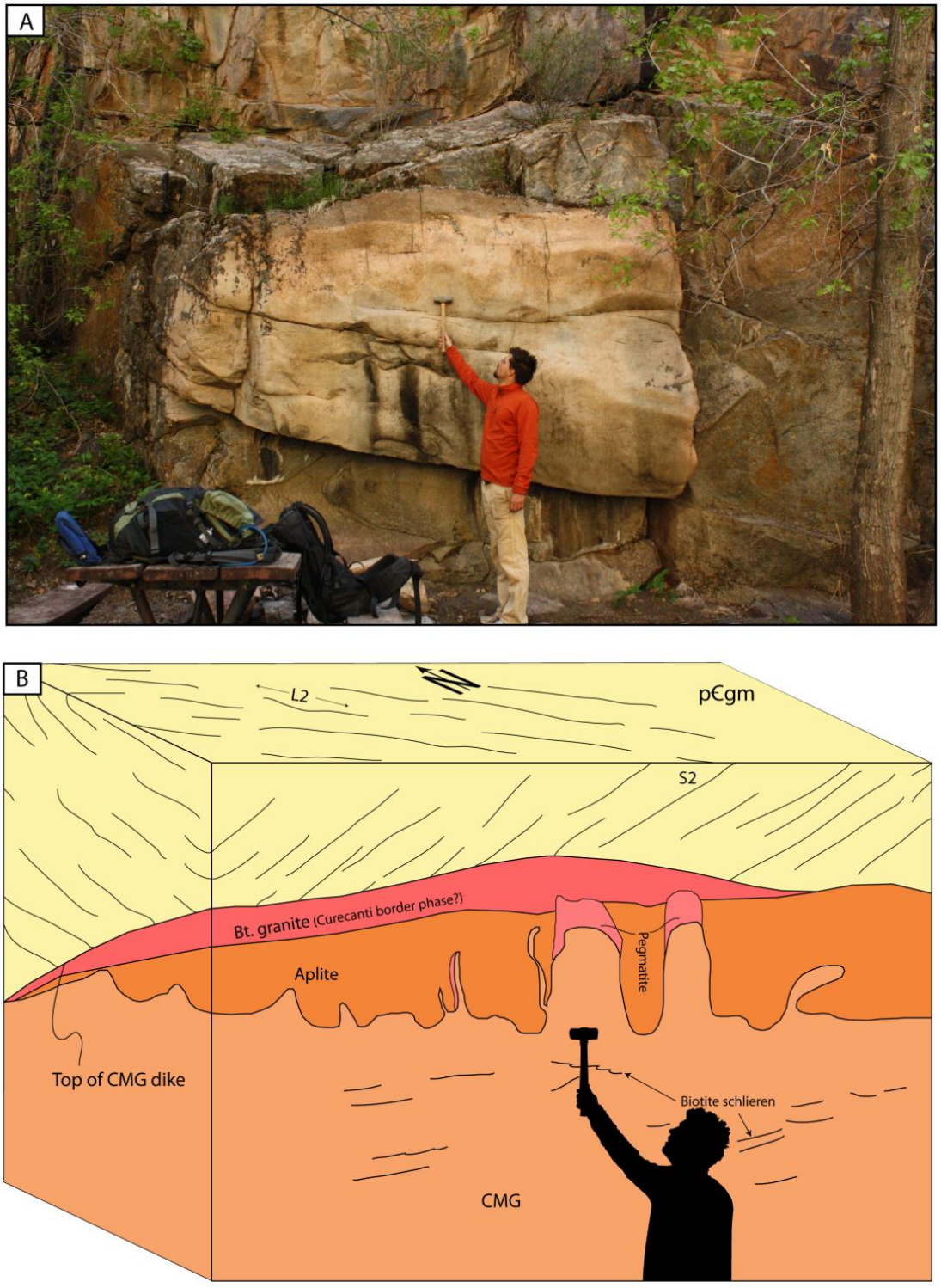

Figure 5-4. (A) Photograph (view to the northeast)and (B) line drawing of a representative CMG dike located along Curecanti Creek at ~2194 m. Colors consistent with other figures. CMG dike has a shallowly dipping roof, a layered biotite granite and aplite border phase, and contains numerous biotite schlieren (average orientation of schlieren in this dike: 288˚, 31˚ N; n=27).

bodies, and likely reflect more rapid cooling of magma directly in contact with relatively cold host rocks (Huppert and Sparks, 1989).

5.2.5 PT/Curecanti pluton host rock mesoscale observations

Along the PT, quartzofeldspathic gneisses have a local S_2 that is oriented, on average, 165˚, 54˚ SW (n=34; Fig. 5-3C). This foliation is cross-cut by CMG (Fig. 5-3A). A curious set of steeply dipping (ca. 85˚ NW), northwest-striking lamprophyre dikes is exposed along the PT below and above the Curecati pluton (Fig. 3-3) and contain a margin-parallel foliation. These lamprophyre dikes cross-cut the fabric in the host migmatite and gneiss, but are cross-cut by CMG, and their age is thus bracketed between the presumed age of migmatites and fabric development (1.7 Ga) and the emplacement of the Curecanti pluton at 1420 ± 15 Ma. Because of their proximity and cross-cutting relationship with the Curecanti pluton, paired with their aluminous composition, these may make a good target for future thermobarometry of the Curecanti Needle area (Chapter 11).

5.3 Chipeta transect mesoscale observations

Chipeta Falls cuts through the Curecanti pluton approximately 1.75 km east of where Curecanti Creek empties into the Morrow Point Reservoir (Fig. 3-3). As mentioned in Section 3.3.4, the floor of the Curecanti pluton is presently beneath the Morrow Point Reservoir, but was mapped by Hansen (1971) prior to reservoir flooding, so it is known that samples collected at the level of Morrow Point Reservoir (e.g. HBC10-38 at 2182 m above sea level) are 20 m above of the pluton floor contact.

5.3.1 CT/Curecanti pluton roof mesoscale observations

The roof zone of the pluton is different here than along the PT. There are no xenoliths or microgranitoid enclaves as there are along the ridge 500 meters southwest of Curecanti Needle along the PT (Fig. 5-1) and suspended in the roof zone of the Curecanti pluton along the NGT (Fig. 3-5). CMG here is non-foliated, fine grained, and lacks garnet (Fig. 5-2). There are, however, numerous 3-5-cm-thick aplitic veinlets that cross-cut the Curecanti pluton and its host quartzofeldspathic gneiss (Fig. 5-5).

5.3.2 CT/Curecanti pluton core mesoscale observations

As mentioned in Section 5.3, the Morrow Point Reservoir has a typical elevation of 2182 m above sea level, ~20 meters above the Curecanti pluton floor along the CT, which makes any sample from this area in the Curecanti pluton core. HBC10-38 (Fig. 3-3) is a garnet-bearing monzogranite without a foliation. No xenoliths are visible in the Curecanti pluton core in this area (Fig. 5-6).

5.3.3 CT/Curecanti pluton floor mesoscale observations

The floor contact of the Curecanti pluton is subhorizontal along this transect, as mapped by Hansen (1971), and is discordant with respect to the host rock macroscopic foliation. However, it is presently 20 m below the level of Morrow Point Reservoir (Fig. 5-6; Hansen, 1971).

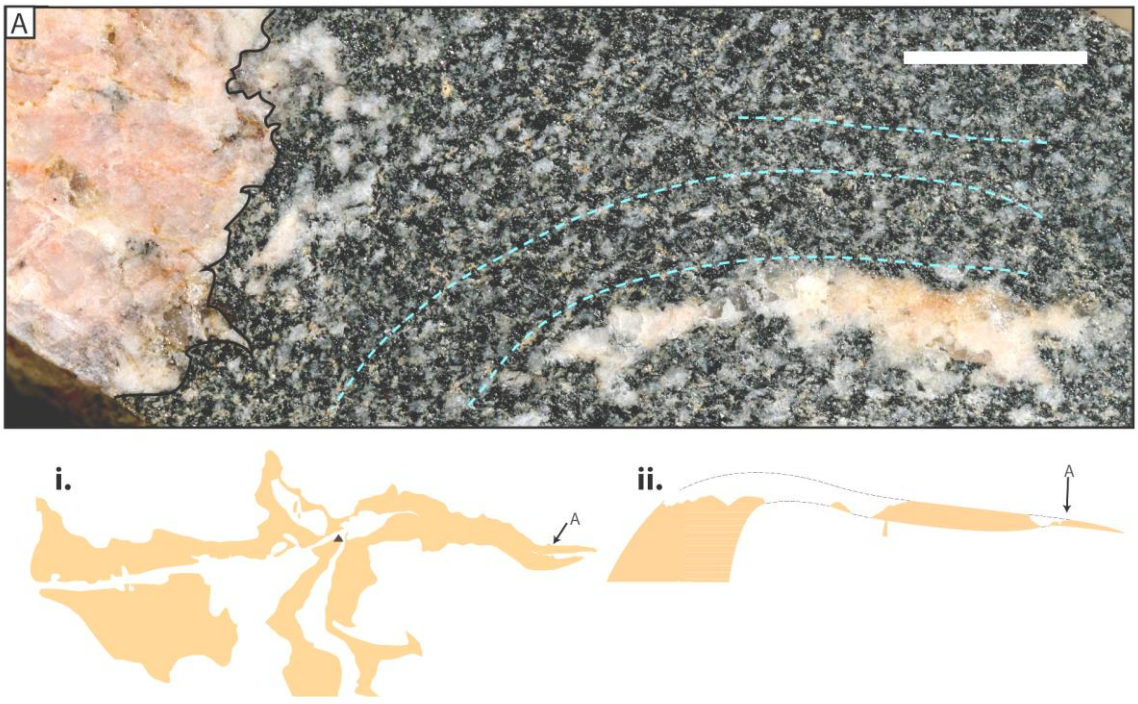

Figure 5-5. (A) Photograph (view to the east) of aplite veinlet (orientation: 271˚, 85˚N), near Chipeta Falls, cross cutting the host gneisses foliation (dashed blue lines), which is gently folded. This photograph was taken 10 m above the Curecanti pluton roof. Insets i. and ii. show location of A.

Figure 5-6. Photograph (view to the north) of Chipeta Falls (46 m-tall), which is composed of CMG in the core of the Curecanti pluton, showing Morrow Point Reservoir (base of photo), distance to the Curecanti pluton floor contact, distance to the agmatite zone (Section 6.3.4), location of sample HBC10-38, and lack of xenoliths/microgranitoid enclaves.

5.3.4 CT/Curecanti pluton host rock mesoscale observations

The Curecanti pluton decreases in thickness from 213 m in the Pioneer Lookout wall (Fig. 3-4) to 90 meters along the CT (Fig. 3-3). ~1 km east of Chipeta Falls, the roof of the Curecanti pluton dips ~5˚ E and submerges beneath the Morrow Point Reservoir (Fig. 5-7). 500 m east of this (1.5 km east of Chipeta Falls), a brecciated zone of quartzofeldspathic migmatite and gneiss was observed (Fig. 5-8). This breccia contains feldspathic leucosome surrounding angular blocks of gneiss, consistent with "agmatite," a migmatitic structure described by Mehnert (1968). These migmatite breccias are interpreted to form during local melting and rapid volume increase (Mehnert, 1968), but little modern research has focused on them (Ma, 1948) since they were first described by Sederholm (1923). However, some authors have suggested they form in the aureoles of plutons and sills (Hill, 1988; Shervais, 2005; Anhaeusser, 2010). The leucosome of agmatite along the CT is not foliated, but generally parallels S_2 where this zone is located (Fig. 5-8). This texture may have formed due to migmatization during formation of the gneisses (Mehnert, 1968), during local folding (i.e. the Curecanti Antiform), or due to the intrusion of the Curecanti pluton; without further timing constrains, the significance of this agmatite zone remains a question.

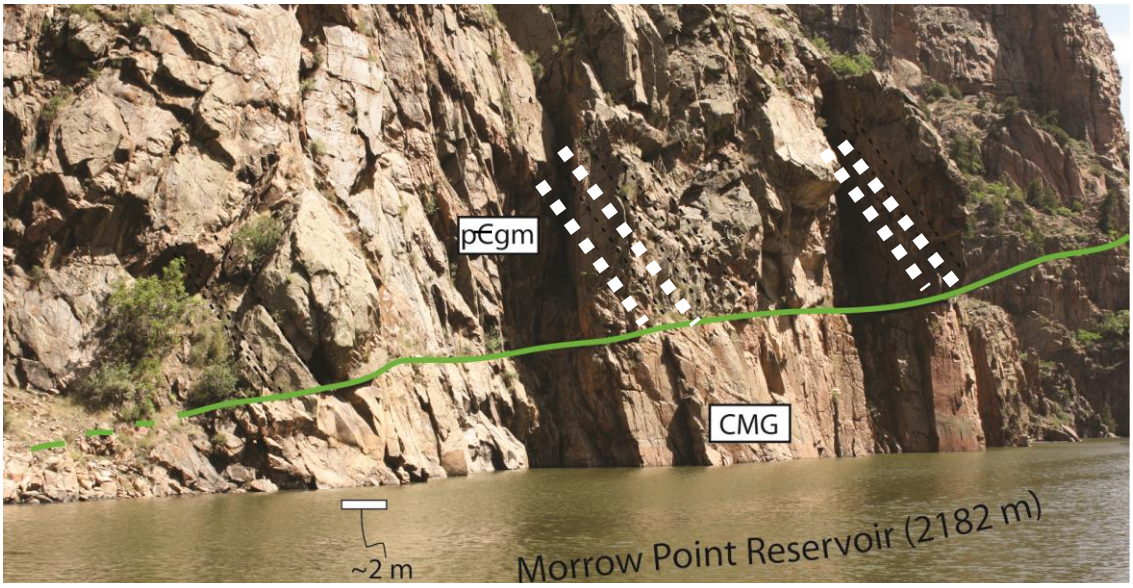

Figure 5-7. View to the southeast of Curecanti pluton roof (green line) as it dips beneath the Morrow Point Reservoir ~1 km east of Chipeta Falls. Note discordance of roof with respect to the foliation in the host rock (dashed white lines) and lack of xenoliths in the Curecanti pluton near the roof at this location.

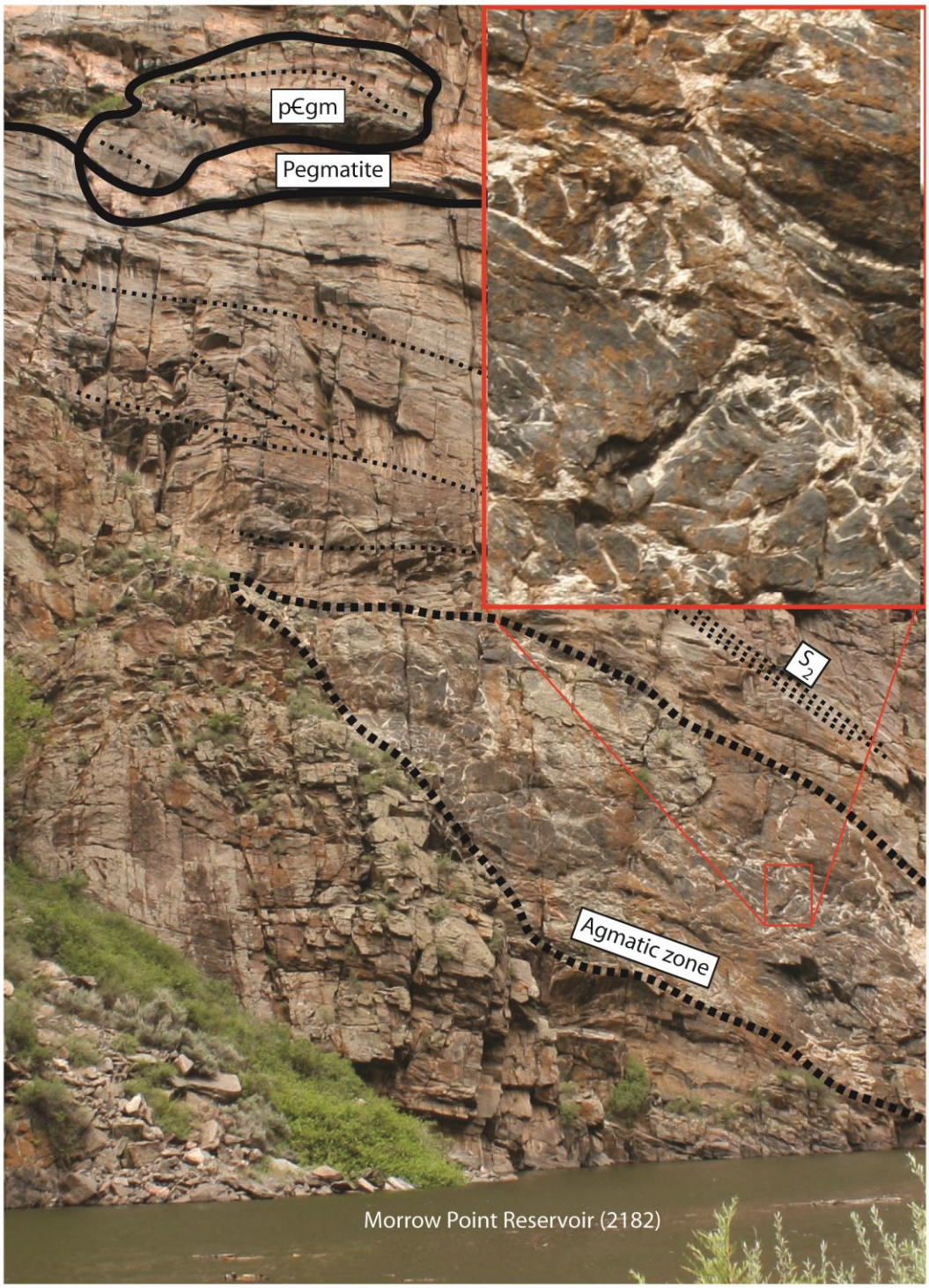

Figure 5-8. View to the north-northeast of Morrow Point Reservoir and a 10-m-thick wedge-shaped agmatite zone (bold dashed lines) within p€gm 1.5 km-east of Chipeta Falls. Inset: core of agmatite zone shown larger (red lines show location of enlargement) where brecciation of gneiss is apparent. A 2 m-thick pegmatite is seen in the upper left of the photo, 15 m-above the agmatite zone. Agmatite zone is approximately parallel with S_2 (thin dotted lines) at this location. Note that S_2 is now dipping southeast.

5.4 Host rocks of the Curecanti pluton mesoscale observations summary

Host rocks of the Curecanti pluton have a consistently quartzofeldspathic lithology, and consist of migmatites and gneisses (Fig. 3-1). Migmatites are hereby and elsewhere defined as composite rocks consisting of one part melanosome (mafic-rich; dark-colored, sensu lato) and one part leucosome (quartz and feldspar-rich; light-colored, sensu lato; (Mehnert, 1968; Burg and Vanderhaeghe, 1993; Vanderhaeghe, 1999; Brown, 1994; Brown et al., 1995; Hall and Kisters, 2012). Gneisses are almost exclusively quartzofeldspathic in the Curecanti Needle area, with the exception of one outcrop composed of garnet-sillimanite schist, located just west of the Nelson Gulch CMG contact (HBC10-5; Fig. 5-9A). More commonly, layered gneisses are moderately dipping in the Curecanti Needle area (Fig. 5-9B). The fabric within these migmatites ranges from nebulitic (Fig. 5-9A) to agmatic (Fig. 5-8) to ptygmatic/stromatic (Fig. 5-9C) to opthalmatic (Fig. 5-9D; Mehnert, 1968).

Along the CT, the fabric within the gneiss and migmatite (i.e. p_gm) undergoes a transition. From 4 km west of Nelson Gulch to Nelson Gulch, S_2 has an average orientation of 182, 54W, and from Nelson Gulch to Chipeta Falls, the orientation of S_2 remains fairly consistent with this (average S_2: 164˚, 54˚SW; Fig 5-10). However, east of Chipeta Falls, S_2 begins to dip southeast and northeast (average S_2: 308˚, 56˚NE), and, in places, is subhorizontal (Fig. 5-5). This area marks the hinge zone of the Curecanti antiform, a km-scale fold first described by Hansen (1964). Using all of the S_2 data collected in the field (n=190), a beta axis (β in Fig. 5-10) calculated for the Curecanti antiform plunges 18˚ towards 319˚, consistent with the general orientation of F_2 folds in the Black Canyon of the Gunnison region, as described by Jessup et al. (2006; Fig. 2-1). The beta axis (β’ in Fig. 5-10) defined by the intersection between two S_2 domains (east of the Chipeta Falls domain and within the area of the Curecanti pluton) plunges 17˚ towards 321˚ and has a 6˚ dihedral angle from the beta axis calculated from the S_2 compilation, within the error of measurements taken with a Brunton compass. Interestingly, the beta axis (β) calculated for all the S_2 measurements collected in the field

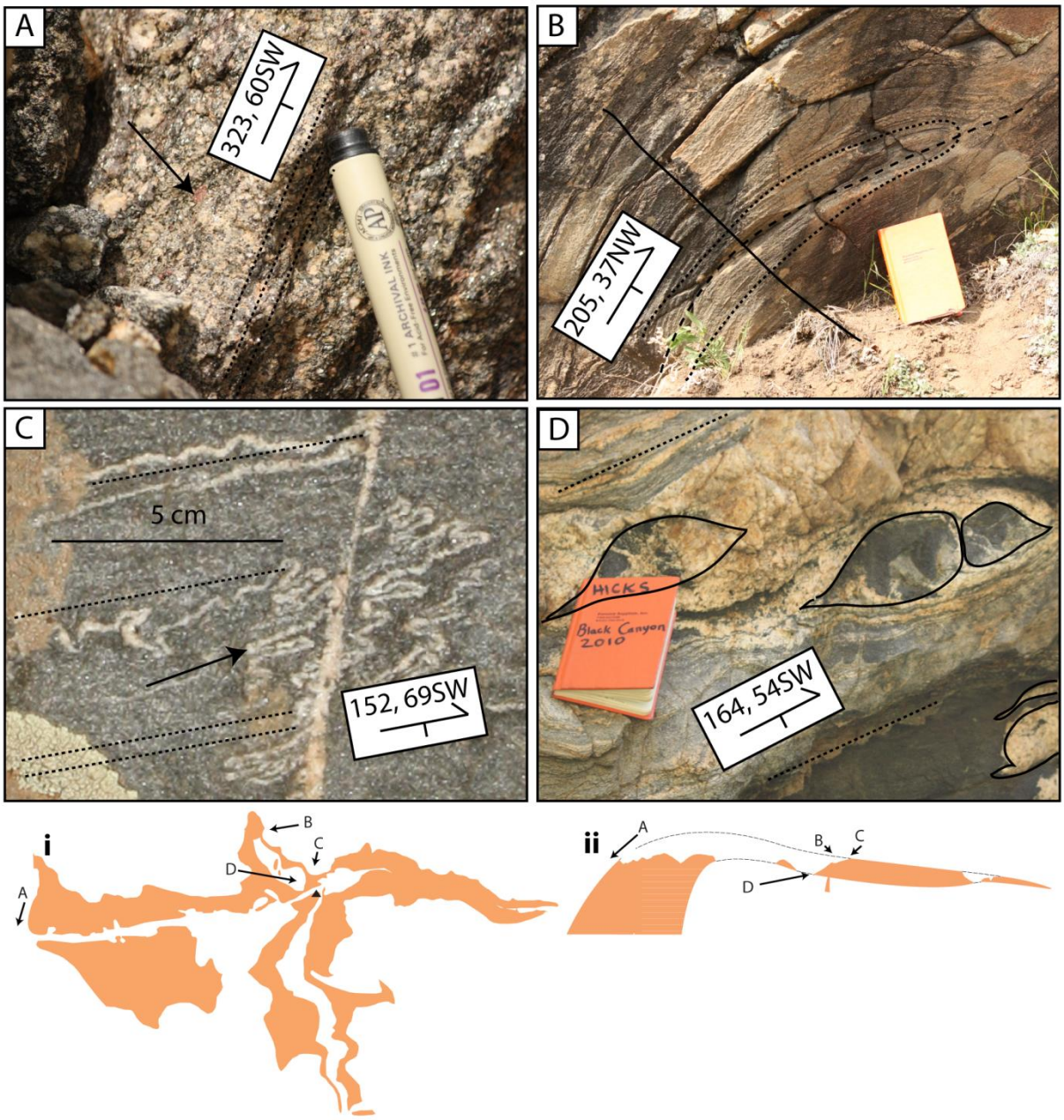

Figure 5-9. Photographs of structures in the host gneisses and migmatites to the Curecanti pluton. (A) Foliated (dotted lines and S_2 measurement) garnet (arrow) + sillimanite schist located in Nelson Gulch (see inset i. and ii. for location information). (B) Typical foliated quartzofeldspathic gneiss, and atypical isoclinal fold, of the Curecanti Needle area with S_2 (dotted line and measurement) and F_2 axial plane (dashed line); S_2 is folded (axial plane of F_3 fold in black line), but an S_3 foliation was not observed. This is the only location where an F_2 hinge was observed, and F_2 measured here is 16˚→295˚. (C) Ptygmatic leucosome (arrow; S_2 is dotted line and measurement) near Pioneer Lookout Point. (D) Opthalmatic migmatite (S_2 as dotted line with measurement), with melanosome outlined in black, near the confluence of Curecanti Creek and Morrow Point Reservoir.

(Fig. 5-10) is similar to an F_2 fold axis measured in Curecanti Creek (Fig. 5-3B); however, this was the only F_2 fold axis observed in the field.

5.5 Mesoscale observations summary

The Curecanti pluton ascended some distance subparallel-to the local S_2 (Section 5.1.1), turned horizontal, and was emplaced as a tongue-shaped sheet with a maximum thickness of ~400 m (Fig. 3-1). Along the long axis of the pluton, its thickness tapers to 90 m near Chipeta Falls and appears to pinch out in the hinge zone of the "Curecanti antiform" of Hansen (1964) and Jessup et al. (2005; Fig. 2-2).

A mesoscopic foliation defined by the planar alignment of biotite is measurable in CMG only in the floor zone of the pluton and in correlative CMG dikes beneath the pluton. Excluding the subvertical fabric mapped in the roof zone southwest of Curecanti Needle (Section 5.2.1), CMG contains an average foliation of 272˚, 30˚ N (Fig. 5-3E),

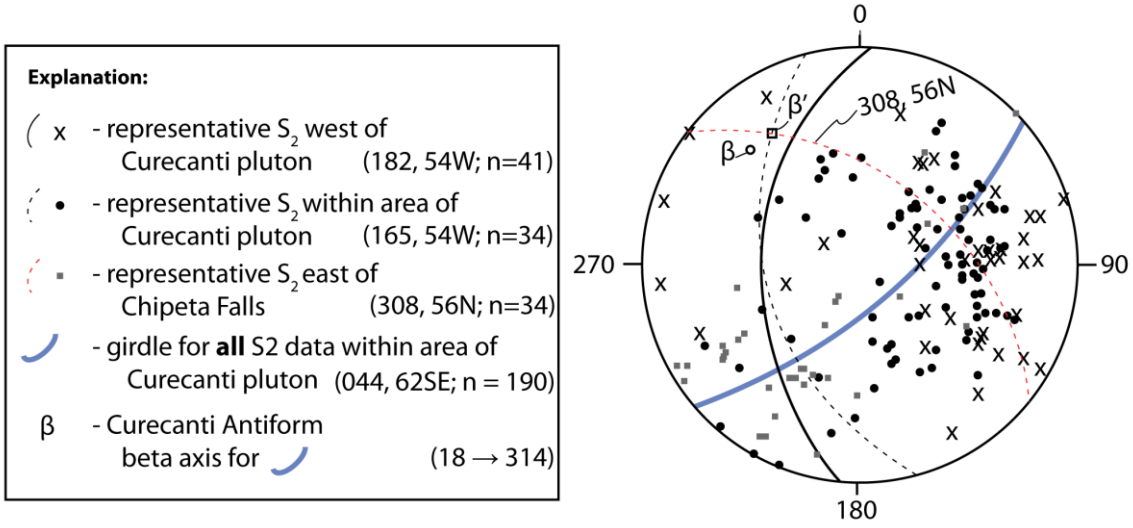

Figure 5-10. Lower-hemisphere equal-area projection of representative poles to planes for S_2 data collected 4 km west of Nelson Gulch to Nelson Gulch (x's), within the area of the Curecanti pluton (black dots), and east of Chipeta Falls (gray squares), average plane for these individual S_2 domains, best-fit girdle for all S_2 data collected in this whole region, and beta axis (open circle β; 18˚→319˚) calculated for the Curecanti antiform using all S_2 data (Holcombe, 2005). For clarity, not all poles plotted for previous three fabric domains, but S_2 girdle calculated from all data (81 additional S_2 measurements included for girdle calculation , so its n = 190). β' (open square) is the beta axis defined by the intersection between the two dashed planes, and is oriented 17˚ → 321˚. There is a 6˚ dihedral angle between β and β'.

which strikes subparallel to the pervasive set of 400 vertical pegmatitic dikes exposed just west of Nelson Gulch (273, 89N, n=41; Fig. 3-1). This average plane includes data from both the floor zone and correlative dikes of CMG, as their fabrics were indistinguishable both in orientation and character. There is a 52˚ dihedral angle between the foliation and pluton floor contacts directly measured in the field (Fig. 5-3C), which is contrary to many observations of margin-parallel foliations within plutons (Vernon et al., 2004).

The mesoscale structures mentioned above are localized in the dikes below the Curecanti pluton main body (Fig. 3-4, inset HBC10-18), the pluton floor zone (Fig. 5-3D), and the pluton roof zone (Fig. 5-1A). The core of the Curecanti pluton does not have a mesoscale foliation and appears as a homogenous, fine-grained, garnet-bearing monzogranite (Fig. 5-2). Fabrics that are limited to pluton margins, the 'onion skin' foliation pattern of Paterson et al. (1998), are usually interpreted as solid-state or magmatic foliations recording principal strain axes that are normal to their margins due to flow of magma in the core of a pluton as its margins are crystallized. This model is particularly apt for plutons emplaced into brittle rocks, providing a differential viscosity that results in margin-parallel "filter pressing" and foliation development (Paterson et al., 1989; Vernon et al., 1989; Miller et al., 2009; Paterson et al., 1998; Paterson et al., 2004; Paterson and Vernon, 1995).

In the Curecanti pluton, a weak foliation is present and localized in the pluton margins, but is oblique to the orientation of the pluton margins (Section 5.2.3). This obliquity, along with the obliquity between the pluton margins and its host rock structure implies a decoupling of CMG melt from its host rocks and/or previously crystallized portions of the pluton (Paterson et al., 1998). This corroborates the suggestion of Paterson et al. (1998) that a pluton fabric should not be used to infer the orientation of the pluton margins in areas where – unlike the Curecanti pluton – pluton geometry is unclear.

CHAPTER 6
RESULTS: MICROSCALE OBSERVATIONS

6.1 Nelson Gulch transect microscale observations

Three samples exemplifying the strain preserved along the NGT are presented: HBC10-5 (garnet-bearing aluminous schist host rock), HBC10-39 (CMG from the Curecanti pluton's roof zone on the east side of Nelson Gulch), and HBC10-25 (CMG from 70 m above the Curecanti pluton floor, in the pluton core). The observations made from these samples are discussed below.

6.1.1 NGT/Curecanti pluton roof microscale observations

Sample HBC10-39 comes from the east side of Nelson Gulch and is representative of the Curecanti pluton roof zone at this location (Fig. 3-3). It is a monzogranite with phenocrysts of plagioclase and quartz. CMG here does not contain garnet. This sample contains plagioclase grains ~2-mm-across that are kinked and fractured, with fractures filled by recrystallized quartz (Fig. 6-1A and 6-1B). Although deformation twins are not continuous across fractures, feldspar is fractured and filled with quartz, suggesting submagmatic flow (Bouchez et al., 1992). Quartz grain boundaries bulge into each other, subgrains are beginning to form within quartz grains, and occur as interfingering sutures (Fig. 6-1C). This is the classic quartz texture of GBM from Stipp et al. (2002), and along with the subgrains forming within quartz, this indicates a transition between SGR and GBM around 500˚C. Flame perthite and abundant microcline twinning are also found in this sample, features which are suggested to form during high-temperature solid-state deformation (Vernon, 2000). These microstructures indicate solid-state flow (Paterson et al., 1989), possibly with melt still present (Vernon, 2000), as indicated by the fractured plagioclase (Bouchez et al., 1992).

Figure 6-1. Photomicrographs of representative samples along the NGT (see Section 7.1.1). (A) CMG (HBC10-39) from the roof zone of the Curecanti pluton showing quartz (qtz) boundaries with interfingering sutures (red arrow) at grain boundaries, quartz-filled fractures (black arrow), and twinned feldspar (fld; upper right feldspar). Sample label box is 500 µm-wide. (B) This sample also has large, kinked feldspar (red arrow) with quartz-filled fractures (white arrow). Sample label box is 500 µm-wide. (D) CMG (HBC10-25) from the core of the Curecanti pluton with abundant subgrains and undulose extinction development (blue arrow), kinked muscovite (ms; red arrow), and core-mantle structure on feldspar grains (yellow arrow). Sample label box is 500 µm-wide. (D) HBC10-5, a garnet (white arrow) sillimanite schist from Nelson Gulch (see insets i. and ii. for photomicrograph locations) with bulging quartz grain boundaries (red arrow). Sample label box is 500 µm-wide.

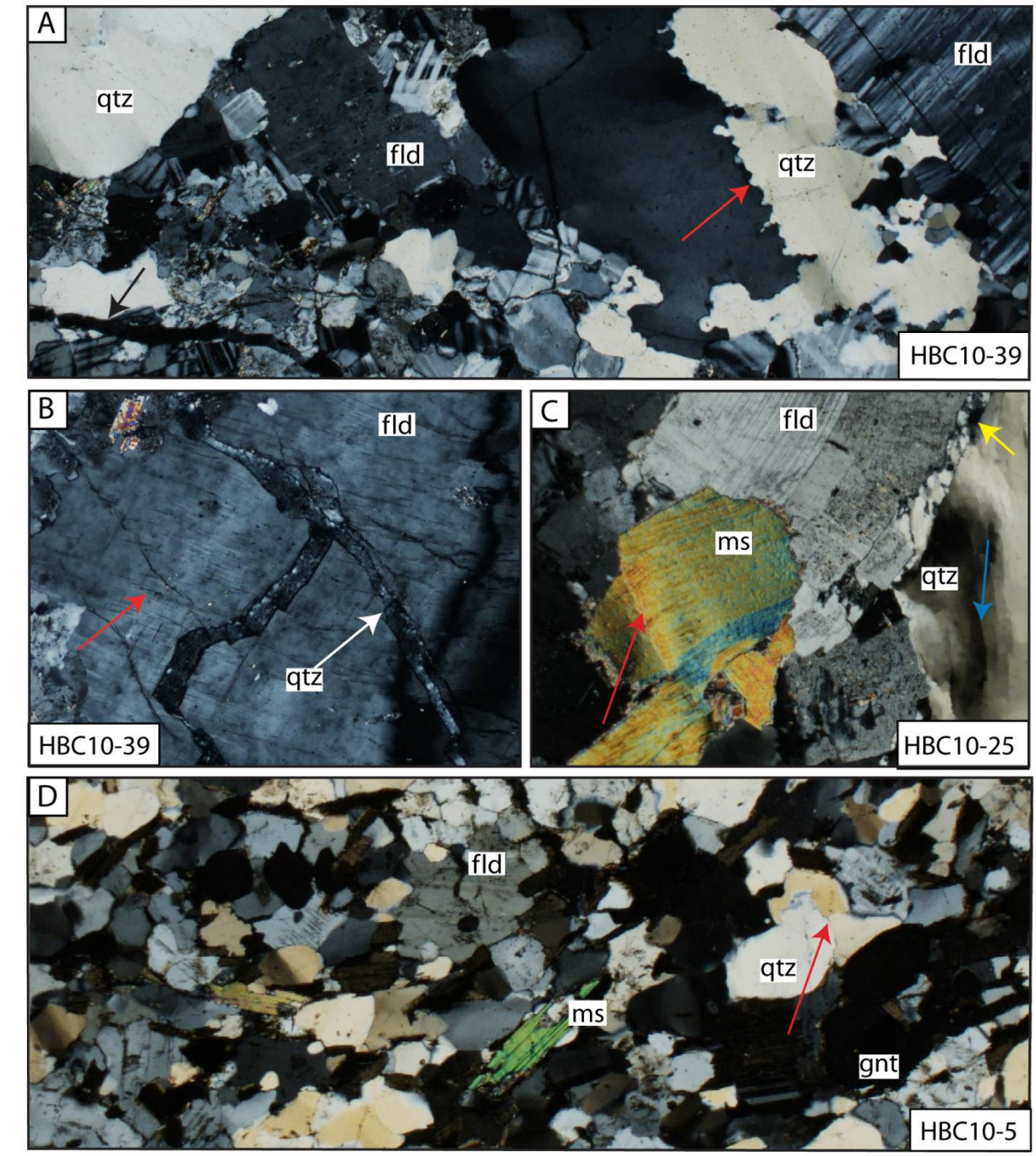
A
qtz
fld
fld
qtz
HBC10-39
B
fld
qtz
HBC10-39
C
fld
ms
qtz
HBC10-25
D
fld
qtz
ms
gnt
HBC10-5
i
C
D
A,B
ii
C
D
A,B

6.1.2 NG/CMG microscale core observations

Though macroscopic fabrics were constrained to 10 m above or below the Curecanti pluton floor and correlative dikes (Section 5.4), there is a relatively large amount of strain accumulated by HBC10-25, a sample from 70 m above the Curecanti pluton's floor (Fig. 6-1C). Muscovite and feldspars are kinked, and recrystallized quartz grains mantle large plagioclase and quartz grains, indicating solid-state deformation (Vernon, 2000). In addition, large (~50-100 μm) quartz crystals contain abundant subgrains and sweeping extinction (Fig. 6-1C) and may record SGR at temperatures between 250 and 500 ˚C (Stipp et al., 2002). All of these are evidence of high-temperature, solid-state strain accumulation in this sample.

6.1.3 NGT/Curecanti pluton host rock microscale observations

As mentioned in Section 5.1.4, a garnet + sillimanite + muscovite schist is exposed on the west side of Nelson Gulch (i.e. HBC10-5). This sample displays strain-free quartz grains that join at 120˚ (Fig. 6-1D). This sample typifies the texture observed in the Curecanti pluton's host rocks along all three transects, and likely records the high temperature history of the gneiss, which were deformed several times (Section 2.2.2) under amphibolite-facies conditions (Jessup et al., 2006).

6.1.4 NG/CMG microscale observations summary

CMG records a significant amount of strain in the Curecanti pluton roof (Fig. 6-1C) and core (Fig. 6-1D) zones, despite the lack of a mesoscopic foliation observed in these samples. High-temperature (>500 ˚C for GBM observed in Fig. 24A) quartz deformation and evidence for submagmatic flow (Fig. 6-1B) suggest subsolidus deformation as the granitoid was crystallizing (Paterson et al., 1989; Vernon, 2000).

6.2 Pioneer Transect microscale observations

As previously mentioned, the PT provides the best exposures of the Curecanti pluton across its entire thickness (Figs. 3-3 and 3-4). Microstructural observations from representative samples along the PT in the Curecanti pluton's roof zone, core, floor zone, CMG dikes, and the host rocks are reported in the following five Sections.

6.2.1 PT/Curecanti pluton roof microscale observations

The highest structural position in the Curecanti pluton (HBC10-34; Section 3.3.3) displays myrmekite, flame perthite, kinked biotite and muscovite, and fractured plagioclase with continuous albite twins across the fractures (Fig. 6-2A and 6-2B). These microstructures suggest submagmatic flow (Bouchez et al., 1992), similar to the roof sample along the NGT (Section 6.1.1).

6.2.2 PT/Curecanti pluton core microscale observations

Located approximately in the middle of the Curecanti pluton (Fig. 3-3), sample HBC10-55 (unfoliated CMG; Fig. 5-2) displays quartz grains with boundaries that bulge into each other and kinked feldspars and plagioclase (Fig. 6-2B), but none of the brittle fracturing pervasive in HBC10-34 (Fig. 6-2A). A few m below HBC10-55 in the Curecanti pluton, sample HBC10-47 (unfoliated CMG) is also from the pluton's core exposed on the west ridge of Curecanti Creek canyon (Fig. 3-3). This sample displays quartz with undulose extinction and subgrain development (Fig. 6-2C), suggesting deformation occurred at temperatures between 400-500 ˚C (Stipp et al., 2002).

6.2.3 PT/Curecanti pluton floor microscale observations

Sample HBC10-32, from the level of the Morrow Point Reservoir (2182 meters above sea level; 20 m above the pluton's floor according to Hansen (1964), is non-foliated CMG and contains quartz with undulose extinction whose boundaries bulge into other quartz, twinned feldspar, and myrmekite (Fig. 6-3A). The actual floor contact of the pluton is exposed at the base of the cliff below Pioneer Lookout Point (Fig. 3-4), and photomicrographs from this contact in sample HBC10-14 reveal an abundance of brittle deformation in CMG up to 10 m away from the pluton's floor contact (Fig. 6-3B). Myrmekite and quartz with bulging grain boundaries are also present in this sample. The floor contact is also exposed on the east side of Blue Creek Canyon, but sample HBC10-53, from the same structural position within the pluton as HBC10-14, does not display

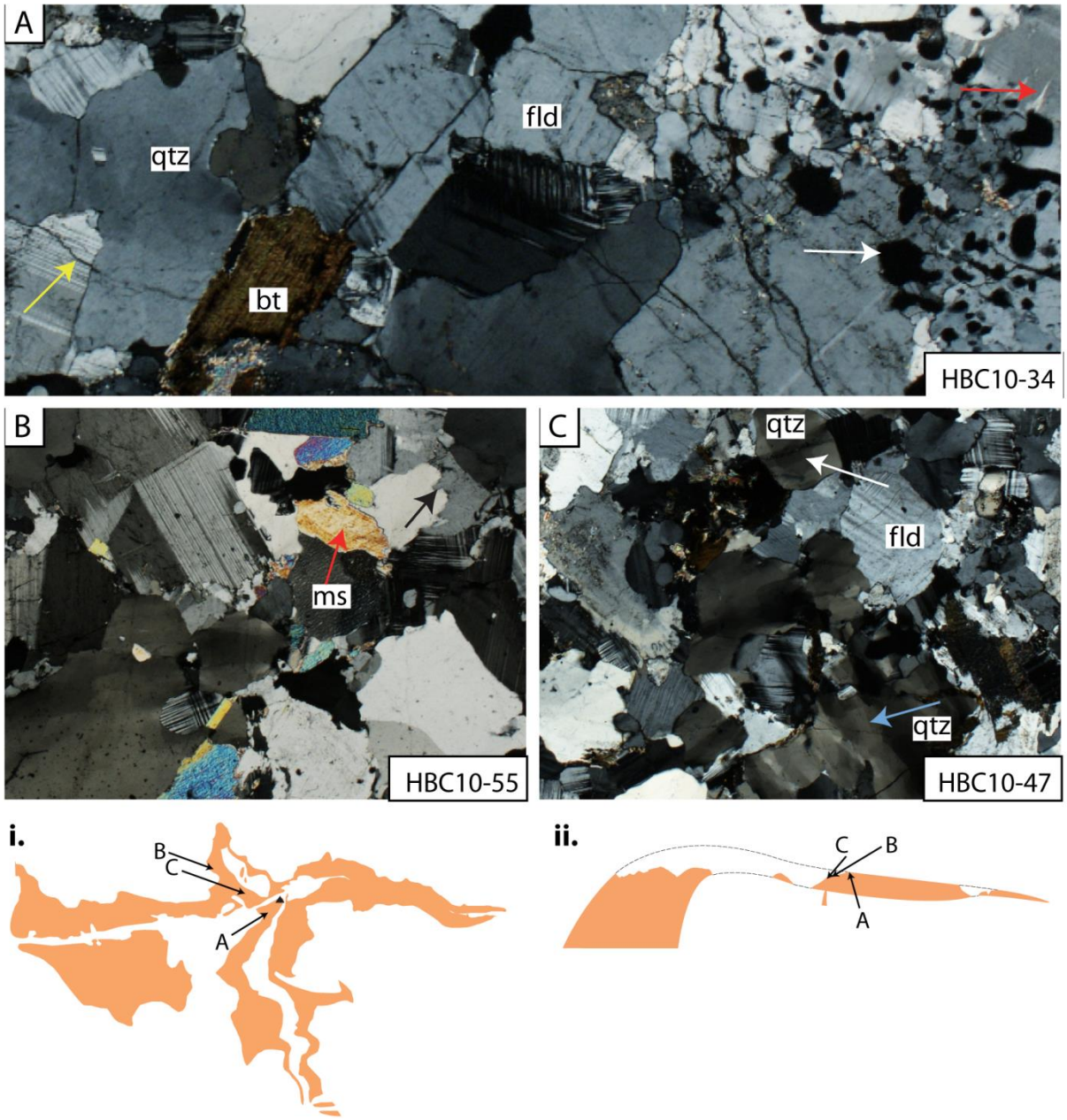

Figure 6-2. Photomicrographs of representative samples of the Curecanti pluton roof zone and core exposed along the PT (Sections 7.2.1 and 7.2.2). (A) Representing the highest structural position in the Curecanti pluton (~10 m-below the pluton's roof contact; see insets i. and ii. for sample location), sample HBC10-34 is CMG that displays fractured plagioclase (yellow arrow); albite twins are continuous across these fractures. Microperthite (red arrow) and myrmekite (white arrow) also present. Sample label box 1000 µm-wide (B) In the core of the pluton, HBC10-55 shows strain-free quartz grain boundaries bulging into one another (black arrow) and kinked muscovite (red arrow). Some quartz has undulose extinction (lower left). Sample label width 500 µm. (C) ~10 m-lower in the Curecanti pluton than B, HBC10-47 shows quartz undulose extinction (white arrow) and sub-grain development (blue arrow). Sample label width 500 µm.

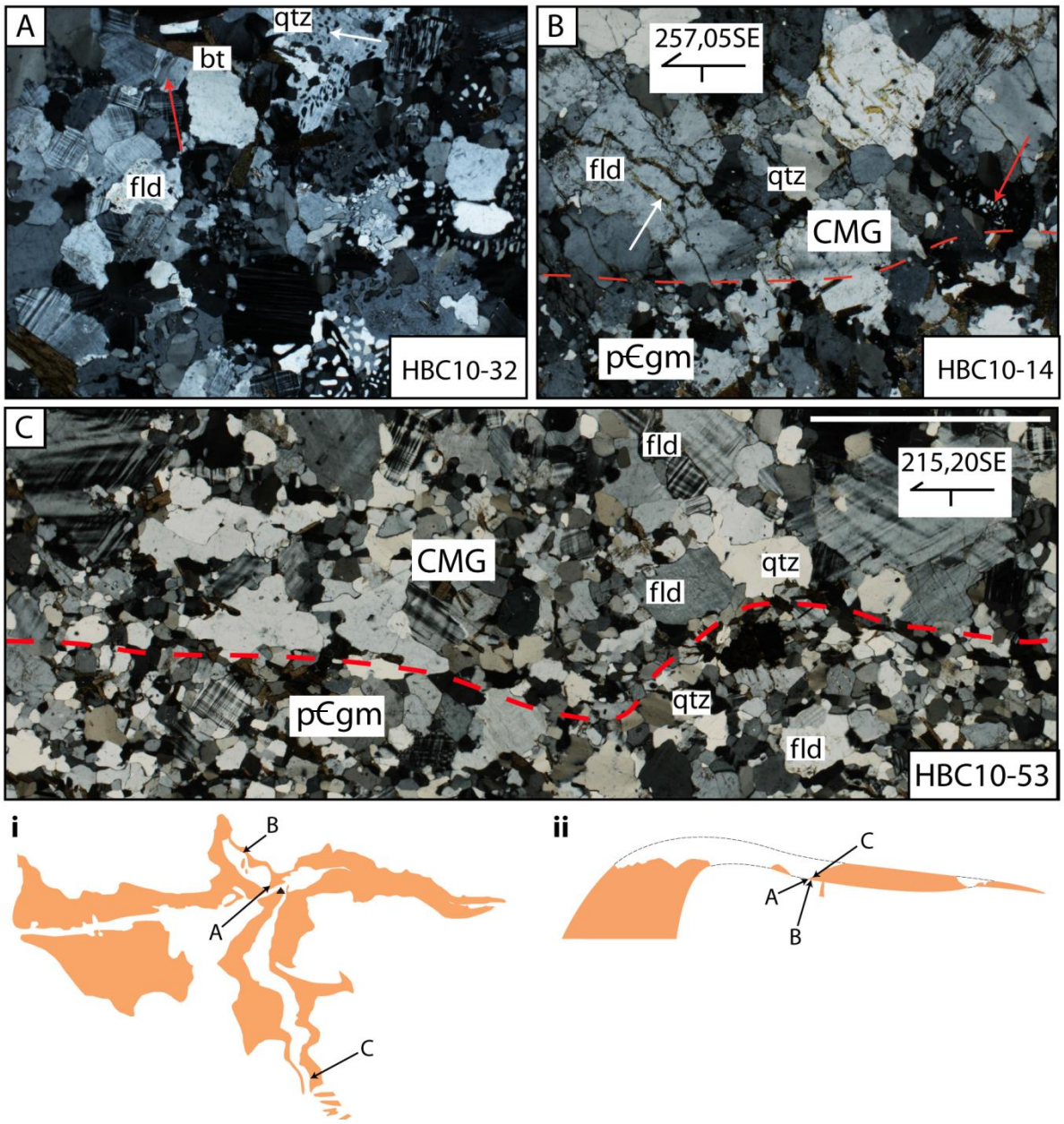

Figure 6-3. Photomicrographs of representative samples of the Curecanti pluton floor zone exposed along the PT (see Sections 7.2.3). (A) Sample HBC10-32 (unfoliated CMG, see insets i. and ii. for locations), ~10 m-above the Curecanti pluton floor contact, displays abundant myrmekite (white arrow) and twins in fledspar (red arrow). Sample label width 500 µm. (B) The floor contact (orientation here: 257˚, 05˚SE) of the Curecanti pluton exposed in Curecanti Creek canyon by sample HBC10-14 (Fig. 9), showing CMG (top two thirds) in contact (red dotted line) with quartzofeldspathic gneiss (lower third), myrmekite (red arrow), and fractured feldspar filled with clays (black arrow). Quartz is relatively strain-free in both CMG and p€gm. Sample label width 500 µm. (C) Floor contact (orientation here: 215˚, 20˚SE) of the Curecanti pluton exposed in Blue Creek Canyon by sample HBC10-53. No myrmekite or fracturing present at the floor contact, and quartz is strain-free in both the CMG (upper two thirds) and p€gm (lower third). White bar is 1000 µm-wide.

the brittle microstructures or myrmekite present in HBC10-14 (Fig. 6-3C). While the latter of these three samples contains a mesoscopic foliation, these samples did not accumulate as much strain as an unfoliated sample of CMG (HBC10-47, Fig. 6-3C) from the pluton core. This implies solid-state (Fig. 6-3A; BLG and myrmekite) and submagmatic flow (Fig. 6-3B; brittle fracturing of feldspars) occurred along some areas of the Curecanti pluton floor but not others (Fig. 6-3C).

6.2.4 PT/CMG dikes microscale observations

CMG dikes below the main pluton in Curecanti Creek Canyon display the most well-developed fabric observed in CMG along any of the three transects. A mm-scale biotite fabric in these dikes is subparallel to a fabric defined by elongate schlieren (Fig. 5-4B). This fabric is cross-cut by mm-scale garnet porphyroblasts (Fig. 6-4A and 6-4B), possible indicating a magamatic fabric developed before growth of the porphyroblasts. Quartz in these dikes contains undulose extinction, but no evidence of highly mobile grain boundaries (Fig. 6-4C and 6-4D), further evidence that fabrics observed in the field (Section 5.2.3) formed as a result of magmatic flow rather than tectonic stresses (Paterson et al., 1989; Vernon, 2000).

6.2.5 PT/Curecanti pluton host rock microscale observations

Sample HBC10-48 is located 10 m above the pluton and is representative of the Curecanti pluton host gneiss and migmatite in the Curecanti Needle area. This sample has quartz that is relatively strain-free, and quartz grain boundaries are simple and commonly join at 120˚ angles (Fig. 6-5). These textures are typical of the high-temperature, amphibolite-facies host rocks to the Curecanti pluton, and the host rock fabric foliation is constant near the Curecanti pluton, other than the apparent replacement of some host migmatite leuocosome by CMG near the floor along the PT (Section 5.2.3). CMG veins that inject subparallel to host rock leucosome are only observed on a cm-scale (Fig, 5-3E).

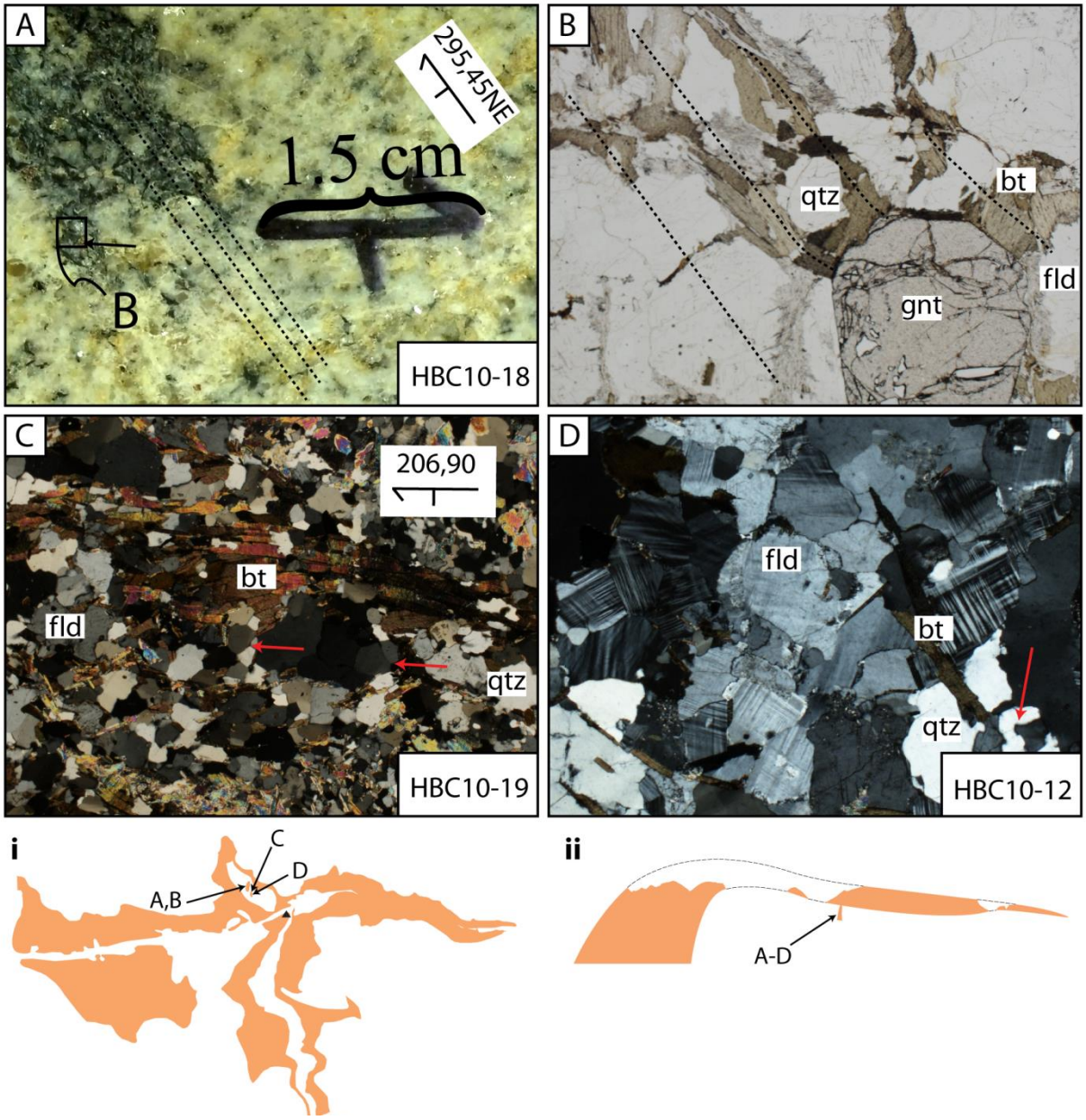

Figure 6-4. Photomicrographs of representative samples of CMG exposed in dikes beneath the Curecanti pluton exposed along the PT (Sections 7.2.4). (A) Mesoscale reference photo of sample HBC10-18 (see insets i. and ii. for sample location) showing CMG with a cm-scale biotite aggregate (orientation here: 295˚, 45˚NE); location of B shown as black box. (B) Plane light photomicrograph of sample HBC10-18 showing 3 mm-wide garnet porphyroblast cross-cutting the biotite aggregate foliation (dotted black lines); same orientation as A. (C) Photomicrograph of sample HBC10-19 from a different, but similar foliated (orientation here: 206˚, 90˚) CMG dike exposed 20 m-southeast of sample HBC10-18; 120˚ strain-free quartz grain boundaries shown with red arrows. Sample label box is 1000 µm-wide. (D) Photomicrograph from sample HBC10-12 showing bulging grain boundaries (red arrow) in quartz which is relatively strain free. Same orientation as C. Sample label box is 500 µm-wide.

6.3 Chipeta transect microscale observations

Chipeta Falls provides another transect through the Curecanti pluton (Fig. 3-3). As previously mentioned (Section 5.3.4), the Curecanti pluton thickness has significantly tapered relative to its thickness along the PT (Fig. 3-1), and the foliation within the host rock begins to transition from southwest-dipping to northeast- and southeast-dipping (Fig. 5-10). The strain recorded within the Curecanti pluton roof zone and core, exposed along the CT, is discussed in the following two sections.

6.3.1 CT/Curecanti pluton roof microscale observations

Sample HBC10-49, from 1 meter below the roof contact of the Curecanti pluton near Chipeta Falls (Fig. 3-3), contains myrmekite, feldspar twins, fractured plagioclase

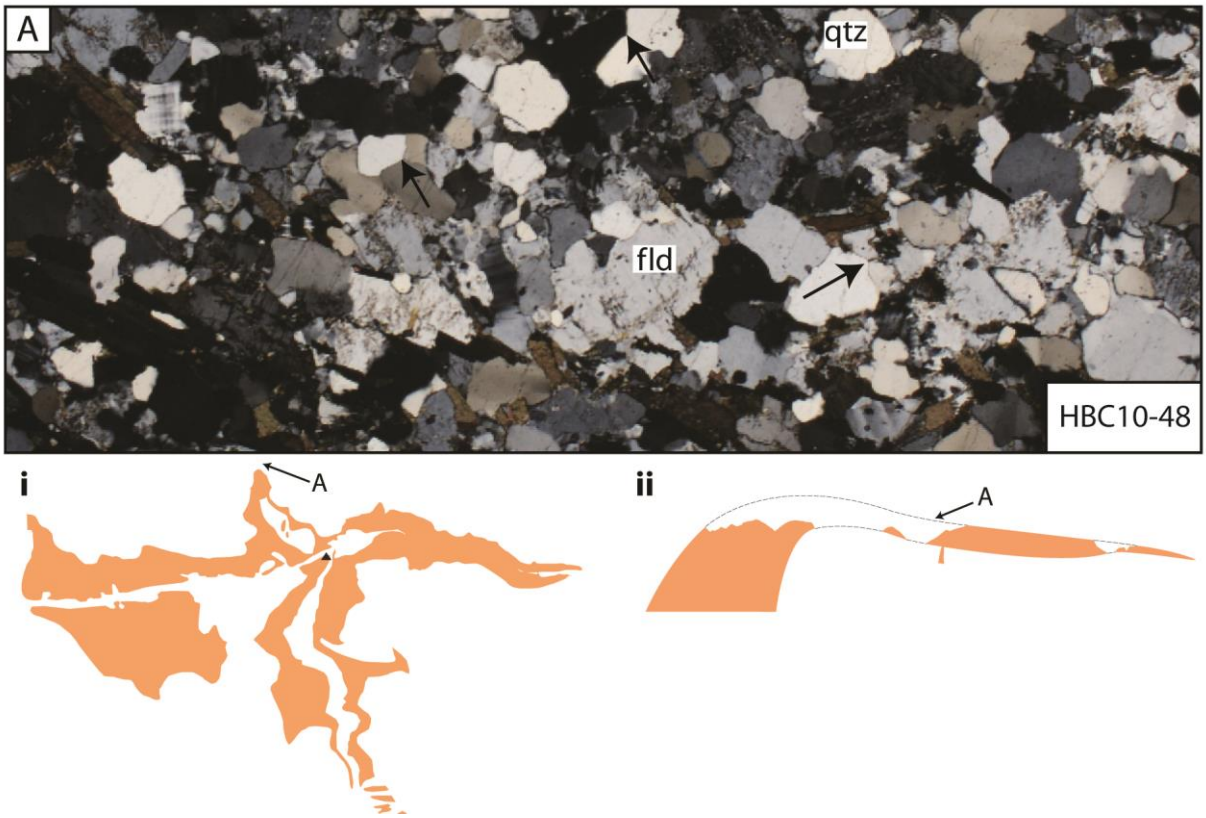

Figure 6-5. Photomicrograph of representative sample (HBC10-48) of Curecanti pluton host gneiss exposed 10 m above the pluton roof in Curecanti Creek Canyon (see insets i. and ii. for sample location). Notice relatively strain-free quartz with 120˚ grain boundaries (black arrows). This texture is common for both roof and floor gneiss/migmatite in the Curecanti Needle area, regardless of their distance away from pluton. Sample label box is 500 µm-wide.

and quartz in filled with fine-grained quartz, kinked muscovite, and undulose extinction in quartz (Fig. 6-6A). These observations are similar to microscopic observations made at the Curecanti pluton roof exposed along the NGT (Section 6.1.1) and the PT (Section 6.2.1) of brittle fracturing of plagioclase in filled by quartz, along with bulging grain boundaries and myrmekite, all of which are criteria for submagmatic flow (Paterson et al., 1989; Vernon, 2000).

6.3.2 CT/Curecanti pluton core microscale observations

Sample HBC10-38, collected from the Morrow Point Reservoir level of 2182 m, is within 20 m of the Curecanti pluton floor contact, though it is presently beneath the reservoir (Section 3.3.4). While plagioclase is still subhedral, quartz from this sample has interfingering sutured grain boundaries with undulose extinction (Fig. 6-6B), implying solid-state deformation occurring at temperatures >500˚ C (Stipp et al., 2002).

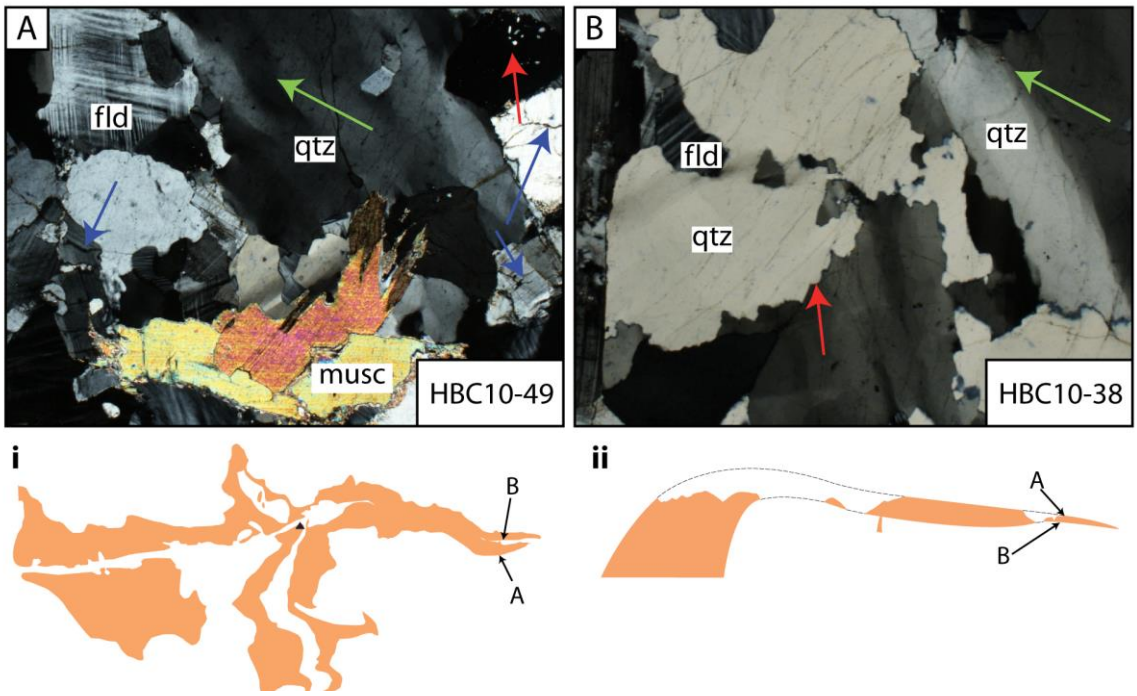

Figure 6-6. Photomicrographs of CMG in the Curecanti pluton exposed along the CT (see insets i. and ii. for sample locations). (A) Sample HBC10-49, from the Curecanti pluton roof zone displays undulose extinction in quartz (green arrow), brittle fracturing of plagioclase (blue arrows), and myrmekite (red arrow). Sample label box is 500 µm-wide. (B) Sample HBC10-38, from the Curecanti pluton core, displaying interfingering sutured quartz grain boundaries (red arrow) and undulose extinction in quartz (green arrow). Sample label box is 500 µm-wide.

6.3.3 CT/Curecanti pluton floor microscale observations

The floor contact of the Curecanti pluton is subhorizontal along this transect, as mapped by Hansen (1971), and is discordant with respect to the host rock macroscopic foliation, but is presently 20 m below the level of the Morrow Point Reservoir.

6.3.4 CT/Curecanti pluton host rock microscale observations

No microscopic observations are reported for the Curecanti pluton host rock along the CT because the textures observed in HBC10-5 (Fig. 6-1D) and HBC10-48 (Fig. 6-5) accurately and fully represent microscale observations made along this transect.

6.4 Summary of microscale observations

It had been previously recognized that the Curecanti pluton and its correlative dikes contained a weak fabric (Hansen, 1964), but the nature and distribution of this fabric was previously unclear. The observations (Sections 6-7.3) suggest that, while the mesoscale fabric within CMG is limited to the roof and floor zones of the Curecanti pluton and the correlative dikes beneath the Curecanti pluton, there is significant strain accumulation up to 70 meters above the pluton floor contact (e.g. HBC10-25 in Fig. 6-2D). Samples from structurally similar positions as HBC10-25, such as HBC10-55 and HBC10-47 (Figs. 6-2B and 6-3C, respectively), do not preserve as much strain. This is not surprising, seeing as one of the problems with interpreting granitoid fabrics is that they were emplaced over a very short time period, as short as 6 months for a Curecanti-sized pluton, according to granitoid-emplacement rate calculations made by Petford et al. (1993). Pavlis (1996) also noted that if a pluton is weaker than its host rocks, the pluton would accumulate most of the strain associated with its emplacement, such that lack of deformation development in the pluton host rocks synchronous with pluton emplacement (i.e. a strain aureole) is not conclusive of non-tectonic emplacement. However, when a pluton is weaker than its host rocks, it should in fact record the last increment of strain as it crystallizes and becomes rigid (Pavlis, 1996).

Some evidence of submagmatic flow was observed in CMG, primarily in the roof zone (e.g. HBC10-39 and HBC10-34). However, even when a fabric was mapped in the field, samples were shown to display a significant amount of internal deformation in

quartz, suggesting that solid-state flow was the dominant mechanisms of fabric formation in the Curecanti pluton. A summary of the meso- and microscopic observations made for CMG and its host rocks along these three transects is presented in Table 6-1, which suggests that submagmatic flow was the most dominant deformation mechanism in the pluton roof, solid-state flow is responsible for the textures observed in the pluton core, and magmatic flow with minor solid-state flow may explain the textures observed in the pluton floor zone and the dikes observed beneath the pluton. CMG dikes observed beneath the pluton contain a foliation, but garnet porphyroblasts grow over this foliation, implying foliation formation prior to crystallization of the melt. Strain is distributed heterogeneously along the Curecanti pluton floor zone, however (e.g. Fig. 6-3A-C), so the differences between strain observed in CMG dikes below the pluton and strain observed in the floor zone of the pluton do not preclude them from being from the same parent magma and/or coevally emplaced.

Pavlis (1996) suggested this pattern of observations to indicate emplacement in a locally strike-slip or extensional setting, which allows for "normal" geothermal gradients, cooling of a pluton roof before its floor, and partitioning of strain into the floor zone. In addition, horizontal sills whose lengths are far greater than their thicknesses may be an igneous feature ubiquitous with extensional tectonic terranes (de Voogd et al., 1986). Alternatively, if a pluton is emplaced in an area with inverted isotherms, highest temperature fabrics would be recorded in the floor, with progressively lower temperature fabrics being recorded closer to the pluton roof zone.

Table 6-1: Summary of meso- and microscopic observations

Transect name	**NGT**		**PT**		**CT**	
	Meso	**micro**	**Meso**	**micro**	**Meso**	**micro**
Roof host	*Qtzfld. gneiss* *Garnet schist*	*n/a*	*Qtzfld. gneiss* *Opthal mig.* *Ptygmatic mig.*	*Strain free*	*Qtzfld. gneiss* *Nebulitic mig.* *Agmatic mig.*	*n/a*
Roof zone	Wedged xen. Unfol.	Submag. SGR	Wedged xen. Stoping Unfol.	Submag.	No xen.	Submag. Undulose
Core	No xen.	GBM	Unfol.	BLG/SGR	Unfol. CMG	GBM Undulose
Floor zone	No xen.		Wedged xen. Foliated	BLG	n/a	n/a
Subpluton dikes	n/a	n/a	Foliated	Undulose	n/a	n/a
Floor host	*Qtzfld gneiss*	*n/a*	*n/a*	*n/a*	*n/a*	*n/a*

Table 6-1: Summary of mesoscopic (meso column) and microscopic (micro column) observations along the three transects introduced in Section 4.2. Salient observation for the roof and floor host rocks (italicized), Curecanti pluton roof zone/core/floor zone, CMG dikes beneath the pluton (subpluton dikes), given for each transect. Abbreviations: qtzfld. (quartzofeldspathic), xen. (xenoliths), submag. (submagmatic foliation), unfol. (unfoliated), mig. (migmatite),

CHAPTER 7
RESULTS: MAGMA DRIVING PRESSURE

7.1 Magma driving pressure and crustal magma traps

The level at which an ascending magma is arrested depends in part on its magma driving pressure (P_d) and the location of crustal anisotropies (e.g. the brittle ductile transition; Hogan and Gilbert, 1995). As shown by Hogan and Gilbert (1995), an ascending magma may be arrested even when its P_d value is higher than lithostatic overburden (Sv). In the following five Sections, P_d is evaluated for CMG from its source depth to the surface during both wholesale-tension and lithostatic states of stress. These Pd data use the diking model of Clemens and Mawer (1992), and assume that CMG was emplacement relatively quickly in a single increment. If the Curecanti pluton was emplaced incrementally through the assembly of many sheets (e.g. Miller et al., 2011), P_d would likely be reduced greatly by P_{vis}. However, Hogan and Gilbert (1995) argue that low phenocryst content, as observed in the Curecanti pluton, may imply a single increment of emplacement in which the magma remained mostly liquid. In addition, the lack of evidence for internal zonation within the Curecanti pluton suggests relatively rapid emplacement in a single event rather than incremental assembly.

7.2 Curecanti pluton hydrostatic pressure $(P_h)_C$

The differential hydrostatic pressure represented by (2) is caused by the density difference between the pluton and the host rock. A compilation of thermochronologic data by Shaw et al. (2005) showed that the Black Canyon of the Gunnison region gneisses were >500˚C at 1.4 Ga, and Jessup et al. (2006) determined the area had cooled through $^{40}Ar/^{39}Ar$ muscovite closure-temperature at 1356 Ma, so average crustal densities may be considered reasonable estimates for the region. A density of 2,950 kg meter^{-3} was used for the lower crust, and 2,750 kg meter^{-3} for the upper crust. The density of 2310 kg meter^{-3} for the Curecanti pluton was derived from (sample HBC10-39) geochemical data (Chapter 8) at a pressure of 3 ± 1 kilobars (Section 2.2.3) using the software *KWare Magma* of Wohletz (2009). Discussion in Section 7.6 will show that minor density variations are insignificant for the calculation of Curecanti pluton P_d, due to uncertainties

at least one order of magnitude larger in the other components of the P_d calculation. Of greater importance is the depth to the source magma chamber, over which some remote control is afforded by geophysical data interpreted by McCoy and Roy (2005) and Isaacson and Smithson (1976). A granitic batholith was interpreted to be approximately 12 km-below the surface in the Sawatch Range and the Elk Mountains (Tweto and Case, 1972; Isaacson and Smithson, 1976), which was suggested by Shaw et al. (2005) to represent a relic of a mid-crustal magma layer formed at 1.4 Ga as plutons pooled at the rheological boundary that is the brittle-ductile transition (Fig. 7-1), though McCoy and Roy (2005) warned that age constraints on this gravity anomaly are not readily available. Without further data suggesting otherwise, however, the thermal model of the Mesoproterozoic crust from Shaw et al. (2005; Fig. 7-1), along with the geophysical interpretations of McCoy and Roy (2005), is used to infer a present-day depth of ~12 km to the top of this gravity anomaly near the Black Canyon of the Gunnison. Using the previously established estimate of 3 ± 1 kbar for the emplacement of the Vernal Mesa pluton (Jessup et al., 2006), and possibly also the Curecanti pluton (Section 2.2.3), we suggest this gravity anomaly to have been ~18-22 km deep at 1.4 Ga. The resultant differential hydrostatic pressure would theoretically reach a maximum value of 174 MPa at the Earth's surface, but clearly the other components of P_d, along with the presence of crustal anisotropies, and the opening plane orientation for magma transport will all have some bearing over whether this pressure is ever obtained by ascending CMG.

7.3 Magma chamber overpressure (P_o)

Reches and Fink (1988) evaluated P_o by quantifying P_h, P_{vis}, and S_h, then calculated the amount of P_o required for a dike of known dimensions, emanating from a source at a known depth, to reach a known emplacement depth. However, at the lithostatic pressure previously suggested for the emplacement of the Curecanti pluton (3 ± 1 kbar), this volume increase would be small, on the order of 10's or less MPa increase (Burnham, 1979). In addition, a set of pegmatite dikes that directly cross cut the pluton might indicate an overpressure in the magma chamber which fed the Curecanti pluton (Jahns and Burnham, 1969). The east-west striking, vertically dipping dike swarm located just west of Nelson Gulch (Fig. 3-1) is thought to be younger than the Curecanti pluton

Figure 7-1. Schematic block diagram of the lithosphere beneath southern Colorado (present day north shown) at 1.4 Ga. Interpreted and reconstructed relationships show contrasting structural and magmatic styles due to different present-day exposure levels of this crustal section. Shallower exposure levels are characterized by subvertical northeast-striking fabrics, and deformation partitioned along discrete shear zones intruded by plutons (e.g. BCSZ and Vernal Mesa/Curecanti plutons, exposed by A'-A"). NW dikes near the Vernal Mesa pluton and EW dike swarm near the Curecanti pluton, shown as grey lines on the top of the block, that are both interpreted to fill tension gashes and record different principal stress orientations. Cross section A'-A" is not interpreted to represent significantly different structural positions of rocks along its trace. The same granitoid batholith interpreted below the Colorado mineral belt/Black Canyon region may be exposed in the southern Wey Mountains of Colorado. These deeper levels of exposure are characterized to moderately- to shallowly-dipping foliations and interconnected networks of penetratively deformed sills and plutons. Modified from Jones et al. (2010). Approximate paleodepths shown on left side of block.

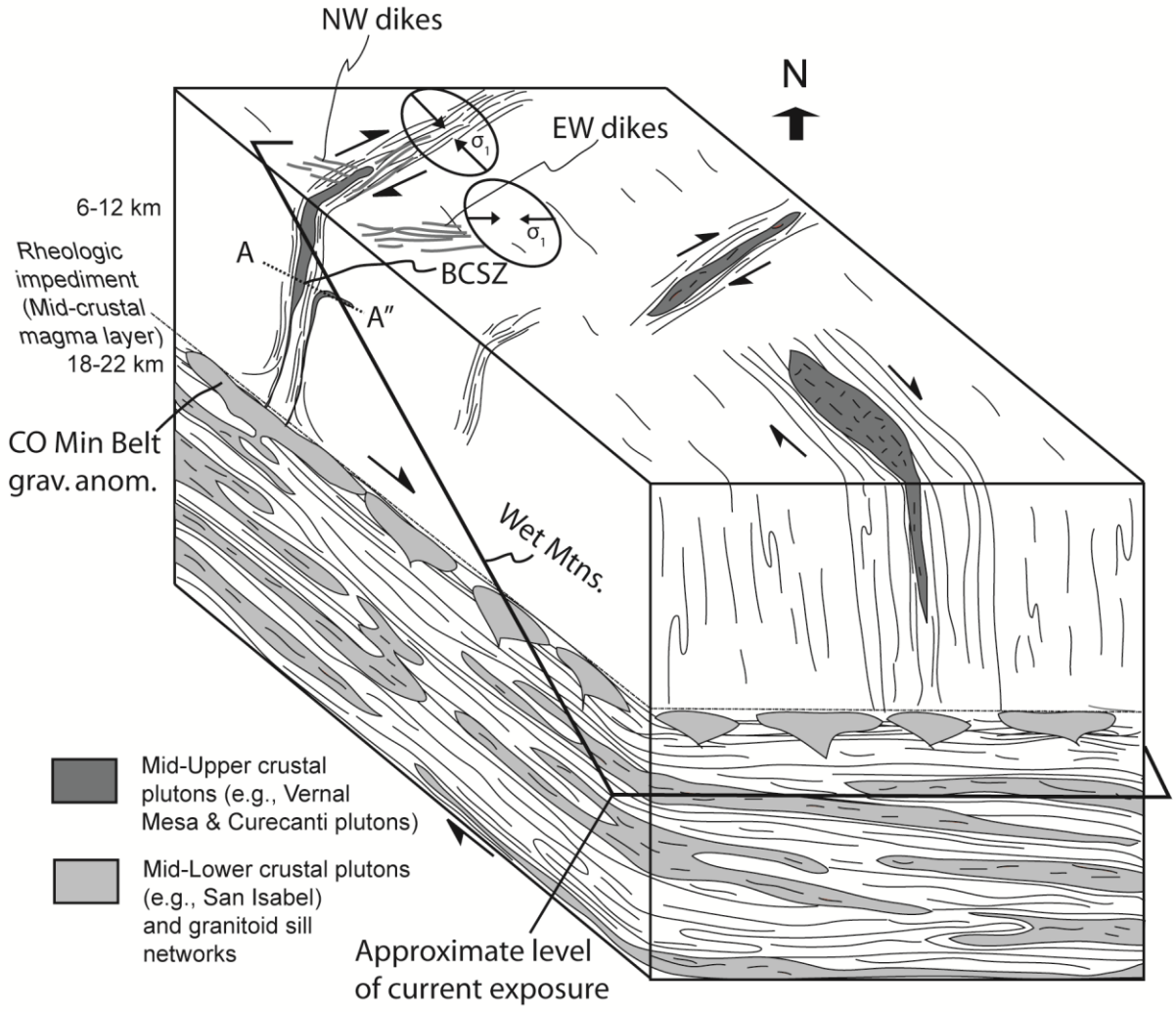
NW dikes
N
EW dikes
σ_1
σ_1
6-12 km
Rheologic
impediment
(Mid-crustal
magma layer)
18-22 km
A
BCSZ
A″
CO Min Belt
grav. anom.
Wet Mtns.
Mid-Upper crustal
plutons (e.g., Vernal
Mesa & Curecanti plutons)
Mid-Lower crustal plutons
(e.g., San Isabel)
and granitoid sill
networks
Approximate level
of current exposure

due to a few similar dikes which do cross cut the pluton. Since almost all of these dikes are located just west of, rather than cross cutting, the pluton, they are thought to represent a switch in the instantaneous stress field just after emplacement of the pluton. As such, we have taken Po to be zero, similar to the work of Hogan and Gilbert (1995).

7.4 Viscous pressure drop (P_{vis})

Baer and Reches (1991) used a value of 0.75 MPa km^{-1} for their granitoid magma, but this was suggested to be an extreme value by Hogan and Gilbert (1995) due to the presence of fluorine in the aforementioned granitoid. The presence of fluorine in the Curecanti pluton (0.03 wt% in HBC10-55; Chapter 10) may also suggest a low value for P_{vis}. A value of 0.5 is adopted here, after the work of Hogan et al. (1998), due to the relatively similar composition of the granitoid rocks in question and the low effect which Pvis has on P_d (Baer and Reches, 1991).

7.5 Horizontal stress (S_h)

Because there are no reliable indicators of paleostress in the Curecanti Needle region at the time of Curecanti pluton emplacement, the state of stress is unknown. However, two end-member crustal stress states are examined to show how these three aforementioned criteria relate to one another and controlled the emplacement depth and shape of the Curecanti pluton. Crustal strength profiles are not available for the southwestern United States during the Mesoproterozoic, so the strength profile of Lynch and Morgan (1987) is used to demonstrate the effect of S_h on P_d during both crustal extension and lithostatic stress states. This crustal strength profile has a maximum value at ~8 km.

7.6 Magma driving pressure conclusions

Using the values discussed in the previous four Sections, Fig. 7-2 shows the lithostatic stress, differential hydrostatic stress, and two driving pressures calculated for sample HBC10-39. P_m represents a driving pressure for a crust experiencing only lithostatic stresses (Section 4.3.4). For the Curecanti pluton, P_m does not become positive until 4 km depth (Fig. 7-2). For this stress regime, emplacement of CMG would be ca. 4

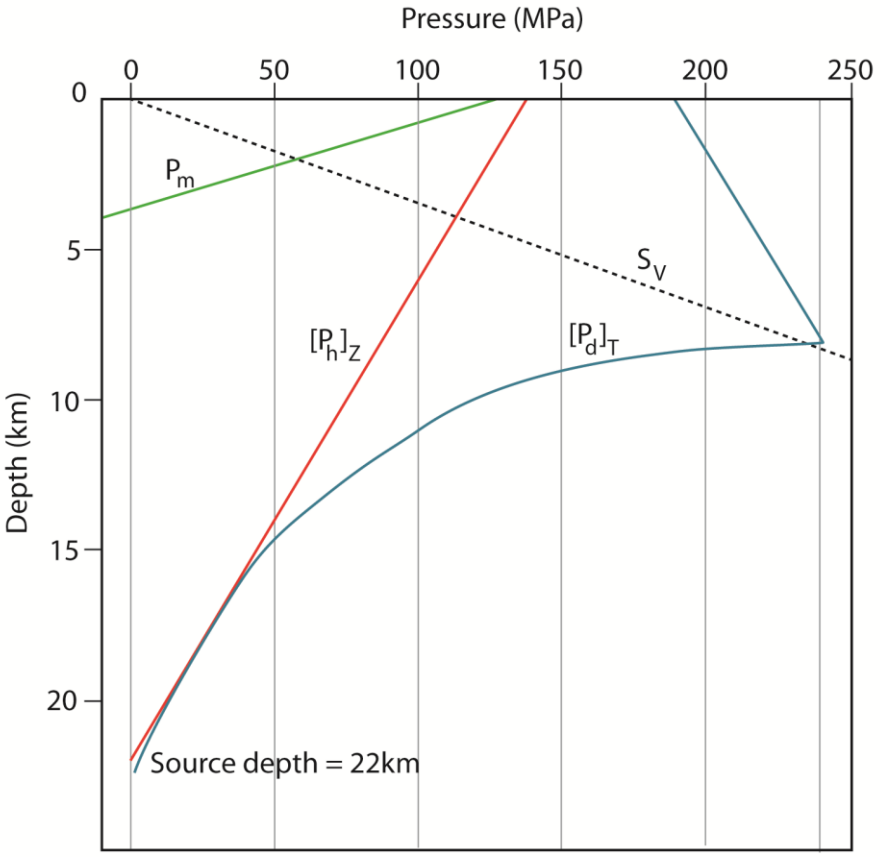

Figure 7-2. Magma driving pressure at various depths calculated from sample HBC10-39 for two crustal stress-states with a source depth of ~22 km. Lithostatic overburden (S_v; dotted black line) and strength curve (not shown) used to calculate driving pressure for the Curecanti pluton emplaced in a crust at its tensile strength ($[P_d]T$, blue line) from Hogan et al. (1998). Driving pressure for a crust at lithostatic pressure (P_m, green line) does not become positive until 4 km depth and reaches a maximum driving pressure of 125 MPa at the Earth's surface. Differential hydrostatic pressure ($[P_h]z$, red line) is the same for both crustal stress end-members and is shown for reference.

km below the Earth's surface, as the liquid reached neutral buoyancy. Any additional compressive stresses would serve to bring this neutral buoyancy depth deeper in the crust. For a crust at its tensile stress, as in the SOA (Hogan and Gilbert, 1995; Hogan et al., 1998), P_d reaches its maximum value around 8 km-deep, the same depth which has the strongest rocks (i.e. highest yield strength). Using a geobaric gradient of 3.7 km = 100 MPa, this max $[P_d]_T$ falls outside the lower range of the previously suggested emplacement depth for the Curecanti pluton by 0.4 km. $[P_d]_T$ maintains a positive value of about 170 MPa at the Earth's surface, implying potential to erupt as a volcano under this stress regime in the absence of a horizontal anisotropy (Hogan and Gilbert, 1995) or a switch in the opening plane orientation (Vigneresse et al., 1999). Furthermore, if a horizontal anisotropy was encountered at a depth where $P_d > S_v$, CMG could have been emplaced as a laccolith which lifted its roof (Hogan et al., 1998). However, a horizontal anisotropy might not be required to form a horizontal sheet, as the magma driving pressure may be enough to switch the opening plane orientation from vertical to horizontal (Chapter 9).

These two end-member stress regimes demonstrate that the density contrast between CMG magma and its wall rocks is sufficient to drive the magma up through the crust if the dike that feeds the pluton maintains connectivity with its source region. Success of this model is also dependent on the pluton remaining completely liquid during ascent. Neutral buoyancy (i.e. P_m) may not be enough to form a horizontal dike such as the Curecanti pluton during extension, because its high driving pressure at the Earth's surface would require a subhorizontal anisotropy to arrest the magma in order for it to crystalize as a pluton (Fig. 7-2).

7.7 Modification of local stress field by magma intrusion.

A non-negligible stress acts perpendicular to a magma-filled dike wall during ascent which effects the principal stresses in the area near intrusion (Parsons and Thompson, 1991; Vigneresse et al., 1999; Ablay et al., 2008). For extending crust, with a vertical σ_1, the Curecanti pluton P_d reached a maximum of 240 MPa at 8 km depth, overcoming lithostatic overburden by ~ 20 MPa (Fig. 7-2). This driving pressure may

have reduced σ_3 by enough to change the opening plane (i.e. the σ_1-σ_2 plane) from vertical to horizontal (Vigneresse et al., 1999). This is discussed further in Chapter 9.

Alternatively, if a crustal heterogeneity (e.g. the brittle ductile transition) was encountered by the ascending CMG, local stress rotation may occur due to more magma flowing to the base of this anisotropy (Menand, 2011). If the anisotropy is rigid enough to impede the magma's ascent and stress begins to rotate due to incoming magma, the local opening plane may change from being vertical (y-z plane for lithostatic stress) to horizontal, and a sill may form (Vigneresse et al., 1999). This will be further discussed in Chapter 9.

CHAPTER 8
RESULTS: WHOLE-ROCK GEOCHEMISTRY

8.1 Major element chemistry & normative minerals

Ten elements (Si, Ti, Al, Fe, Mn, Mg, Ca, Na, K, and P) are typically considered the major elements in geology (Rollinson, 1993). Abundances of these elements are reported as weight percent oxides. The results of whole-rock geochemical analysis of the three samples (discussed in Section 4.4.3) are presented in Table 8-1. Analysis revealed small variations in major element abundances; the average SiO_2 in CMG is 74.79 wt % with a standard deviation of only 0.44 wt %. Likewise, the standard deviations of all other major element oxides (TiO_2, MnO, MgO, CaO, Na_2O, and K_2O) for CMG are all less than 1.00 wt % (Table 8-1).

CIPW norms (Hyndman, 1985) were calculated using the Excel spreadsheet of Hollocher (2003; Table 8-2). Corundum is present as a normative mineral in all three samples (Table 8-2), indicating peraluminous chemistry (Rollinson, 1993). Using the normative minerals for the three aforementioned samples, along with data from Hansen (1964), CMG is plotted on the standard QAP diagram of Streckeisen (1974). Note that Hansen (1964, 1965, 1971, 1987) called the CMG a quartz monzonite, though the data show all samples having enough quartz to fall in the monzogranite field (Fig. 8-1).

8.2 Comparison with global 1.4 Ga granites

The Curecanti pluton and correlative dikes fit into the peraluminous granitoid province of Anderson and Morrison (2005), which lies almost entirely within Colorado and Wyoming (Fig. 8-2). They have relatively high amounts of Y and Nb, which are contained in approximately equal proportions, a trait typical of "within-plate" granites (Fig. 8-2A; Anderson and Cullers, 1999). Most 1.7 Ga plutons plot in the volcanic arc granitoid (VAG) field of Pearce et al. (1984), whereas 1.4 Ga plutons plot in the within-plate granitoid field (WPG; Fig 8-2A). Note that the Oak Creek pluton would plot in the ocean ridge granitoid (ORG) field of Pearce et al. (1984), but was omitted in

Table 8-1. Geochemical data for CMG samples.

Sample ID:		**HBC10-39**	**HBC10-55**	**HBC10-18**
Element	Location in pluton:	Roof zone of pluton	Core of pluton	"Lower three"
Analysis type				
FUS-ICP	*Detection limit*			
SiO_2	0.01%	74.34	74.81	75.22
Al_2O_3	0.01%	12.99	13.59	13.25
Fe_2O_3 (total)	0.01%	1.42	0.93	1.19
MnO	0.0010%	0.021	0.14	0.065
MgO	0.01%	0.18	0.03	0.1
CaO	0.01%	0.9	0.67	0.81
Na_2O	0.01%	3.11	4.2	3.78
K2O	0.01%	5.06	3.72	4.88
TiO_2	0.0010%	0.171	0.017	0.061
P_2O_5	0.01%	0.005	0.02	0.03
LOI		0.25	0.31	0.02
	Totals	98.49	98.44	99.4
Ba	1 ppm	1337	2	207
Be	1 ppm	2	6	5
Sr	2 ppm	175	5	56
V	5 ppm	14	6	7
Y	1 ppm	14	40	55
INAA				
Au	1 ppb	<0.1	<0.1	<0.1
As	1 ppm	< 1	3	< 1
Br	0.5 ppm	< 0.5	< 0.5	< 0.5
Cr	0.5 ppm	< 0.5	< 0.5	1
Hg	1 ppm	< 1	< 1	< 1
Ir	1 ppb	< 1	< 1	< 1
Sb	0.1 ppm	< 0.1	< 0.1	0.2
Sc	0.01 ppm	1.76	13.2	4.64
Se	0.5 ppm	< 0.5	< 0.5	< 0.5
FUS-MS				
Bi	0.1 ppm	< 0.1	0.8	0.6
Cs	0.1 ppm	6.6	10.5	9.5
Ga	1 ppm	16	24	18
Ge	0.5 ppm	1.9	3.9	2.8
Hf	0.1 ppm	4.2	2	2.1
In	0.1 ppm	< 0.1	< 0.1	< 0.1
Rb	2 ppm	120	249	218
Sn	1 ppm	< 1	15	6

Table 8-1. Geochemical data for CMG samples (continued).

Element	*Detection limit*	*(Sample ID)* ***HBC10-39***	***HBC10-55***	***HBC10-18***
Ta	0.1 ppm	10.6	34.4	12.4
Th	0.05 ppm	9.12	6.94	19.2
U	0.05 ppm	1.4	1.73	7.97
Zr	1 ppm	23	33	93
La	0.05 ppm	31.6	7.72	16.8
Ce	0.1 ppm	65.2	19.1	38
Pr	0.02 ppm	6.68	2.35	4.61
Nd	0.05 ppm	23.5	8.66	18
Sm	0.01 ppm	4.07	3.48	5.36
Eu	0.005 ppm	8.22	0.042	0.403
Gd	0.02 ppm	2.72	3.32	6.01
Tb	0.01 ppm	0.41	0.85	1.3
Dy	0.02 ppm	2.52	6.1	8.86
Ho	0.01 ppm	0.49	1.32	1.91
Er	0.01 ppm	1.47	4.37	5.36
Tl	0.05 ppm	0.76	1.52	1.54
Tm	0.005 ppm	0.253	0.931	0.961
Yb	0.01 ppm	1.84	8.75	6.58
Lu	0.002 ppm	0.318	1.78	1.08
FUS-ISE				
F	0.01%	--	0.03	--
TD-ICP				
Ag	0.5 ppm	< 0.5 ppm	< 0.5 ppm	< 0.5 ppm
Cd	0.5 ppm	< 0.5 ppm	< 0.5 ppm	< 0.5 ppm
Cu	1 ppm	10	13	3
Ni	1 ppm	3	4	3
Pb	5 ppm	16	29	31
S	0.001%	0.006	0.005	0.004
Zn	1 ppm	23	33	93

Table 8-2. CIPW normative mineralogy for CMG samples.

Sample ID:	**HBC10-39**	**HBC10-55**	**HBC10-18**
Description:	Roof zone of pluton	Core of pluton	"Lower three"
Normative mineralogy *(Weight % norm)*			
Quartz	34.63	35.45	32.84
Plagioclase	30.98	39.25	36.00
Orthoclase	31.46	22.40	29.16
Corundum	0.68	1.58	0.33
Hypersthene	0.45	0.07	0.25
Rutile	0.16	--	--
Ilmenite	0.02	0.04	0.11
Magnetite	--	0.36	0.05
Hematite	1.44	0.70	1.16
Apatite	0.12	0.05	0.07
Zircon	0.04	--	0.01
Pyrite	0.02	0.02	--
Fluorite	--	0.07	--

Caveat: data are normalized such that total = 100%

this compilation, as it was considered an anomaly by Anderson and Cullers (1999). The Oak Creek pluton is a pervasively foliated peraluminous quartz monzonite to monzogranite which is different from most 1.4 Ga homogeneous granitoids (e.g. the Curecanti pluton) in that it has a lower SiO_2 content (as low as 55%) and is considered to represent the parent magma of more typical 1.4 Ga plutons (Cullers et al., 1993).

All three samples of CMG have high potassium (Fig 8-2B), compared to the majority of 1.7 Ga plutons which have, in general, more variation in potassium levels (Anderson and Cullers, 1999). The interpretation made by Anderson and Cullers (1999) was that early 1.7 Ga granitoids are mostly tholeiitic which were followed by large calc-alkaline batholiths, resulting in a range of compositions for 1.7 Ga granitoids (Fig. 8-2C). The chemistry of 1.4 Ga plutons, on the other hand, has a smaller range: these plutons plot mostly in the WPG field of Figure 8-2A, have high potassium (Fig. 8-2B), and are almost exclusively tholeiitic (Fig. 8-2C).

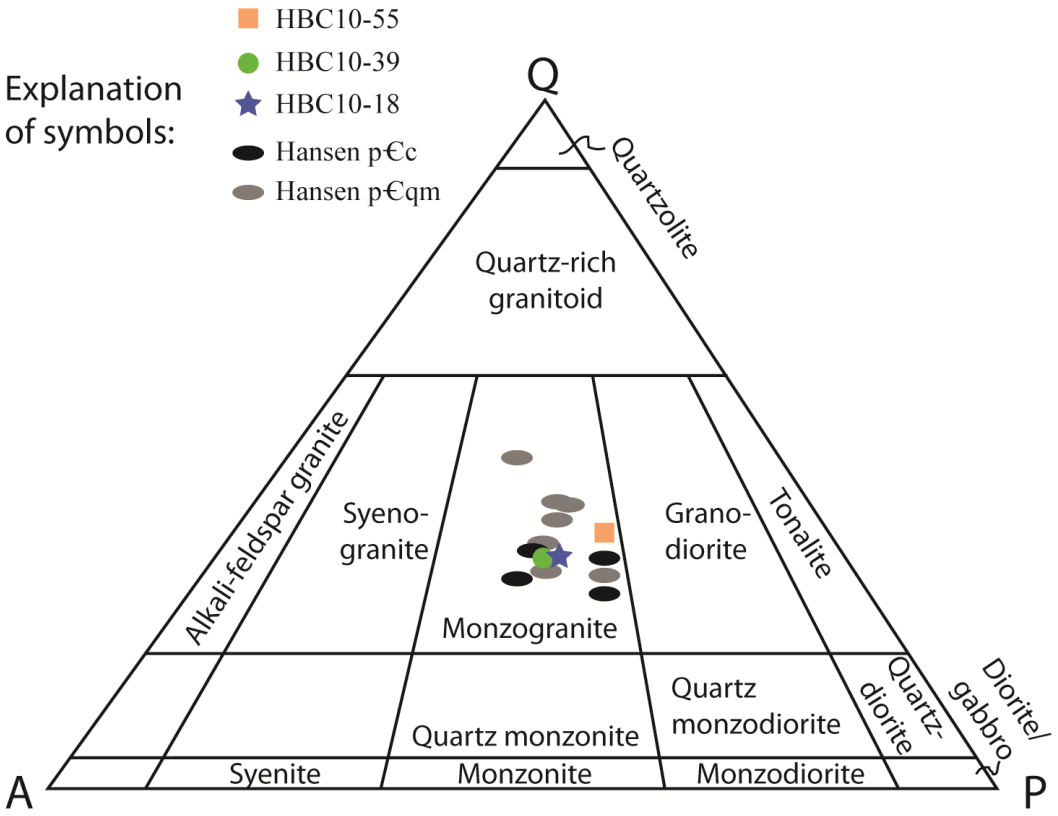

Figure 8-1. QAP diagram of CMG samples and data from Hansen (1964); boundaries from Streckeisen (1974).

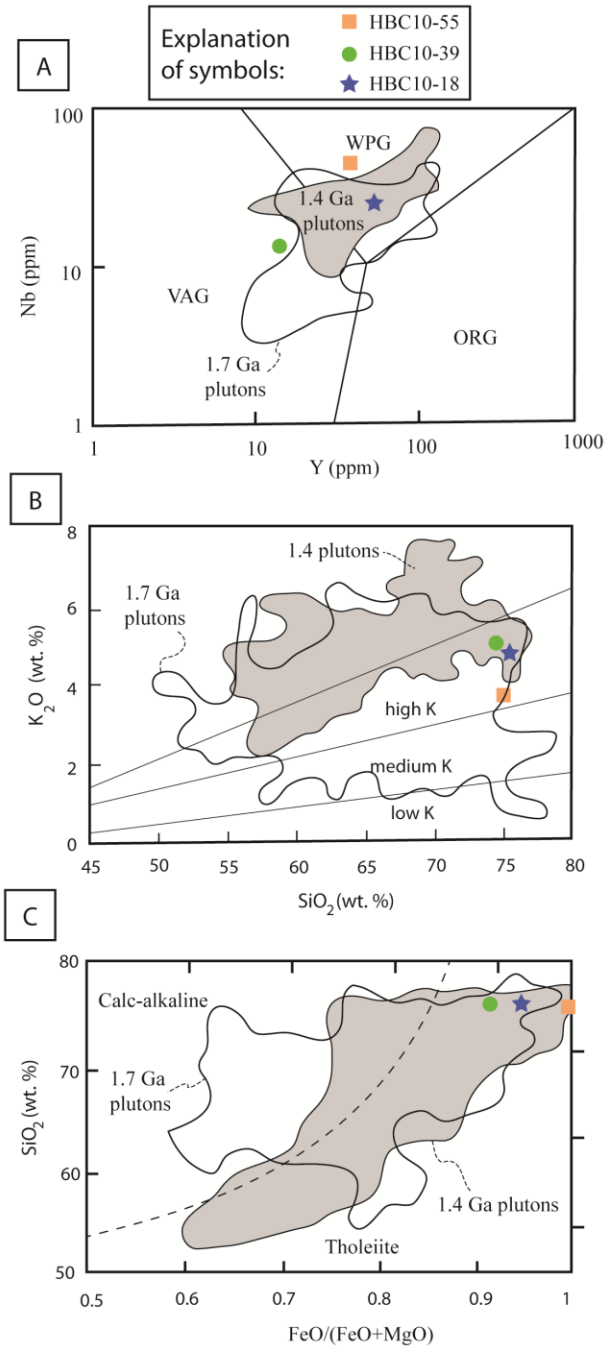

Figure 8-2. Geochemistry of CMG samples discussed in Section 5.4.3 compared to chemical extent of 1.7 Ga (white outlines) and 1.4 Ga (gray outlines) plutons in Colorado and Wyoming from Anderson and Cullers (1999). (A) Nb vs. Y with tectonic discrimination boundaries (within-plate granite, WPG; volcanic arc granite, VAG; ocean ridge granite, ORG) of Pearce et al. (1984). (B) K_2O vs. SiO_2 with potassium-boundaries from Anderson and Cullers (1999). (C) SiO_2 versus FeO/(FeO+MgO) with calc-alkaline/tholeiite distinguishing line of Rickwood (1989). Note the wide range for 1.7 Ga plutons, whereas 1.4 Ga plutons are mostly constrained to the tholeiitic field.

Rare earth elements (REE; La-Lu ± Y) are useful for interpreting the genesis of igneous rocks (Pearce et al., 1984; Cherniak et al., 1993; Rollinson, 1993; Frost et al., 2001). All of these REE form a stable ion with nearly identical physical and chemical properties, so differences are thought to be related to slightly different atomic radii. These differences result in differential fractionation, which is dependent on the tectonic environment, producing a diagnostic REE signature (Rollinson, 1993). A negative Eu anomaly is present in both CMG and data compiled from Anderson and Cullers (1999); Fig. 8-3, a characteristic of rocks with abundant feldspar due to Eu substituting for Sr in feldspar during reducing conditions (Rollinson, 1993). In general, CMG has relatively high light REE abundances (La, Ce; Fig. 8-3), as do most 1.4 Ga granitoids (Anderson and Cullers, 1999). CMG is depleted in Tb and Lu, two heavy REE which the Curecanti pluton consistently has one order of magnitude less of than most 1.4 Ga granitoids (Fig.

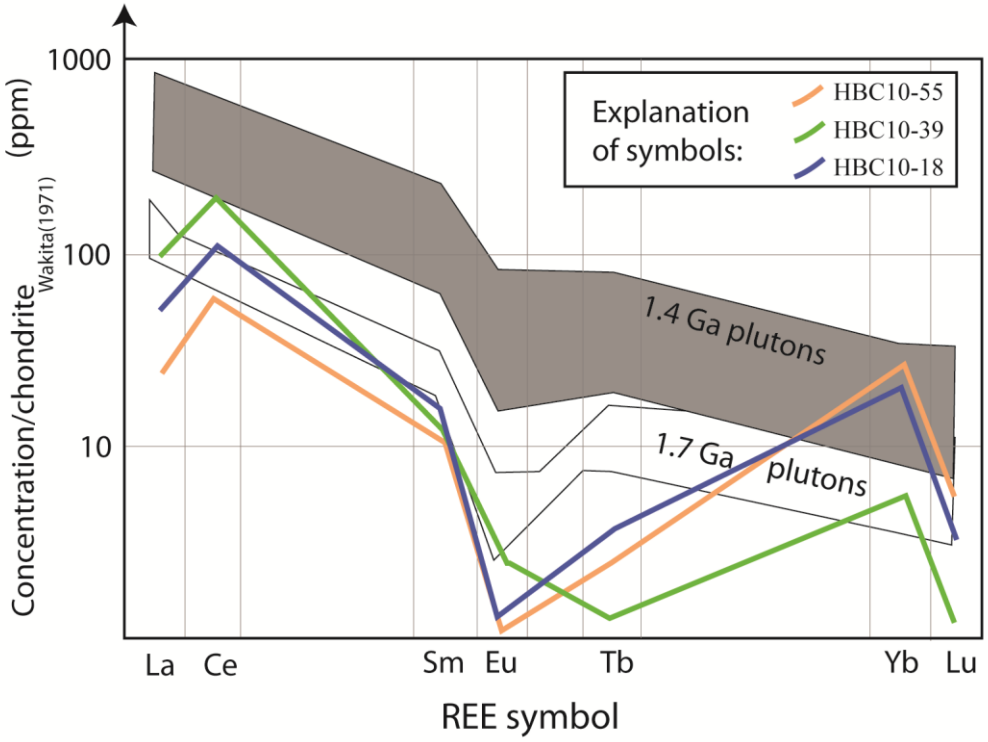

Figure 8-3. Select whole-rock rare earth element chemistry of CMG samples discussed in Section 5.4 normalized to chondrite values of Wakita et al. (1971): La 0.34, Ce 0.91, Sm 0.195, Eu 0.073, Tb 0.047, Yb 0.22, and Lu 0.034. The extent of rare earth element abundances for 1.7 Ga (white outlines) and 1.4 Ga (gray outlines) plutons in Colorado and Wyoming from Anderson and Cullers (1999) using the same chondrite-normalization values.

8-3). CMG's heavy REE depletion relative to other 1.4 Ga granitoids (Anderson and Cullers, 1999) may reflect CMG being sourced from a region with garnet, which will result in depletion of heavy REE (Rollinson, 1993). This may indicate variability in the source regions of 1.4 Ga plutons, a reasonable assumption considering the Proterozoic lithologic variations mapped in the Wet Mountains, an area thought to be representative of the Curecanti pluton source region (Jones et al., 2010).

8.3 Tectonic discrimination diagrams

It is difficult to use major element concentrations to elucidate an emplacement setting for individual granitoids, but trace element abundances may be more sensitive to the tectonic setting (Jakeš and White, 1972; Pearce et al., 1984; Frost et al., 2001; Bonin, 2007). Pearce et al. (1984) developed a series of tectonic discrimination diagrams by plotting trace element abundances of ~ 600 granitoids that were emplaced in a known tectonic environment; they found certain trace element ratios indicative of VAG, WPG, ORG, or syn-collisional (syn-COL) granitoids. The boundaries between granitoids of these chemistries are plotted (Fig. 8-4), along with trace element abundances from the three samples of CMG (discussed in Section 4.4.3). It should be noted that some of these diagrams use Rb, which may be mobile during hydrothermal alteration of granitoids (Mukasa and Henry, 1990); however, as mentioned in Section 4.4.3, care was taken to obtain the freshest possible samples of CMG. In addition, contamination of Ta and Nb may occur when using a tungsten carbide mill during sample preparation (Green, 1995), so multiple lines of evidence are used to establish the relationship of the Curecanti pluton to other 1.4 Ga granitoids.

The core of the Curecanti pluton (i.e. HBC10-55) plots well within the WPG field of Pearce et al. (1984), and the roof of the pluton plots in the VAG field in all but one plot (Fig. 8-4A-C). The contradiction between the tectonic setting implied by the diagrams (Fig. 8-4A-C) may indicate evidence that Rb mobility occurred in these rocks (Mukasa and Henry, 1990), inter-pluton variation (Srogi and Lutz, 1997; Dostal and Chatterjee, 2000; Hoskin and Ireland, 2000), or trace element contamination during sample preparation. While it is concerning that the Curecanti pluton roof (i.e. HBC10-39) would plot in a different tectonic field, it is also encouraging that the Curecanti core and

the correlative dikes below the pluton generally plot close to one another (Figs. 8-2 and 8-4). This chemical evidence supports the interpretation of these two samples being consanguineous, even if they record slightly different strain patterns (Sections 5.4 and 6.4). Anderson and Cullers (1999) argued that the Mesoproterozoic existence of VAG granitoids (Fig. 8-2A) and reactivation of faults (Section 1.2.2) need not preclude this thermal event from being anorogenic, as the majority of 1.4 Ga granitoids, including some CMG samples, appear to have chemistry plotting in the WPG of Pearce et al. (1984; Figs. 8-2 and 8-4).

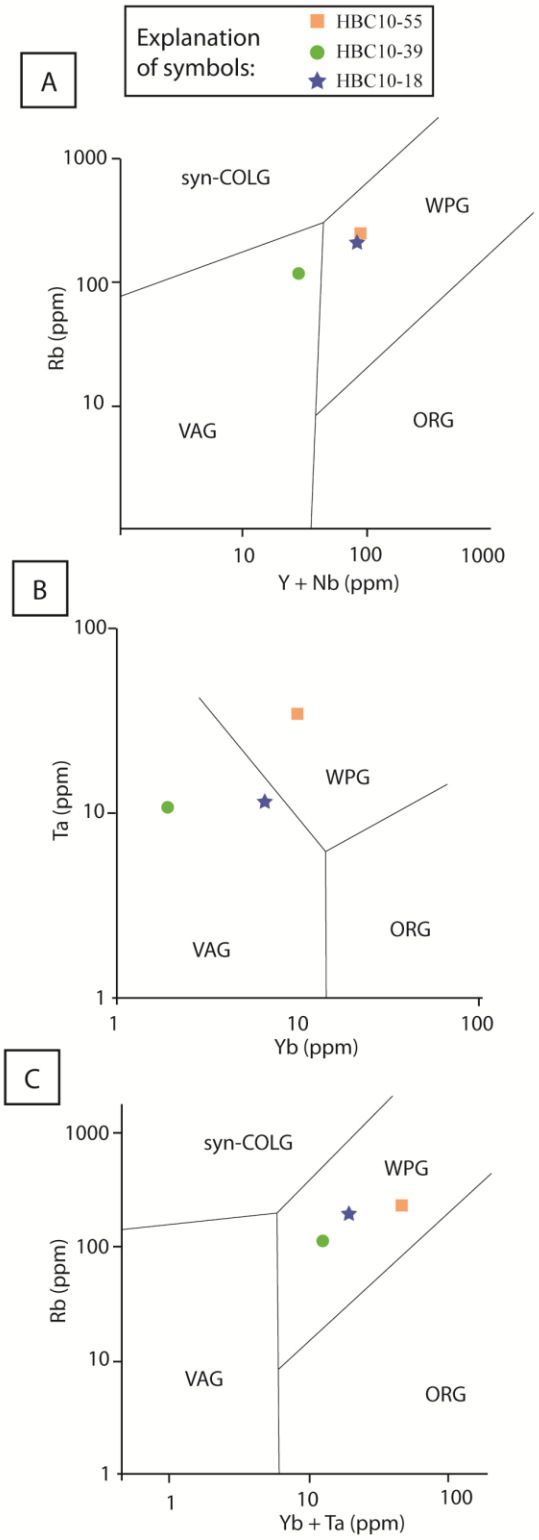

Figure 8-4. (A) Rb-(Y+Nb), (B) Ta-Yb, and (C) Rb-(Yb+Ta) discriminant diagrams for syn-collision (syn-COL), volcanic arc (VA), within plate (WP), and normal and anomalous ocean ridge (OR) granites. Boundaries from Pearce et al. (1984).

CHAPTER 9
DISCUSSION

9.1 Mechanics behind intrusion

Rayleigh-Taylor instabilities (Ryan, 1993) are likely an insufficient mechanism to transport large volumes of granitoid from their source region in the lower crust, through the ductile lower crust, and into the upper brittle crust (Vigneresse, 1995; Menand, 2011). The process of magma wedging, described by Clemens and Mawer (1992) and discussed in Section 1.1.3, postulates that both deformation and buoyancy are required for the distribution of granitoid bodies in the upper crust. This model utilizes the low tensile strength of rocks and presence of Griffith cracks to form Mode I fractures even during applied compression (Fig. 4-6). In brittle rocks, magma will generally propagate perpendicular to the least compressive stress along the σ_1-σ_2 plane (Fig. 9-1A; Jaeger and Cook, 1979; Hutton, 1996; Vigneresse et al., 1999). Mohr Coulomb fractures, typically oriented 30˚ from the principal maximum compressive stress, may alternatively provide preferential paths through which magma may be transported if Griffith cracks are not present (Fig. 9-1B; Clemens and Mawer, 1992). Furthermore, magma can contribute substantially to the local stress field during its ascent; this stress contribution is potentially enough to change the principal stress orientations and thus the orientation of the opening plane (Parsons and Thompson, 1991; Vigneresse et al., 1999). If the supply of magma through a vertical dike is sufficiently high, the local stress field cannot relax, resulting in a horizontal dike (Fig. 9-1C; Vigneresse et al., 1999). As discussed in Section 4.4, magma driving pressure can be used to estimate whether this switch of principal stress orientations will occur.

If CMG did not initially ascend from its source through Mode I tensile fractures, it may have risen at least some distance along its host rock S_2 foliation to its current level at Nelson Gulch (Fig. 9-1B). The Curecanti pluton roof emerges from the level of the Morrow Point Reservoir in Nelson Gulch with an orientation of 300˚, 60˚ SW, subparallel to S_2 at this location. The roof and floor of the Curecanti pluton, exposed along the Pioneer transect, shows that CMG at least locally appears to infiltrate along

host rock leucosome, apparently utilizing these planes as weaknesses. This observation is consistent with other authors who have demonstrated granitoid magma injecting parallel and subparallel to macroscopic foliation (Hall and Kisters, 2012). For a crust in extension, the S_2 at Nelson Gulch is oriented such that σ_1 would be 30˚ from the plane on which the fabric lies. This is the optimal orientation for development of Mohr-Coloumb shear fractures with rocks that contain tensile strength or frictional failure on preexisting weaknesses with no cohesion (Fig. 9-1B; Byerlee, 1978; Fossen, 2010), perhaps implying that magma ascended at least partly along these 60˚ SW-dipping foliation planes. The depth below the Earth's surface to which this S_2 fabric continues at 300˚, 60˚ SW is unknown, but cross-section construction suggests these F_2 folds have an amplitude of around 3-5 km (Fig. 2-2), providing an order of magnitude estimate regarding how far a Coulomb shear fracture could have existed parallel to S_2 at this location.

Figure 9-1 is an attempt to show the observations expected for an intrusion that initially propagates vertically (Fig. 9-1A) or along 60˚-dipping fractures (Fig. 9-1B) and gains enough P_d such that the principal stress acting perpendicular to the dike walls becomes the maximum compressive stress (9-1C). When magma supply diminishes, the principal stress orientations will resume their pre-intrusion orientation, and vertical dikes may once again result. Table 9-1 summarizes the expected observations for each of these steps, the observations made for CMG around Curecanti Needle, and an interpretation regarding the validity of each step.

Using the maximum P_d value of 240 MPa calculated for CMG during crustal extension (Section 7.6), a vertical dike of CMG would have contributed to an initially horizontal σ_3 enough to overcome lithostatic overburden (σ_1), changing the orientation of the σ_1-σ_2 plane from vertical to horizontal at 8 km depth (Fig. 9-1C). Note that 8 km corresponds to the maximum P_d calculated for CMG emplaced during extension, but is on the lower end of the geothermobarometric data presented in Chapter 2.2.2.

Alternatively, a 60˚-dipping dike, as observed at the roof contact of the Curecanti pluton at Nelson Gulch (Fig. 3-5), would exert a force F_i perpendicular to its walls, acting on the horizontal plane $\sigma_3 F_i \sin 60$ (Means, 1976), would not have generated a σ_{diff} sufficient to cause failure along either the Mohr failure envelope of Myrvang (2001) or

Figure 9-1. Semi-schematic Mohr and block diagrams of stress axis exchange due to magma (gray polygons in block diagrams) intrusion during crustal extension ($\sigma_1=\sigma_z$), showing two end-member ascent mechanisms for CMG. (A) Initially, the opening plane (σ_1-σ_2) may have been vertical. (B) Alternatively, failure may result along local S_2 at Nelson Gulch, if it acted as a preexisting weakness, but P_d serves to increases σ_3, shifting the Mohr circle toward the stable field. (C) As P_d increases, it may increase the horizontal stress component such that it becomes to greatest compressive principal stress, changing the σ_1-σ_2 plane from vertical to horizontal, resulting in horizontal sill development. (D) As magma supply diminishes, σ_1-σ_2 one again becomes vertical. See Table 9-1 for observations expected for these four stages and observations made in the Curecanti Needle area.

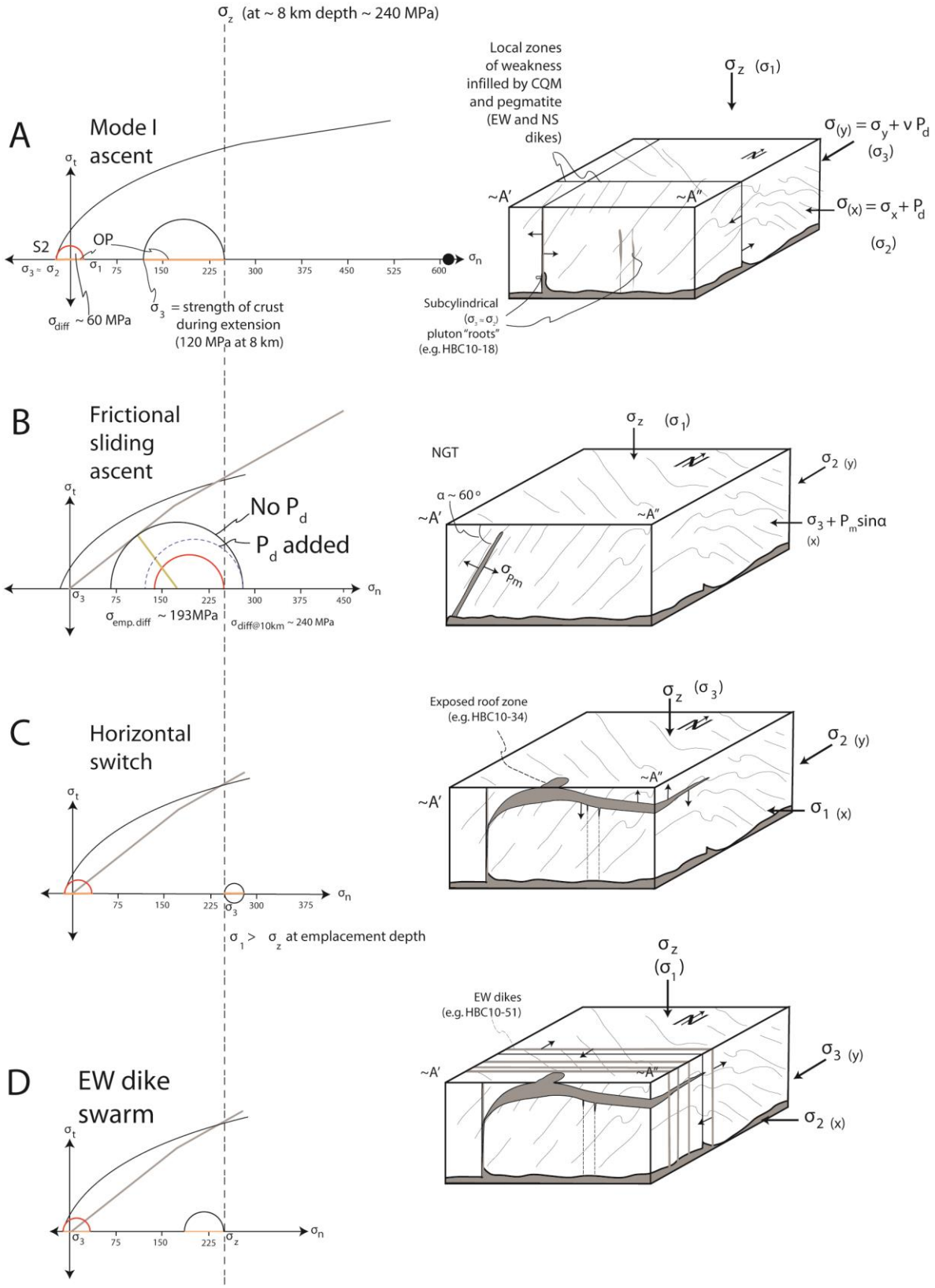
σz (at ~ 8 km depth ~ 240 MPa)
A
Mode I ascent
σt
S2
OP
σ3 ≈ σ2
σ1
σn
75
150
225
300
375
450
525
600
σdiff ~ 60 MPa
σ3 = strength of crust during extension (120 MPa at 8 km)
Local zones of weakness infilled by CQM and pegmatite (EW and NS dikes)
σz (σ1)
σ(y) = σy + ν Pd
(σ3)
σ(x) = σx + Pd
(σ2)
~A′
~A″
Subcylindrical (σ3 ≈ σ2) pluton "roots" (e.g. HBC10-18)
B
Frictional sliding ascent
No Pd
Pd added
σ3
σemp. diff ~ 193MPa
σdiff@10km ~ 240 MPa
NGT
α ~ 60°
σpm
σ2 (y)
σ3 + Pm sinα
(x)
C
Horizontal switch
σ1 > σz at emplacement depth
Exposed roof zone (e.g. HBC10-34)
σ1 (x)
D
EW dike swarm
EW dikes (e.g. HBC10-51)
σ3 (y)
σ2 (x)

the frictional sliding envelope of Byerlee (1978) during extension. Ascent via Mode I tensile fractures, requiring tensile strength and the presence of Griffith cracks, appears to be the most viable mechanism for CMG ascent. A similar argument was made by Clemens and Mawer (1992) for the magma wedging model of magma ascending.

Table 9-1. Expected observations and results for instantaneous stress field switch model for horizontal sill emplacement (Figure 9-1).

Stage of Figure 9-1	**Expected observations**	**Actual observations**	**Interpretation**
A	Subcylindrical vertical dikes NS/EW dikes cross-cut by pluton	Subcylindrical vertical dikes	Oldest history, σ_1-σ_2 plane locally vertical
B	60˚-dipping dikes	Only 60˚-dipping at NGT	Travelled along 60˚-dipping plane short distance
C	Horizontal dike cross-cutting subcyllindral dikes Roof lift/floor sink evidence	Horizontal dike above foliated correlative dikes No strain/thermal aureole; internal fabric oblique to margins	σ_1-σ_2 plane locally horizontal via Mode I Strain partitioned elsewhere Decoupling of pluton/host rocks
D	Cross-cutting dike swarm of late-magmatic fluids	Cross-cutting dike swarm	σ_1-σ_2 plane locally horizontal P_d no longer > σ_z

Proterozoic crust may have been at least locally in extension ca. 1.4 Ga (Anderson, 1983; Ferguson et al., 2004; Duebendorfer, 2007), which would provide the essential vertical σ_1 and relatively low σ_3 components. Alternatively, transpressional and transtensional tectonic environments have been proposed for the southwestern United States at 1.4 Ga (Shaw et al., 2001; Shaw et al., 2005; Jessup et al., 2006; Lee et al., 2012), which could still provide local dilatancy. If these models hold true, these P_d calculations demonstrate that magma wedging (Clemens and Mawer, 1992) and magma driving pressure acting perpendicular to the walls of vertical dikes (Parsons and Thompson, 1991) would have been sufficient to emplace the Curecanti pluton as a horizontal sheet around 8 km below the Earth's surface. The differential stress at emplacement does not intersect the failure envelope in Mohr space (Fig. 9-1C), so Griffith fractures are required to cause a reorientation of the applied stress and the opening of horizontal Mode I fractures (Twiss and Moores, 1992). Alternatively, a horizontal anisotropy (i.e. brittle-ductile transition) could be responsible for arresting the magma, rather than the opening plane rotating to horizontal. In the Curecanti Needle area, it is possible that a change in S_2, such as the hinge zone of the Curecanti antiform, acted as a local anisotropy and/or dilatation. Regional compression does not preclude the model presented in Figure 9-1 from succeeding, as locally dilatant sites can develop even during convergent orogeny (Vigneresse et al., 1999). Time scales for pluton-emplacement are relatively rapid, and a dilatant site need not exist longer than it takes to assemble the melt in the pluton – as short as days or months (Petford et al., 2000).

Evidence of ballooning (Paterson and Vernon, 1995; Hutton, 1996; Tikoff et al., 1999; Brown and McClelland, 2000) is lacking in the Curecanti pluton and host rocks, as the host rock foliation is not deflected at the floor or roof contacts of the pluton. This indicates space for this pluton having been accommodated by an alternative mechanism such as roof lifting via either the piston or cantilever mechanisms of Cruden (1998), floor subsidence, source region compaction, isostatic depression of the Moho, or some combination of the above (Cruden, 1998; Petford et al., 2000; Cruden and McCaffrey, 2001). Unfortunately, these processes are not preserved in the present exposures. The validity of Fig. 9-1C depends on a crustal strength curve having a maximum value

approximately at the depth of emplacement (Sections 7.5 and 7.6); the local least principal stress (σ_3) must have been: **(1)** low enough to generate tensile fractures at the source region, a process which is assisted by Griffith fractures, and **(2)** greater than ~20 MPa at emplacement level for magma driving pressure's maximum addition of ~240 MPa to supersede lithostatic overburden at ~ 8 km depth; the crustal column between CMG source depth and emplacement must have had sufficient tensile strength for CMG to ascend initially through Mode I tensile fractures.

If the local stress field around present-day Curecanti Needle was compressive at 1.4 Ga, mechanisms other than the magma driving pressure model, as utilized as Weertman and Chang (1977) and Hogan et al. (1998) did, must be called upon. As discussed in Section 1.1.2, vertical diking is hindered during compression due to the σ_1-σ_2 plane being horizontal. However, shortening would invoke horizontal σ_1 that, if assisted sufficiently from magma driving pressure and the presence of Griffith cracks, would form horizontal fractures that are parallel to σ_1-σ_2. These surfaces could manifest as horizontal dikes if lithostatic overburden is exceeded due to magma driving pressure increasing the principal stress normal to the wall of dikes through which magma is being transported. Just as vertical diking is hindered during compression, so should horizontal diking be favored due to the magma wedging plane (i.e. σ_1-σ_2) being horizontal. Applying the compressive stress regime to the 60˚-dipping surface of S_2 at Nelson Gulch would create a 60˚ angle between σ_1 and the foliation surface. This would translate to 2Θ angle of 120˚ on the Mohr circle; making this a nearly impossible scenario.

Cruden and McCaffrey (2001) emphasized the importance of a pluton magma source region characteristics in determining both the emplacement level and the final shape of a pluton. Constraints on the Curecanti pluton's source region are limited to gravity data which indicate a large granitoid batholith might have existed beneath the Colorado mineral belt (Tweto and Case, 1972; Isaacson and Smithson, 1976; McCoy and Roy, 2005). Shaw et al. (2005) and Jones et al. (2010) suggested that this gravity low represents the vestige of a mid-crustal magma layer formed at 1.4 Ga where magma pooled at a rheological impediment, possibly the brittle-ductile transition, and fed mid- and upper-crustal plutons such as the Vernal Mesa and Curecanti Pluton. This suggestion

is corroborated by thermobarometric data and field mapping from the southern Wet Mountains that suggests fabric development and igneous activity coeval with that of the Black Canyon of the Gunnison region, but at a deeper structural level.

Local extension is critical to develop the Mode I tensile fractures that the magma wedging model relies upon. However, it is well documented on many scales that an applied stress need not reflect the local stress field around Griffith fractures, which are likely ubiquitous in the brittle crust. In addition, horizontal sills are a well-documented feature in extensional regimes. We suggest that a local extensional field was required for the Curecanti pluton to ascend from its source region as a hot magma with enough buoyant force and differential hydrostatic pressure to overcome lithostatic overburden at some depth, likely around 8-12 kilometers, and "roll over" horizontally.

Because P_d serves to increase σ_3 in the model shown in Figure 9-1, differential stress decreases as P_d rises, resulting in frictional sliding failure only during narrow "depth windows," i.e. only between depths of 10 ± 1 km does failure occur for a magma sourced from 22 kilometers. Assuming connectivity with the source chamber is not broken, CMG's P_d increases as it ascends, which suppresses differential stress (Parsons and Thompson, 1991), bringing the Mohr circle for its immediate host rocks further towards the stability field of Mohr space. However, the presence of Griffith cracks will create a local stress field at their tips, making Mode I ascent a more viable option, consistent with other authors who have observed that tensile failure along the local σ_1-σ_2 plane is the best way to transport magma (Weertman, 1971; Lynch and Morgan, 1987; Parsons and Thompson, 1991; Clemens and Mawer, 1992; Wagner et al., 2006; Ablay et al., 2008; Bons et al., 2012;).

9.2 Is the Curecanti pluton a laccolith, lopolith, or chonolith?

The Curecanti pluton can be thought of as a mostly discordant sill – it has the tabular geometry of a sill, yet is discordant with respect to layering (i.e. mesoscopic foliation, S_2) in its host rock everywhere but at Nelson Gulch. It is now clear that the pluton ascended at least a short distance subparallel to S_2 at Nelson Gulch, turned horizontal, and was emplaced as a 5-km-long mostly discordant dike which tapers out in the hinge zone of a km-scale fold. The turning or "rollover" of a vertical dike to

horizontal is well-documented in mediums that contain horizontal layering; horizontal sills are often documented to sit beneath some rigid layer that they were not able to penetrate, but were able to lift (Corry, 1988; Mahan et al., 2003; Menand, 2008; Stevenson et al., 2007; Ferwerda, 2012). However, the Curecanti pluton, despite its mostly subhorizontal shape, does not rest at the base of any mesoscale anisotropy. A rheological anisotropy is the basis for arresting magmas and the formation of laccoliths in most models (Johnson and Pollard, 1973; Koch et al., 1981; Corry, 1988; Hunt, 1988; Jackson and Pollard, 1988; Roman-Berdiel et al., 1995; Acocella, 2002; Ferwerda, 2012; Menand, 2008). The original definition of laccoliths restricted their genesis to forcible roof-lifting of horizontally bedded rocks between which magma wedged itself (Gilbert, 1880, 1896). Later observations expanded this definition to include at least partly discordant floor and/or roof contacts (Corry, 1988), although the confirmation of roof-lifting should still be an essential distinction between a laccolith and a sill or horizontal dike. A lopolith is similar in that a space-creating mechanism (floor subsidence, in this case) is necessary to its definition. A chonolith, on the other hand, is considered to be a pluton where emplacement was clearly forcible, but where it is unclear whether roof lifting or floor lifting were the primary space-creating mechanisms (Corry, 1988). Referring to this somewhat cumbersome terminology, Charles B. Hunt (1953) once said, tongue in cheek, that “a cactolith is a quasihorizontal chonolith composed of anastomosing ductoliths whose distal ends curl like a harpolith, thin like a sphenolith, or bulge discordantly like an akmolith or ethmolith." What is clear, however, is that these terms are preferable to the standard term “pluton” only if a space-creating mechanism can be demonstrated.

Hansen (1964) considered the Curecanti pluton have been emplaced as a laccolith based on the low to moderate dip of the pluton floor, arched roof, and overall tongue-shaped geometry. While it is now known that laccoliths, sensu stricto, can indeed be emplaced at Curecanti-pluton-like depths (Scaillet et al., 1995; Morgan and Law, 1998; Stevenson et al., 2007; Menand, 2008; Vegas et al., 2008), roof-lifting cannot be confirmed around Curecanti Needle. However, this does not exclude the Curecanti pluton from being a laccolith, as roof-lifting may be accommodated via far-field space creating

mechanisms higher in the crust (Fig. 4-7). The lack of high strain accumulation fabrics (i.e. mylonites, S-C fabrics, etc.) in the pluton, along with a decoupling [i.e. obliquity] between the weak foliation observed in CMG, the Curecanti pluton margins, and its host rock foliation may imply that ballooning was not a primary mechanism for creating space, or that this strain was simply partitioned into a part of the crust not presently exposed. Vegas et al. (2008) showed that nearly all the strain for several 7 km-deep laccoliths was partitioned into surficial bulges of subaqueous sediment, presenting a model in which the classical roof-lifting of Jackson and Pollard (1988) or space-creating mechanisms suggested by Cruden (1998) are not necessary the only manifestations of roof-lifting. As complete as exposure in the Black Canyon of the Gunnison is, there is clearly a great deal of the 1.4 Ga crustal column missing from the record.

CHAPTER 10
CONCLUSIONS

(1) The obliquity between Curecanti pluton contacts, a weak foliation in the pluton floor zone, a coeval dike swarm, and its host rock foliation is contrary to many observations worldwide of pluton's being emplaced parallel to regional layering and/or containing a margin-parallel foliation. The orientation of these planes suggests a switch in the opening plane orientation during emplacement (e.g. the Curecanti pluton) and just after emplacement (e.g. the east-west dike swarm), possibly accompanied by oblique diapirism and subsequent minor deformation of the pluton.

(2) In the past several decades, research on granitoids has shifted away from geochemical studies of magma origin towards studies that address the physical processes involving its rapid ascent and emplacement (Petford et al., 2000). It is now demonstrated that the magma driving pressure model, originally proposed by Weertman (1971), is most efficient during locally extensional environments. If emplaced during local extension, CMG could have risen to a depth of 8 km and been emplaced as a horizontal sheet, as it is presently exposed, due to the magma driving pressure acting perpendicular to the ascending dike walls, serving to sufficiently increase confining pressure until the opening plane became horizontal. On the other hand, if Griffith cracks were not present where P_d for CMG overcame lithostatic overburden, a horizontal anisotropy would be required, as failure would not cause the instantaneous stress field rotation (Fig. 9-1C).

Other authors have also stressed the importance of local extension for a magma to ascend above neutral buoyancy level (Takada, 1989, 1990). While evidence for 1.4 Ga compressional or transpressional orogeny continues to build (Shaw et al., 2005; Daniel and Pyle, 2006; Jones et al., 2010; Jones et al., 2011; Andronicos et al., 2012; Lee et al., 2012), dilatant sites are known to focus melt in the crust (Hall and Kisters, 2012) and may have existed at least locally in the Curecanti area, allowing for the emplacement of the Curecanti pluton as a partly discordant tongue-shaped sheet.

CHAPTER 11
SUGGESTIONS FOR FURTHER WORK

The excellent constraints on the three-dimensional shape of the Curecanti pluton make it an ideal candidate for emplacement mechanism studies. Future studies would greatly benefit from detailed anisotropy of magnetic susceptibility transects and mapping of the Curecanti pluton to determine the existence/extent/nature of a magnetic fabric (de Saint Blanquat et al., 2001) and whether the pluton crystallized while still ascending at Nelson Gulch (Vegas et al., 2008). In addition, some of the criteria to distinguish between magmatic, submagmatic, and solid-state flow require electron backscatter diffraction (EBSD; Section 4.2), which could help further elucidate the origin of the foliation within CMG. Geothermobarometric studies should target the garnet + sillimanite + biotite schist at Nelson Gulch, possibly utilizing monazite chemical dating to delimit the timing of pressure-temperature conditions.

A Rb/Sr date of 1360 ± 40 Ma of a pegmatite dike 3 km east of Curecanti Needle is insufficiently precise to constrain the timing of the ~400 east-west-striking, vertical-dipping pegmatite dikes located just west of Nelson Gulch. These dikes are hereby interpreted to represent a switch in the instantaneous stress field during and after emplacement of the Curecanti pluton, but modern geochronology would be necessary to confirm this relationship. In addition, >200 analyses of zircon grains derived from CMG using laser ablation inductively coupled plasma mass spectrometry were unable to identify anything but 1.7 Ga inherited zircon, and new geochronology, which can improve upon the old Rb/Sr date of Hansen and Peterman (1968), would add value to emplacement-mechanism models and help understand how the Curecanti pluton fits into the worldwide 1.4 Ga thermal event. High precision geochronologic studies should also target the subcyllindrical CMG bodies beneath the Curecanti pluton in Curecanti Creek to support the interpretation that these are indeed consanguineous dikes that may have fed the main pluton. The timing of melting, specifically the leucosome in the host migmatites, would be useful to constrain regional deformation models for the crust during the Mesoproterozoic, and to constrain the degree of leucosome-injection which the Curecanti pluton was responsible for.

REFERENCES CITED

Ablay, G. J., Clemens, J. D., and Petford, N., 2008, Large-scale mechanics of fracture-mediated felsic magma intrusion driven by hydraulic inflation and buoyancy pumping: Geological Society, London, Special Publications, v. 302, no. 1, p. 3-29.

Acocella, V., 2002, Space accommodation by roof lifting during pluton emplacement at Amiata (Italy): Terra Nova, v. 12, no. 4, p. 149-155.

Afifi, A. M., 1981, Precambrian geology of the Iris area, Gunnison and Saguache counties, Colorado. MS thesis, Colorado School of Mines, Golden.

Amato, J. M., Boullion, A. O., Serna, A. M., Sanders, A. E., Farmer, G. L., Gehrels, G., and Wooden, J. L., 2008, Evolution of the Mazatzal province and the timing of the Mazatzal orogeny: Insights from U-Pb geochronology and geochemistry of igneous and metasedimentary rocks in southern New Mexico: Geological Society of America Bulletin, v. 120, no. 3/4, p. 328-348.

Amato, J. M., Heizler, M. T., Boullion, A. O., Sanders, A. E., Toro, J., McLemore, V. T., and Andronicos, C. L., 2011, Syntectonic 1.46 Ga magmatism and rapid cooling of a gneiss dome in the southern Mazatzal Province: Burro Mountains, New Mexico: Geological Society of America Bulletin, v. 123, no. 9-10, p. 1720-1744.

Anderson, E. M., 1951, The Dynamics of Faulting and Dyke Formation with Applications to Britain, Edinburgh and London, Oliver and Boyd Ltd.

Anderson, J. L., 1983, Proterozoic anorogenic granite plutonism of North America: Memoir - Geological Society of America, v. 161, p. 133-154.

Anderson, J. L., and Cullers, R. L., 1999, Paleo- and Mesoproterozoic granite plutonism of Colorado and Wyoming: Rocky Mountain Geology, v. 34, no. 2.

Anderson, J. L., and Morrison, J., 2005, Ilmenite, magnetite, and peraluminous Mesoproterozoic anorogenic granites of Laurentia and Baltica: Lithos, v. 80, no. 1-4, p. 45-60.

Andronicos, C., Aronoff, R. F., Daniel, C., Hunter, R. A., Jones, J. V. I., and Vervoort, J., 2012, Contrasting Precambrian tectonic histories in northern New Mexico and southern Colorado: Abstracts with Programs - Geological Society of America, v. 44, no. 6.

Anhaeusser, C. R., 2010, Magmatic and structural characteristics of the ca. 3440 Ma Theespruit pluton, Barberton Mountain Land, South Africa: American Journal of Science, v. 310, no. 9, p. 1136-1167.

Aronoff, R. F., Vervoort, J., Andronicos, C., and Hunter, R. A., 2012, Lu-Hf garnet geochronology and microstructural analysis constrain the timing of crustal assembly in southwestern North America: Abstracts with Programs - Geological Society of America, v. 44, no. 7, p. 525.

Baer, G., and Reches, Z. e., 1991, Mechanics of emplacement and tectonic implications of the Ramon dike systems, Israel: Journal of Geophysical Research, v. 96, no. B7, p. 11,895-811,910.

Bartley, J. M., Glazner, A. F., and Mahan, K. H., 2012, Formation of pluton roofs, floors, and walls by crack opening at Split Mountain, Sierra Nevada, California: Geosphere, v. 8, no. 5, p. 1086-1103.

Bell, T. H., and Johnson, S. E., 1989, The role of deformation partitioning in the deformation and recrystallization of plagioclase and K-feldspar in the Woodroffe Thrust mylonite zone, central Australia. Journal of Metamorphic: Journal of Metamorphic Geology, v. 7, p. 151-168.

Benn, K., Odonne, F., and de Saint Blanquat, M., 1998, Pluton emplacement during transpression in brittle crust: new views from analogue experiments: Geology, v. 26, no. 12, p. 1079-1082.

Bennett, V. C., and DePaolo, D. J., 1987, Proterozoic crustal history of the western United States as determined by neodymium isotopic mapping: Geological Society of America Bulletin, v. 99, no. 5, p. 674-685.

Berger, A. R., and Pitcher, W. S., 1970, Structures in Granitic Rocks: A Commentary and a Critique on Granite Tectonics: Proceedings of the Geologists' Association, v. 81, no. 3, p. 441-461.

Bickford, M. E., and Boardman, S. J., 1984, A Proterozoic volcano-plutonic terrane, Gunnison and Salida areas, Colorado: The Journal of Geology, p. 657-666.

Bickford, M. E., Bowring, S. A., and Gray, J. E., 1982, Chronology of igneous events in the Proterozoic of central Colorado: Abstracts with Programs - Geological Society

of America, v. 14, no. 6, p. 303.

Bickford, M. E., and Hill, B. M., 2007, Does the arc accretion model adequately explain the Paleoproterozoic evolution of southern Laurentia?: An expanded interpretation: Geology, v. 35, no. 2, p. 167-170.

Bickford, M. E., Mueller, P. A., Kamenov, G. D., and Hill, B. M., 2008, Crustal evolution of southern Laurentia during the Paleoproterozoic: Insights from zircon Hf isotopic studies of ca. 1.75 Ga rocks in central Colorado: Geology, v. 36, no. 7, p. 555-558.

Bickford, M. E., Shuster, R. D., and Boardman, S. J., 1989, U-Pb geochronology of the Proterozoic volcano-plutonic terrane in the Gunnison and Salida areas, Colorado: Special Paper - Geological Society of America, v. 235, p. 33-48.

Bonin, B., 2007, A-type granites and related rocks: evolution of a concept, problems and prospects: Lithos, v. 97, no. 1, p. 1-29.

Bons, P. D., Elburg, M. A., and Gomez-Rivas, E., 2012, A review of the formation of tectonic veins and their microstructures: Journal of Structural Geology, v. 43, no. 0, p. 33-62.

Bouchez, J. L., Delas, C., Gleizes, G., and Nédélec, A., 1992, Submagmatic microfractures in granites: Geology, v. 20, p. 35-38.

Bowring, S. A., and Karlstrom, K. E., 1990, Growth, stabilization, and reactivation of Proterozoic lithosphere in the southwestern United States: Geology, v. 18.

Brown, E. H., and McClelland, W. C., 2000, Pluton emplacement by sheeting and vertical ballooning in part of the southeast Coast Plutonic Complex, British Columbia: Geological Society of America Bulletin, v. 112, no. 5, p. 708-719.

Brown, M., 1994, The generation, segregation, ascent and emplacement of granite magma: the migmatite-to-crustally-derived granite connection in thickened orogens: Earth-Science Review, v. 36.

Brown, M., Averkin, Y. A., and McLellan, E. L., 1995, Melt segregation in migmatites: Journal of Geophysical Research, v. 100, no. B8.

Brown, M., and Solar, G. S., 1998, Granite ascent and emplacement during contractional deformation in convergent orogens: Journal of Structural Geology, v. 20, no. 9-10.

-, 1999, The mechanism of ascent and emplacement of granite magma during transpression: a syntectonic granite paradigm: Tectonophysics, v. 312.

Burg, J. P., and Vanderhaeghe, O., 1993, Structures and way-up criteria in migmatites, with application to the Velay dome (French Massif Central): Journal of Structural Geology, v. 15, no. 11.

Burnham, C. W., 1979, The importance of volatile constituents, *in* Yoder, H. S. J., ed., The evolution of the igneous rocks; Fiftieth Anniversary Perspectives: Princeton, New Jersey, Princeton University Press, p. 439-478.

Burnham, C. W., and Nekvasil, H., 1986, Equilibrium properties of granite pegmatite magmas: American Mineralogist, v. 71, no. 3-4, p. 239-263.

Byerlee, J. D., 1978, Friction of rocks: Pure and applied Geophysics, v. 116, no. 4, p. 615-626.

Castro, A., 1987, On granitoid emplacement and related structures. A review: Geologische Rundschau, v. 76, no. 1, p. 101-124.

Chappell, B. W., White, A. J. R., and Wyborn, D., 1987, The Importance of Residual Source Material (Restite) in Granite Petrogenesis: Journal of Petrology, v. 28, no. 6.

Chen, G. N., and Grapes, R. H., 2007, Granite genesis: In-situ melting and crustal evolution; Netherlands, Springer Dordrecht, p. 1-278.

Cherniak, D. J., Watson, E. B., and in Hanchar, J. M., and Hoskin, P.W.O., eds, 1993, Diffusion in zircon: Reviews in Mineralogy and Geochemistry, v. 53.

Christensen, N. I., 1996, Poisson's ratio and crustal seismology: Journal of Geophysical Research, v. 101, no. B2, p. 3139-3156.

Clemens, J. D., and Mawer, C. K., 1992, Granitic magma transport by fracture propagation: Tectonophysics, v. 204.

Clemens, J. D., and Petford, N., 1999, Granitic melt viscosity and silicic magma dynamics in contrasting tectonic settings: Journal of the Geological Society, v. 156, p. 1057-1060.

Coffman, J. D., Gilbert, G. K., and McConnell, 1986, An interpretation of the crustal structure of the Southern Oklahoma Aulacogen satisfying gravity data, *in* Gilbert, G. K., ed., Petrology of the Cambrian Wichita Mountains Igneous Suite, Volume Guidebook: Norman, Oklahoma Geological Survey, p. 10.

Condie, K. C., 1982, Plate-tectonics model for Proterozoic continental accretion in the southwestern United States: Geology, v. 10, no. 1, p. 37-42.

Corry, C. E., 1988, Laccoliths: mechanics of emplacement and growth: Special Paper - Geological Society of America, v. 220.

Courrioux, G., 1987, Oblique diapirism: the criffel granodiorite/granite zones pluton (southwest Scotland): Journal of Structural Geology, v. 9, no. 3, p. 313-330.

Cruden, A. R., 1998, On the emplacement of tabular granites: Journal of the Geological Society, London, v. 155, p. 9.

Cruden, A. R., and McCaffrey, K. J. W., 2001, Growth of plutons by floor subsidence: implications for rates of emplacement, intrusion spacing and melt-extraction mechanisms: Physics and Chemistry of the Earth, Part A: Solid Earth and Geodesy, v. 26, no. 4, p. 303-315.

Cullers, R. L., Stone, J., Anderson, J. L., Sassarini, N., and Bickford, M. E., 1993, Petrogenesis of Mesoproterozoic Oak Creek and West McCoy Gulch plutons, Colorado: an example of cumulate unmixing of a mid-crustal, two-mica granite of anorogenic affinity: Precambrian Research, v. 62.

Daniel, C., Pfeifer, L. S., Jones, J. V. I., and McFarlane, C. M., 2012, Detrital zircon evidence for Mesoproterozoic deposition, orogenesis and non-Laurentian provenance in the Picuris Mountains, New Mexico, USA: Abstracts with Programs - Geological Society of America, v. 44, no. 7, p. 36.

-, 2013, Detrital zircon evidence for non-Laurentian provenance, Mesoproterozoic (ca. 1490–1450 Ma) deposition and orogenesis in a reconstructed orogenic belt, northern New Mexico, USA: defining the Picuris Orogeny: Geological Society of

America Bulletin, v. IN REVIEW.

Daniel, C., and Pyle, J. M., 2006, Monazite–Xenotime Thermochronometry and Al2SiO5 Reaction Textures in the Picuris Range, Northern New Mexico, USA: New Evidence for a 1450–1400Ma Orogenic Event: Journal of Petrology, v. 47, no. 1, p. 97-118.

Davidson, C., Schmidt, S. M., and Hollister, L., 2007, Role of melt during deformation in the deep crust: Terra Nova, v. 6, p. 133-142.

de Saint Blanquat, M., Law, R. D., Bouchez, J. L., and Morgan, S., 2001, Internal structure and emplacement of the Papoose Flat pluton: An integrated structural, petrographic, and magnetic susceptibility study: Geological Society of America Bulletin, v. 113, no. 8.

de Voogd, B., Serpa, L., Brown, L. D., Hauser, E., Kaufman, S., Oliver, J., Troxel, B. W., Willemin, J., and Wright, L. A., 1986, Death Valley bright spot: A midcrustal magma body in the southern Great Basin, California?: Geology, v. 14, no. 1, p. 64-67.

Demartis, M., Pinotti, L. P., Coniglio, J. E., D'Eramo, F. J., Tubía, J. M., Aragón, E., and Insúa, L. A. A., 2011, Ascent and emplacement of pegmatitic melts in a major reverse shear zone (Sierras de Córdoba, Argentina): Journal of Structural Geology, v. 33, p. 1334-1346.

Donath, F. A., 1972, Effects of cohesion and granularity on deformational behavior of anisotropic rock: Studies in mineralogy and Precambrian geology, v. 135, p. 95-128.

Dostal, J., and Chatterjee, A. K., 2000, Contrasting behaviour of Nb/Ta and Zr/Hf ratios in a peraluminous granitic pluton (Nova Scotia, Canada): Chemical Geology, v. 163, no. 1, p. 207-218.

Duebendorfer, E., 2007, Crust formation in the western United States: Geological Society of America, p. 1.

Ferguson, C. B., Duebendorfer, E. M., and Chamberlain, K. R., 2004, Synkinematic intrusion of the 1.4-Ga Boriana Canyon pluton, northwestern Arizona: Implications for ca. 1.4-Ga regional strain in the western United States: The

Journal of Geology, v. 112.

Ferwerda, B. P., Dike-sill transitions in the san rafael volcanic field, Utah: implications for sill emplacement mechanisms, *in* Proceedings Geological Society of America Abstracts with Programs 2012, Volume 44, p. 0.

Fossen, H., 2010, Structural Geology, Cambridge University Press.

Frost, B. R., Barnes, C. G., Collins, W. J., Arculus, R. J., Ellis, D. J., and Frost, C. D., 2001, A Geochemical Classification for Granitic Rocks: Journal of Petrology, v. 42, no. 11.

Frost, C. D., and Frost, B. R., 1997, Reduced rapakivi-type granites: The tholeiite connection: Geology, v. 25, no. 7.

Gapais, D., and Barbarin, B., 1989, Quartz fabric transition in a cooling syntectonic granite (Hermitage Massif, France): Tectonophysics, v. 125, no. 4, p. 357-370.

Gilbert, G. K., 1880, Geology of the Henry Mountains.

-, 1896, Laccolites in southeastern Colorado: The Journal of Geology, p. 816-825.

Graubard, C. M., and Mattinson, J. M., 1990, Syntectonic emplacement of the approximately 1440 Ma Mt: Evans Pluton and history of motion along the Idaho Springs–Ralston Creek shear zone, central Front Range, Colorado: Geological Society of America Abstracts with Programs, v. 22, no. 6, p. 12.

Green, T. H., 1995, Significance of Nb/Ta as an indicator of geochemical processes in the crust-mantle system: Chemical Geology, v. 120, no. 3, p. 347-359.

Hall, D., and Kisters, A., 2012, The stabilization of self-organised leucogranite networks—Implications for melt segregation and far-field melt transfer in thecontinental crust: Earth and Planetary Science Letters, no. 355, p. 1-12.

Handin, J., 1969, On the Coulomb-Mohr failure criterion: Journal of Geophysical Research, v. 74, no. 22, p. 5343-5348.

Hansen, W. R., 1964, Curecanti pluton, an unusual intrusive body in the Black Canyon of the Gunnison, Colorado: U. S. Geological Survey Bulletin, p. D1-D15.

-, 1965, The Black Canyon of the Gunnison: Today and Yesterday: U. S. Geological Survey Bulletin, v. 1191, p. 84.

-, 1971, Geologic map of the Black Canyon of the Gunnison River and vicinity, western Colorado: U. S. Geological Survey Misc. Geologic Investigations I-0584, scale 1 : 31,680, 2 sheets.

-, 1972, Geology of the Black Ridge: U.S. Geological Survey Miscellaneous Geologic Quadrangle Map GQ-747, scale 1 : 24,000, 1 sheet.

-, 1987, The Black Canyon of the Gunnison in depth, ed. 2, Western National Parks Association, Tucson, Arizona.

Hansen, W. R., and Peterman, Z. E., 1968, Basement-rock geochronology of the Black Canyon of the Gunnison, Colorado: U. S. Geological Survey Professional Paper, p. C80-C90.

Hibbard, M. J., 1979, Myrmekite as a marker between preaqueous and postaqueous phase saturation in granitic systems: Geological Society of America Bulletin, v. 90, no. 11, p. 1047-1062.

Hill, B. M., and Bickford, M. E., 2001, Paleoproterozoic rocks of central Colorado: Accreted arcs or extended older crust?: Geology, v. 29, no. 11, p. 1015-1018.

Hill, J. D., 1988, Late Devonian peraluminous granitic plutons in the Canso area, eastern Meguma Terrane, Nova Scotia: Atlantic Geology, v. 24, no. 1.

Hirth, G., and Tullis, J., 1992, Dislocation creep regimes in quartz aggregates: Journal of Structural Geology, v. 14, p. 145-159.

Hoffman, P. F., 1989, Speculation on Laurentia's first gigayear (2.0 to 1.0 Ga): Geology, v. 17.

Hogan, J. P., and Gilbert, G. K., 1995, The A-type Mount Scott Granite sheet: Importance of crustal magma traps: Journal of Geophysical Research, v. 100, no. B8, p. 779-792.

Hogan, J. P., Price, J. D., and Gilbert, M. C., 1998, Magma traps and driving pressure: consequences for pluton shape and emplacement in an extensional regime:

Journal of Structural Geology, v. 20, no. 9-10.

Hollocher, K., 2003, CIPW Normative Calculation: Schenectady, NY, Geology Department, Union College.

Hoskin, P. W. O., and Ireland, T. R., 2000, Rare earth element chemistry of zircon and its use as a provenance indicator: Geology, v. 28, no. 7, p. 627-630.

Hunt, C. B., 1953, Geology and geography of the Henry Mountains region, Utah: a survey and restudy of one of the classic areas in geology, US Govt. Print. Off., v. 228.

-, 1988, The laccolith-stock controvery: New results from the southern Henry Mountains, Utah: Discussion and reply: Geological Society of America Bulletin, v. 100.

Hunter, J. F., 1925, Pre-Cambrian rocks of Gunnison River, Colorado.

Huppert, H. E., and Sparks, R. S. J., 1989, Chilled margins in igneous rocks: Earth and Planetary Science Letters, v. 92, no. 3, p. 397-405.

Hutton, D. H. W., 1996, The 'space problem' in the emplacement of granite: Episodes, v. 19, no. 4, p. 114-119.

Hyndman, D. W., 1985, Petrology of igneous and metamorphic rocks, McGraw-Hill New York.

Inglis, J. D., Samson, S. D., D'lemos, R. S., and Miller, B. V., 2005, Timing of Cadomian deformation and magmatism within La Hague, NW France: Journal of the Geological Society, v. 162, no. 2, p. 389-400.

Isaacson, L. B., and Smithson, S. B., 1976, Gravity anomalies and granite emplacement in west-central Colorado: Geological Society of America Bulletin, v. 87, p. 22-28.

Jackson, M. D., and Pollard, D. D., 1988, The laccolith-stock controversy: New results from the southern Henry Mountains, Utah: Geological Society of America Bulletin, v. 100, p. 117.

Jaeger, J. C., and Cook, N. G., 1979, Fundamentals of Rock Mechanics: Chapman and Hall, London, p. 593.

Jahns, R. H., and Burnham, C. W., 1969, Experimental Studies of Pegmatite Genesis: A Model for the Derivation and Crystallization of Granitic Pegmatite: Society of Economic Geologists, Inc., v. 64, p. 843-864.

Jakeš, P., and White, A. J. R., 1972, Major and trace element abundances in volcanic rocks of orogenic areas: Geological Society of America Bulletin, v. 83, no. 1, p. 29-40.

Jessup, M. J., Jones, J. V. I., Karlstrom, K. E., Williams, M. L., Connelly, J. N., and Heizler, M. T., 2006, Three Proterozoic orogenic episodes and an intervening exhumation event in the Black Canyon of the Gunnison region, Colorado: The Journal of Geology, v. 115.

Jessup, M. J., Karlstrom, K. E., Connelly, J. N., Williams, M. L., Livaccari, R., Tyson, A., and Rogers, S. A., 2005, Complex Proterozoic crustal assembly of southwestern North America in an arcuate subduction system; the Black Canyon of the Gunnison, southwestern Colorado: Geophysical Monograph, v. 154, p. 21-38.

Johnson, A. M., and Pollard, D. D., 1973, Mechanics of growth of some laccolithic intrusions in the Henry Mountains, Utah: Tectonophysics, v. 18.

Jones, J. V. I., Connelly, J. N., Karlstrom, K. E., Williams, M. L., and Doe, M. F., 2009, Age, provenance, and tectonic setting of Paleoproterozoic quartzite successions in the southwestern United States: Geological Society of America Bulletin, v. 121, no. 1-2, p. 247-264.

Jones, J. V. I., Daniel, C., Frei, D., and Thrane, K., 2011, Revised regional correlations and tectonic implications of Paleoproterozoic and Mesoproterozoic metasedimentary rocks in northern New Mexico, USA: New findings from detrital zircon studies of the Hondo Group, Vadito Group, and Marqueñas Formation: Geosphere, v. 7, no. 4, p. 974-991.

Jones, J. V. I., Rogers, S. A., and Connelly, J. N., 2010, U-Pb geochronology of Proterozoic granites in the Sawatch Range, central Colorado, U.S.A.: Rocky Mountain Geology, v. 45, no. 1.

Jones, J. V. I., Siddoway, C. S., and Connelly, J. N., 2010, Characteristics and

implications of ca. 1.4 Ga deformation across a Proterozoic mid-crustal section, Wet Mountains, Colorado, USA: Lithosphere, v. 2, no. 2.

Karlstrom, K. E., 1989, Toward a syntectonic paradigm for granitoids: EOS Transactions, v. 70, p. 762-762.

Karlstrom, K. E., Åhäll, K., Harlan, S., Williams, M. L., McLelland, J., and Geissman, J. W., 2001, Long-lived (1.8–1.0 Ga) convergent orogen in southern Laurentia, its extensions to Australia and Baltica, and implications for refining Rodinia: Precambrian Research, v. 111, no. 1, p. 5-30.

Karlstrom, K. E., and Bowring, S. A., 1988, Early Proterozoic assembly of tectonostratigraphic terranes in southwestern North America: The Journal of Geology, v. 96.

Karlstrom, K. E., Whitmeyer, S. J., Williams, M. L., Bowring, S. A., and Jessup, M. J., 2007, Does the arc-accretion model adequately explain the Paleoproterozoic evolution of southern Laurentia: An expanded interpretation: COMMENT AND REPLY: Geology, v. 35, no. 1, p. e143-e144.

Kilian, R., Heilbronner, R., and Stünitz, H., 2011, Quartz grain size reduction in a granitoid rock and the transition from dislocation to diffusion creep: Journal of Structural Geology, v. 33, no. 8, p. 1265-1284.

Kirby, E., Karlstrom, K. E., and Andronicos, C. L., 1995, Tectonic setting of the Sandia pluton: An orogenic 1.4 Ga granite in New Mexico: Tectonics, v. 14, no. 1.

Koch, F. G., Johnson, A. M., and Pollard, D. D., 1981, Monoclinal bending of strata over laccolithic intrusions: Tectonophysics, v. 74.

Lee, P. E., Jessup, M. J., Shaw, C. A., Hicks III, G. L., and Allen, J. L., 2012, Strain partitioning in the mid-crust of a transpressional shear zone system: Insights from the Homestake and Slide Lake shear zones, central Colorado: Journal of Structural Geology, v. 39, p. 237-252.

Lister, J. R., and Kerr, R. C., 1991, Fluid-mechanical models of crack propagation and their application to magma transport in dykes: Journal of Geophysical Research, v. 96, no. B6, p. 10049-10010,10077.

Livaccari, R. F., Bowring, T. J., Farmer, E. T., Garhart, K. S., Hosak, A. M., Navarre, A.

K., Peterman, J. S., Rollins, S. M., Williams, C. A., and Kunk, M., Proterozoic rocks of the Uncompahgre Plateau, western Colorado and eastern Utah, *in* Proceedings Geological Society of America Abstracts with Programs 2001, Volume 33, p. 44.

Lynch, H. D., and Morgan, P., 1987, The tensile strength of the lithosphere and the localization of extension, *in* Coward, M. P., Dewey, J. F., and Hancock, P. L., eds., Continental Extensional Tectonics, Geological Society of London Special Publication, p. 53-65.

Ma, H. Y., 1948, On the Occurrence of Agmatite in the Rogart Migmatite Area, Sutherland: A Study in Granitization: Geological Magazine, v. 85, no. 01, p. 1-18.

Maggi, A., Jackson, J. A., McKenzie, D., and Priestley, K., 2000, Earthquake focal depths, effective elastic thickness, and the strength of the continental lithosphere: Geology, v. 28, no. 6.

Mahan, K. H., Bartley, J. M., Coleman, D. S., Glazner, A. F., and Carl, B. S., 2003, Sheeted intrusion of the synkinematic McDoogle pluton, Sierra Nevada, California: Geological Society of America Bulletin, v. 115, no. 12, p. 1570-1582.

Marsh, B. D., 1982, On the mechanics of igneous diapirism, stoping, and zone melting: American Journal of Science, v. 282.

McCaffrey, K. J. W., 1992, Igneous emplacement in a transpressive shear zone. Ox Mountains igneous complex: Journal of Structural Geology, v. 149, p. 221-235.

McClintock, F. A., and Walsh, J. B., Friction on Griffith cracks in rocks under pressure, *in* Proceedings Proc. 4th US Nat. Congr. Appl. Mech 1962, Volume 2, p. 1015-1022.

McCoy, A. M., and Roy, M., 2005, Gravity Modeling of the Colorado Mineral Belt: American Geophysical Union Monograph, v. 154, p. 99-106.

Means, W. D., 1976, Stress and strain: Basic concepts of continuum mechanics for geologists, Springer-Verlag.

Mehnert, K. R., 1968, Migmatites and the origin of granitic rocks, Elsevier Amsterdam.

Menand, T., 2008, The mechanics and dynamics of sills in layered elastic rocks and their implications for the growth of laccoliths and other igneous complexes: Earth and Planetary Science Letters, v. 267, p. 93-99.

-, 2011, Physical controls and depth of emplacement of igneous bodies: A review: Tectonophysics, v. 500, p. 11-19.

Miller, C. F., Furbish, D. J., Walker, B. A., Claiborne, L. L., Koteas, G. C., Bleick, H. A., and Miller, J. S., Growth of plutons by incremental emplacement of sheets in crystal-rich host: Evidence from Miocene intrusions of the Colorado River region, Nevada, USA: Tectonophysics, v. 500, p. 65-77.

Miller, R. B., and Paterson, S. R., 1994, The transition from magmatic to high-temperature solid-state deformation: implications from the Mount Stuart batholith, Washington: Journal of Structural Geology, v. 16, no. 6, p. 853-865.

-, 1999, In defense of magmatic diapirs: Journal of Structural Geology, v. 21, no. 8, p. 1161-1173.

Miller, R. B., Paterson, S. R., and Matzel, J. P., 2009, Plutonism at different crustal levels: Insights from the ~5-40 km (paleodepth) North Cascades crustal section, Washington: The Geological Society of America Special Paper, v. 456.

Morgan, S., and Law, R. D., 1998, Laccolith-like emplacement model for the Papoose Flat pluton based on porphyroblast-matrix analysis: Geological Society of America Bulletin, v. 110, no. 1.

Mukasa, S. B., and Henry, D. J., 1990, The San Nicolás batholith of coastal Peru: early Palaeozoic continental arc or continental rift magmatism?: Journal of the Geological Society, v. 147, no. 1, p. 27-39.

Myrvang, A., 2001, Bergmekanikk (Rock mechanics): Trondheim, Norway, NTNU: Norwegian University of Science and Technology.

Nyman, M. W., Karlstrom, K. E., Kirby, E., and Graubard, C. M., 1994, Mesoproterozoic contractional orogeny in western North America: Evidence from ca. 1.4 Ga plutons: Geology, v. 22.

Olson, J. C., and Hedlund, D. C., 1973, Geologic map of the Gateview quadrangle,

Gunnison County, Colorado. U.S. Geological Survey Quadrangle Map GQ-1071, scale 1 : 24,000, 1 sheet.

Parsons, T., and Thompson, G. A., 1991, The role of magma overpressure in suppressing earthquakes and topography: Worldwide examples: Science, v. 253, no. 5026, p. 1399-1402.

Passchier, C. W., and Trouw, R. A., 2005, Microtectonics, Germany, Springer-Verlag, 366 p.:

Passchier, C. W., Zhang, J. S., and Konopásek, J., 2005, Geometric aspects of synkinematic granite intrusion into a ductile shear zone-an example from the Yunmengshan core complex, northern China: Geological Society of London Special Publication, v. 245, p. 65.

Paterson, S. R., Fowler, T. J., Schmidt, K. L., Yoshinobu, A. S., Yuan, E. S., and Miller, R. B., 1998, Interpreting magmatic fabric patterns in plutons: Lithos, v. 44, p. 53-82.

Paterson, S. R., Pignotta, G. S., and Vernon, R., 2004, The significance of microgranitoid enclave shapes and orientations: Journal of Structural Geology, v. 26, no. 8, p. 1465-1481.

Paterson, S. R., and Vernon, R., 1995, Bursting the bubble of ballooning plutons: A return to nested diapirs emplaced by multiple processes: Geological Society of America Bulletin, v. 107, no. 11.

Paterson, S. R., Vernon, R., and Othmar, T. T., 1989, A review of criteria for the identification of magmatic and tectonic foliations in granitoids: Journal of Structural Geology, v. 11, no. 3.

Pavlis, T. L., 1996, Fabric development in syn-tectonic intrusive sheets as a consequence of melt-dominated flow and thermal softening of the crust: Tectonophysics, v. 253, p. 1-31.

Pearce, J. A., Harris, N. B. W., and Tindle, A. G., 1984, Trace element discrimination diagrams for the tectonic interpretation of granitic rocks: Journal of Petrology, v. 25, no. 4, p. 956-983.

Petford, N., and Atherton, M. P., 1992, Granitoid emplacement and deformation along a major crustal lineament: the Cordillera Blanca, Peru: Tectonophysics, v. 205, no. 1, p. 171-185.

Petford, N., Cruden, A. R., McCaffrey, K. J. W., and Vigneresse, J. L., 2000, Granite magma formation, transport and emplacement in the Earth's crust: Nature, v. 408, p. 5.

Petford, N., Kerr, R. C., and Lister, J. R., 1993, Dike transport of granitoid magmas: Geology, v. 21, p. 845-848.

Petford, N., Lister, J. R., and Kerr, R. C., 1994, The ascent of felsic magmas in dykes: Lithos, v. 32, no. 1, p. 161-168.

Phillips, E. R., 1974, Myrmekite—one hundred years later: Lithos, v. 7, no. 3, p. 181-194.

Pitcher, W. S., 1975, On the rate of emplacement of batholiths: Journal of the Geological Society of London, v. 131, p. 587-591.

Pollard, D. D., 1973, Derivation and evaluation of a mechanical model for sheet intrusions: Tectonophysics, v. 19, no. 3, p. 233-269.

Pownall, J. M., Waters, D. J., Searle, M. P., Shail, R. K., and Robb, L. J., 2012, Shallow laccolithic emplacement of the Land’s End and Tregonning granites, Cornwall, UK: Evidence from aureole field relations and P-T modeling of cordierite-anthophyllite hornfels: Geosphere, v. 8, no. 6, p. 1467-1504.

Pryer, L. L., and Robin, P.-Y. F., 1996, Differential stress control on the growth and orientation of flame perthite: a palaeostress-direction indicator: Journal of Structural Geology, v. 18, no. 9, p. 1151-1166.

Ramsay, J. G., 1989, Emplacement kinematics of a granite diapir: the Chindamora batholith, Zimbabwe: Journal of Structural Geology, v. 11, no. 1, p. 191-209.

Reches, Z. e., and Fink, J., 1988, The mechanism of intrusion of the Inyo Dike, Long Valley Caldera, California: Journal of Geophysical Research, v. 93, no. B5, p. 4321-4334.

Reed, J. C., Bickford, M. E., and Tweto, O. L., 1993, Proterozoic accretionary terranes of Colorado and southern Wyoming: in The Geology of North America, v. 2, p. 211-228.

Rickwood, P.C., 1989, Boundary lines within petrologic diagrams which use oxides of major and minor elements: Lithos, v. 22, no. 4, p. 247-263.

Rollinson, H. R., 1993, Using geochemical data: evaluation, presentation, interpretation.

Roman-Berdiel, T., Gapais, D., and Brun, J. P., 1995, Analogue models of laccolith formation: Journal of Structural Geology, v. 17, no. 9, p. 1337-1346.

Rosenberg, C. L., Berger, A. R., and Schmid, S. M., 1995, Observations from the floor of a granitoid pluton: Inferences on the driving force of final emplacement: Geology, v. 23, no. 5, p. 443-446.

Royden, L., 1996, Coupling and decoupling of crust and mantle in convergent orogens: Implications for strain partitioning in the crust: Journal of Geophysical Research, v. 101, no. B8, p. 17679-17617,17705.

Ryan, M. P., 1993, Neutral buoyancy and the structure of mid ocean ridge reservoir: Journal of Geophysical Research, v. 98, p. 22321-22338.

Saha, D., and Chakraborti, S., 2007, Advective heat transfer and fabric development in a shallow crustal intrusive granite—the case of Proterozoic Vellaturu granite, south India: Journal of Earth System Science, v. 116, no. 5, p. 433-450.

Scaillet, B., Pecher, A., Rochette, P., and Champenois, M., 1995, The Gangotri granite (Garhwal Himalaya): Laccolithic emplacement in an extending collisional belt: Journal of Geophysical Research, v. 100, no. B1, p. 585-607.

Schmidt, C. J., Smedes, H. W., and O'Neill, J. M., 1990, Syncompressional emplacement of the Boulder and Tobacco Root Batholiths (Montana USA) by pull-apart along old fault zones: Geological Journal, v. 25, p. 305-318.

Sederholm, J. J., 1923, On Migmatites and Associated Pre-Cambrian Rocks of Southwestern Finland: Pt. I. The Pellinge Region, US Government Printing Office.

Shaw, C. A., Heizler, M. T., and Karlstrom, K. E., 2005, (super 40) Ar/ (super 39) Ar thermochronologic record of 1.45-1.35 Ga intracontinental tectonism in the southern Rocky Mountains; interplay of conductive and advective heating with intracontinental deformation: American Geophysical Union Monograph, v. 154, p. 163-184.

Shaw, C. A., and Karlstrom, K. E., 1999, The Yavapai-Mazatzal crustal boundary in the southern Rocky Mountains: Rocky Mountain Geology, v. 34, no. 1, p. 37-52.

Shaw, C. A., Karlstrom, K. E., Williams, M. L., Jercinovic, M. J., and McCoy, A. M., 2001, Electron-microprobe monazite dating of ca. 1.71–1.63 Ga and ca. 1.45–1.38 Ga deformation in the Homestake shear zone, Colorado: Origin and early evolution of a persistent intracontinental tectonic zone: Geology, v. 49, no. 8.

Shervais, J. W., 2005, Quartz diorite and diorite plutons of the Elder Creek ophiolite, California: Fore-arc magmatism in a supra-subduction zone ophiolite, *in* Proceedings Geological Society of America Abstracts with Programs, Volume 37, p. 85.

Sibson, R. H., Moore, J. M., and Rankin, A. H., 1975, Seismic pumping - a hydrothermal fluid transport mechanism: Journal of the Geological Society of London, v. 131, p. 653-659.

Solar, G. S., Pressley, R. A., Brown, M., and Tucker, R. D., 1998, Granite ascent in convergent orogenic belts: Testing a model: Geology, v. 26, no. 8.

Srogi, L. A., and Lutz, T. M., 1997, Chemical variation in plutonic rocks caused by residual melt migration: Implications for granite pedogenesis: The Nature of Magmatism in the Appalachian Orogen, v. 191, p. 309.

Stevenson, C. T. E., Owens, W. H., Hutton, D. H. W., Hood, D. N., and Meighan, I. G., 2007, Laccolithic, as opposed to cauldron subsidence, emplacement of the Eastern Mourne pluton, N. Ireland: evidence from anisotropy of magnetic susceptibility: Journal of the Geological Society, London, v. 164.

Stipp, M., Stünitz, H., Heilbronner, R., and Schmid, S. M., 2002, The eastern Tonale fault zone: a ‘natural laboratory’ for crystal plastic deformation of quartz over a temperature range from 250 to 700 °C: Journal of Structural Geology, v. 24, no. 1861-1884.

Streckeisen, A., 1974, Classification and nomenclature of plutonic rocks recommendations of the IUGS subcommission on the systematics of igneous rocks: Geologische Rundschau, v. 63, no. 2, p. 773-786.

Takada, A., 1989, Magma transport and reservoir formation by a system of propagating cracks: Bulletin of Volcanology, v. 52, no. 2, p. 118-126.

-, 1990, Experimental study on propagation of liquid-filled crack in gelatin: shape and velocity in hydrostatic stress condition: Journal of Geophysical Research, v. 95, no. B6, p. 8471-8481.

Taylor, S. R., and McLennan, S. M., 1995, The geochemical evolution of the continental crust: Reviews of Geophysics, v. 33, no. 2, p. 241-265.

Tikoff, B., De Saint Blanquat, M., and Teyssier, C., 1999, Translation and the resolution of the pluton space problem: Journal of Structural Geology, v. 21, p. 1109-1117.

Tikoff, B., and Teyssier, C., 1992, Crustal-scale, en echelon" P-shear" tensional bridges: A possible solution to the batholithic room problem: Geology, v. 20, no. 10, p. 927-930.

Tikoff, B., and Vigneresse, J. L., 1999, Strain partitioning during partial melting and crystallizing felsic magmas: Tectonophysics, v. 312, p. 117-132.

Tobisch, O. T., McNulty, B. A., and Vernon, R., 1997, Microgranitoid enclave swarms in granitic plutons, central Sierra Nevada, California: Lithos, v. 40, p. 321-339.

Tweto, O. L., and Case, J. E., 1972, Gravity and magnetic features as related to geology in the Leadville 30-minute quadrangle, Colorado: USGS Professional Paper, v. 726-C, p. 1-31.

Tweto, O. L., and Sims, P. K., 1963, Precambrian ancestry of the Colorado mineral belt: Geological Society of America Bulletin, v. 74, no. 8, p. 991-1014.

Twiss, R. J., and Moores, E. M., 1992, Structural geology, W.H. Freeman.

Vanderhaeghe, O., 1999, Pervasive melt migration from migmatites to leucogranite in the Shuswap metamorphic core complex, Canada: control of regional deformation:

Tectonophysics, v. 312.

Vegas, N., Naba, S., Bouchez, J. L., and Jessell, M., 2008, Structure and emplacement of granite plutons in the Paleoproterozoic crust of Eastern Burkina Faso: rheological implications: International Journal of Earth Sciences, v. 97, no. 6, p. 1165-1180.

Vernon, R., 1991, Questions about myrmekite in deformed rocks: Journal of Structural Geology, v. 13, no. 9, p. 979-985.

-, 2000, Review of Microstructural Evidence of Magmatic and Solid-State Flow: Visual Geosciences, v. 5, no. 2, p. 1-23.

Vernon, R., Johnson, S., and Melis, E., 2004, Emplacement-related microstructures in the margin of a deformed pluton: the San Jose tonalite, Baja California, Mexico: Journal of Structural Geology, v. 26, no. 10, p. 1867-1884.

Vernon, R., Paterson, S. R., and Geary, E. E., 1989, Evidence for syntectonic intrusion of plutons in the Bear Mountains fault zone, California: Geology, v. 17, no. 8, p. 723-726.

Vigneresse, J. L., 1995, Crustal regime of deformation and ascent of granitic magma: Tectonophysics, v. 249, no. 3, p. 187-202.

Vigneresse, J. L., and Clemens, J. D., 2000, Granitic magma ascent and emplacement: neither diapirism nor neutral buoyancy: Geological Society, London, Special Publications, v. 174, no. 1, p. 1-19.

Vigneresse, J. L., Tikoff, B., and Améglio, L., 1999, Modification of the regional stress field by magma intrusion and formation of tabular granitic plutons: Tectonophysics, v. 302.

Wagner, R., Rosenberg, C. L., Handy, M. R., Möbus, C., and Albertz, M., 2006, Fracture-driven intrusion and upwelling of a mid-crustal pluton fed from a transpressive shear zone—The Rieserferner Pluton (Eastern Alps): Geological Society of America Bulletin, v. 118, no. 1, p. 219.

Weertman, J., 1971, Theory of water-flled crevasses in glaciers applied to vertical magma transport beneath oceanic ridges: Journal of Geophysical Research, v. 76, no. 5, p. 1167-1183.

Weertman, J., and Chang, S. P., 1977, Fluid flow through a large vertical crack in the Earth's crust: Journal of Geophysical Research, v. 82, no. 5, p. 929-932.

Whitmeyer, S. J., and Karlstrom, K. E., 2007, Tectonic model for the Proterozoic growth of North America: Geosphere, v. 3, no. 4.

Williams, M. L., and Karlstrom, K. E., 1996, Looping P-T paths and high-T, low-P middle crustal metamorphism: Proterozoic evolution of the southwestern United States: Geology, v. 24, no. 2.

Williams, M. L., Karlstrom, K. E., Lanzirotti, A., Read, A. S., Bishop, J. L., Lombardi, C. E., Pedrick, J. N., and Wingsted, M. B., 1999, New Mexico middle-crustal cross sections: 1.65-Ga macroscopic geometry, 1.4-Ga thermal structure, and continued problems in understanding crustal evolution: Rocky Mountain Geology, v. 34, no. 1.

Winter, J. D., 2001, An introduction to igneous and metamorphic petrology, Upper Saddle River, Prentice-Hall, 697 p.:

Wohletz, K., 2009, KWare Magma, ver. 2.49.0126, University of California.

Zibra, I., 2012, Syndeformational granite crystallisation along the Mount Magnet Greenstone Belt, Yilgarn Craton: evidence of large-scale magma-driven strain localisation during Neoarchean time: Australian Journal of Earth Sciences, v. 59, no. 5, p. 793-806.

Zoback, M. L., and Zoback, M. D., 1980, State of stress in the conterminous United States: Journal of Geophysical Research, v. 85, no. B11, p. 6113-6156.

APPENDICES

Appendix I

Samples collected during the 2010 field season; UTM zone 13N				Oriented surface				
Sample	**Location**	**Latitude**	**Longitude**	**Strike**	**Dip**	**Oriented surface is…**	**Rock type**	**Purpose of sample**
HBC10-1	Warner Pt	38.56754	107.76630	212	84SW	fol	pCqm	hs
HBC10-2	Warner Pt	38.57426	107.77115				pCqm?	hs
HBC10-3	Nelson Gulch	38.44738	107.45195	012	65SE	arb	pCa	ts
HBC10-4	Nelson Gulch	38.44733	107.45123				gnt+sil+bt gneiss	ps
HBC10-5	Nelson Gulch	38.44733	107.45123	020	66NW	fol	gnt+sil+bt gneiss	ps
HBC10-6	Nelson Gulch	38.44733	107.45123				Spotted Rk	hs
HBC10-7	CC: main W talus field	0288882	4258875				fol pCc	ts
HBC10-8	CC: pg 18	0289345	4258440				fol bt granite	hs
HBC10-9	CC: pg 18	0289345	4258440				peg	hs
HBC10-10A	Hermits Rest	0279982	4259672				gnt+sil+bt gneiss	ps
HBC10-10B	Hermits Rest	0279982	4259672				gnt+sil+bt gneiss	ts
HBC10-11	Hermits Rest	0279972	4259799	097	28SW	fol?	L > S pCc	chem, gc, ts; contrain relationship of CMG dikes to pluton
HBC10-12	CC: pg 18	0289268	4258622	296	76SW	arb	fol bt granite	ts, chem
HBC10-13	CC: bird shit wall	0289321	4258620	141	76SW	arb	pCc	ts
HBC10-14	CC: bird shit wall	0289321	4258620	257	55SW	orientation of contact	pCc	ts
HBC10-15	CC: bird shit wall	0289107	4257982	124	33SW	S2	bt gneiss	hs
HBC10-16	CC: bird shit wall	0289107	4257982	130	22SW	S2	bt gneiss	ts
HBC10-17	CC: bird shit wall	0289107	4257982	134	76SW	arb	bt granite	ts
HBC10-18	CC: lower 3	0288881	4258678	305	15NE	fol	fol pCc	ps, chem
HBC10-19	CC: across from lower bridge	0289068	4258593	206	90	fol	fol bt granite	hs
HBC10-20	CC: across from lower bridge	0289068	4258593	202	73NW	fol	fol bt granite	ts
HBC10-21	CC	0288695	4259495	304	77NE	orientation of dike	Lamp	ts
HBC10-22	CC	0288695	4259495	302	86NE	orientation of dike	Lamp	hs
HBC10-23	CC	0288695	4259495				Lamp	chem, gc; constrain age of lamprophyre: 1.4 or 1.7 Ga?
HBC10-24	CC	0288695	4259289	144	42SW	S2	pCgm	ts
HBC10-25	CC: w ridge	0287464	4258334				pCc	chem, ts
HBC10-26	CC: w ridge	0287607	4258499				Diabase	hs
HBC10-27	CC: creepy den	0289118	4258745				pCc/pCgm contact	hs
HBC10-28	CC: creepy den	0289118	4258745	295	90	fol	pCc/pCgm contact	hs
HBC10-29	CC	38°27'37.884	107°25'20.220"				Lamp	hs
HBC10-30	CC	38°27'37.884	107°25'20.220"				Spotted Rk	hs
HBC10-31	CC	38°27'37.884	107°25'20.220"				Lamp	hs
HBC10-32	CC: pg 12	0289365	4258430				pCc w/ pCgm	hs
HBC10-33	Blue Creek	0289262	4257052	261	50NW	fol	pCgm	ts
HBC10-34	Blue Creek	0289262	4257052				pCc	ts
HBC10-35	Boat tour	0289507	4258519	056	72SE	arb	Lamp	hs
HBC10-36	Boat tour	0289507	4258519	086	77SW	arb	pCc	ts
HBC10-37	Boat tour	0289507	4258519				pCc	ts
HBC10-38	Boat tour	0291001	4258465				pCc	chem
HBC10-39	Boat tour	0285486	4258064				pCc	chem, ts
HBC10-40	Boat tour	0285414	4258060	004	72NW	~orientation of dike	Lamp	hs
HBC10-41	Gateview	0317274	4244531				Thorium vien	hs
HBC10-42	Gateview	0318555	4236534				Carbonatite	hs
HBC10-43	Gateview	0217483	4239810				Pyroxenite	hs
HBC10-44	Gateview	0318647	4239337				Neph. Syenite	hs
HBC10-45	Gateview	0316985	4238186				Mag-il.-perovskite	hs
HBC10-46	CC	0289119	4258622	171	30SW	S2	pCgm	ts
HBC10-47	CC	0289119	4258622				pCc	hs
HBC10-48	CC	0288764	4259325	130	47SW	S2	pCgm	ts
HBC10-49	Above Chapeta Falls	0291124	4258423	015	10SE	arb	pCc	ts
HBC10-50	Above Chapeta Falls	0291122	4258432	247	30NW	S2	pCgm	hs
HBC10-51	Above Myers Gulch	0284598	4259100	184	25NW	S2	Spotted Rk	ts
HBC10-52	Above Myers Gulch	0284610	4259146	080	86NW		EW dike	chem, gc; constrain relationship of EW dikes: improve stress field switch model
HBC10-53	Blue creek	0289950	4255546	150	33SW	arb	fol bt granite	ts
HBC10-54	Blue Creek	0289850	4255620	084	84SE	arb	pCc/pCgm contact	ts
HBC10-55	CC: main W talus field	0288809	4258959				pCc	chem, gc, ts; representative CMG sample to get better pluton age
HBC10-56	CC: trail	0288874	4259275				pCc	hs

Abbreviations: CC, Curecanti Creek; pCqm, Precambrian quartz monzonite; pCa, amphibolite; gnt, garnet; sil, sillimanite; bt, biotite; Rk, rock; pCc, Curecanti monzogranite; peg, pegmatite; L, lineation; S, foliation; Lamp, lamprophyre; neph, nepheline; Mag., magnetite; il., ilmenite; pCgm, quartzofeldspathic migmatite and gneiss; arb, arbitrary; fol, foliation; und., undolose extinction.

Appendix II

Structural data collected in the Curecanti Needle area of the Black Canyon of the Gunnison

Collected during the 2010 and 2012 field seasons; UTM zone 13N

Outcrop	Latitude	Longitude	Strike	Dip	Plunge	Trend	Generatio	Description	Note
10m south of Page 18 outcrop	0289268	4258622		265 29NW				Biotite aggregate lenses with elongate garnet	
10m south of Page 18 outcrop	0289268	4258622		249 32NW				Biotite aggregate lenses with elongate garnet	
10m south of Page 18 outcrop	0289268	4258622		275 41NW				Biotite aggregate lenses with elongate garnet	
10m south of Page 18 outcrop	0289268	4258622		246 47NW				Biotite aggregate lenses with elongate garnet	
10m south of Page 18 outcrop	0289268	4258622		287 29NE				Biotite aggregate lenses with elongate garnet	
10m south of Page 18 outcrop	0289268	4258622		234 51NW				Biotite aggregate lenses with elongate garnet	
10m south of Page 18 outcrop	0289268	4258622		278 22NW				Biotite aggregate lenses with elongate garnet	
10m south of Page 18 outcrop	0289268	4258622		234 40NW				Biotite aggregate lenses with elongate garnet	
10m south of Page 18 outcrop	0289268	4258622		269 19NW				Biotite aggregate lenses with elongate garnet	
10m south of Page 18 outcrop	0289268	4258622		270 34NW				Biotite aggregate lenses with elongate garnet	
10m south of Page 18 outcrop	0289268	4258622		261 32NW				Biotite aggregate lenses with elongate garnet	
10m south of Page 18 outcrop	0289268	4258622		285 21NW				Curecanti/Pegmatite contact	
10m south of Page 18 outcrop	0289268	4258622		304 30NW				Pegmatite/migmatite contact	
10m south of Page 18 outcrop	0289268	4258622		354 22NE				Biotite aggregate lenses with elongate garnet	
Page 18 outcrop	0289268	4258622		259 57NW			S2	Foliation in migmatite	
Page 18 outcrop	0289268	4258622		264 49NW			S2	Foliation in migmatite	
Page 18 outcrop	0289268	4258622		355 10NE				Granite/migmatite contact	
Page 18 outcrop	0289268	4258622		201 24SE				Weak foliation of mica in granite	Questionable
Bird Shit Talus	0289321	4258620		14 84SE				Pegmatite on migmatite pavement	
Bird Shit Talus	0289321	4258620		186 88SE				Pegmatite on migmatite pavement	
Bird Shit Talus	0289321	4258620		175 34SW	292	30	S2	Migmatite pavement	
Bird Shit Talus	0289321	4258620		180 33W	290	30	S2	Migmatite pavement	
Bird Shit Talus	0289321	4258620		161 41W	281	36	S2	Migmatite pavement	
Bird Shit Talus	0289321	4258620		155 32SW	180	23	S2	Migmatite pavement	
Bird Shit Talus	0289321	4258620		145 26SW	286	19	S2	Migmatite pavement	
Bird Shit Talus	0289321	4258620		135 31SW	266	29	S2	Migmatite pavement	
Bird Shit Talus	0289321	4258620		173 38SW	270	37	S2	Migmatite pavement	
Bird Shit Wall	0289321	4258620		320 62NE			S2	Migmatite	
Bird Shit Wall	0289321	4258620		193 88NW				Garnet bearing pegmatite cutting Curecanti	
Bird Shit Wall	0289321	4258620		200 89NW				Garnet bearing pegmatite cutting Curecanti	
Bird Shit Wall	0289321	4258620		354 39NE				Curecanti/Migmatite contact	
Bird Shit Wall	0289321	4258620		340 61NE				Curecanti/Migmatite contact	
Lower Three - #2 (base of bird Shit Talus Contact)	0289068	4258593		330 35NE				Curecanti/Migmatite contact	
Lower Three - #2 (base of bird Shit Talus Contact)	0289068	4258593		332 40NE				Curecanti/Migmatite contact	
Lower Three - #2 (base of bird Shit Talus Contact)	0289068	4258593		321 30NE				Curecanti/Migmatite contact	
Lower Three - #2 (base of bird Shit Talus Contact)	0289068	4258593		196 30NW			S2	Migmatite	
Lower Three - #2 (base of bird Shit Talus Contact)	0289068	4258593		304 52NE				Curecanti/Migmatite contact	
Lower Three - #2 (base of bird Shit Talus Contact)	0289068	4258593		340 49NE				Curecanti/Migmatite contact	
Lower Three - #3 (lower bridge contact)	0289345	4258440		272 28NE				Curecanti/Migmatite contact	
Lower Three - #3 (lower bridge contact)	0289345	4258440		340 22NE				Curecanti/Migmatite contact	Questionable
Lower Three - #3 (lower bridge contact)	0289345	4258440		289 36NE				Curecanti/Migmatite contact	
North buttress of Bird Shit Talus	0289107	4257982	093	64SW				Pegmatite cutting migmatite	Pegmatite that cuts mig, cur, and screen in cur?
North buttress of Bird Shit Talus	0289107	4257982	092	41SW	091	6	S2	Migmatite	Pegmatite that cuts mig, cur, and screen in cur?
North buttress of Bird Shit Talus	0289107	4257982	095	65SW				Pegmatite cutting migmatite	Pegmatite that cuts mig, cur, and screen in cur?
North buttress of Bird Shit Talus	0289107	4257982		133 31SW	256	30	S2	Migmatite	Pegmatite that cuts mig, cur, and screen in cur?
Bird Shit Wall (main floor contact)	0289107	4257982		252 27NW				Curecanti/Migmatite contact	Near North buttress of Bird Shit Talus
Bird Shit Wall	0289321	4258620		216 90			G1?	25cm thick pegmatite dike cutting mig but being cut by Curecanti	Near North buttress of Bird Shit Talus
Bird Shit Wall	0289321	4258620		134 37NW	305	4	S2	Black bt rich schist with mineral lineation	Near North buttress of Bird Shit Talus
Bird Shit Wall	0289321	4258620		124 33SW	288	15	S2	Black bt rich schist with mineral lineation	Near North buttress of Bird Shit Talus
Bird Shit Wall	0289321	4258620		130 22Sw	275	20	S2	Black bt rich schist with G1 pegmatite injection vein	Peg coming from 216, 90 pegmatite

Appendix II (continued)

Outcrop	Latitude	Longitude	Strike	Dip	Plunge	Trend	Generatio	Description	Note
Bird Shit Wall	0289321	4258620	257	72NW				Foliated granite below main floor contact, related to Curecanti?	Questionable
Bird Shit Wall	0289321	4258620	330	82NE				Foliated granite below main floor contact, related to Curecanti?	Near North buttress of Bird Shit Talus
Lower Three - #3 (lower bridge contact)	0289068	4258593	304	34NE				Biotite aggregate lenses with elongate garnet	
Lower Three - #3 (lower bridge contact)	0289068	4258593	335	20NE				Curecanti-Migmatite contact	Questionable
Lower Three - #3 (lower bridge contact)	0289068	4258593	290	26NE				Weak foliation defined by bt in Curecanti	Questionable
Warner Point	38.56754	107.76630	218	76NW	216	26		Foliation in unknown granite	Phase of Pitts Meadow?
Warner Point	38.56755	107.76631	226	84SW	216	26		Foliation in unknown granite	Phase of Pitts Meadow?
Nelson Gulch	38.44733	107.45123			002	31	L2?	L-tectonite amphibolite	
Nelson Gulch	38.44734	107.45124			007	38	L2?	L-tectonite amphibolite	
Nelson Gulch	38.44735	107.45125			26	24	L2?	L-tectonite amphibolite	
Fold hinge below upper Curecanti Creek footbridge	0288695	4259495	251	39NW	328	26	S2	Foliation in migmatite	
Fold hinge below upper Curecanti Creek footbridge	0288695	4259495	249	39NW	340	34	S2	Foliation in migmatite	
Fold hinge below upper Curecanti Creek footbridge	0288695	4259495	229	44NW	340	38	S2	Foliation in migmatite	
Fold hinge below upper Curecanti Creek footbridge	0288695	4259495	219	30NW	295	30	S2	Foliation in migmatite	
Fold hinge below upper Curecanti Creek footbridge	0288695	4259495	39	39SE	140	36	S2	Foliation in migmatite	
Fold hinge below upper Curecanti Creek footbridge	0288695	4259495	70	43SE			S2	Foliation in migmatite	
Fold hinge below upper Curecanti Creek footbridge	0288695	4259495	64	36SE			S2	Foliation in migmatite	
Isoclinal "F1" on Curecanti Creek Trail	0288695	4259495	326	56NW	294	16	S2	Foliation in migmatite	
Isoclinal "F1" on Curecanti Creek Trail	0288695	4259495	330	47NW	295	22	S2/S3 inte	Foliation in migmatite	
Page 18 outcrop	0289345	4258440	319	24NE				Pegmatite/migmatite contact	
Page 18 outcrop	0289345	4258440	306	55NE				Biotite aggregate lenses with elongate garnet	
Page 18 outcrop	0289345	4258440	327	16NE				Biotite aggregate lenses with elongate garnet	
Page 18 outcrop	0289345	4258440	363	14NE				Biotite aggregate lenses with elongate garnet	
Page 18 outcrop	0289345	4258440	214	24SE				Biotite aggregate lenses with elongate garnet	
Hermits Rest Trail	0279982	4259672	148	47SW	155	32	S2	Gnt/sil/bt gneiss	
Hermits Rest Trail	0279982	4259672			148	28		Gnt/sil/bt gneiss	
Hermits Rest Trail	0279982	4259672			150	27		Gnt/sil/bt gneiss	
Hermits Rest Trail	0279982	4259672			157	23		L>S Curecanti	May have a foliation, but unable to measure
Hermits Rest Trail	0279982	4259672			150	21		L>S Curecanti	May have a foliation, but unable to measure
Hermits Rest Trail	0279982	4259672			162	13		L>S Curecanti	May have a foliation, but unable to measure
Hermits Rest Trail	0279982	4259672			161	22		L>S Curecanti	May have a foliation, but unable to measure
Hermits Rest Trail	0279982	4259672			160	32		L>S Curecanti	May have a foliation, but unable to measure
Hermits Rest Trail	0279982	4259672	89	82SE				Curecanti/Pegmatite contact	
Hermits Rest Trail	0279982	4259672	99	88SE				Curecanti/Pegmatite contact	
Hermits Rest Trail	0279982	4259672	111	28SW	161	22		L>S Curecanti	Foliation slightly suspect
Bird Shit Wall	0289107	4257982	320	62NE			S2	Foliation in migmatite	
Bird Shit Wall	0289107	4257982	193	83NW				Garnet bearing pegmatite cutting Curecanti	
Bird Shit Wall	0289107	4257982	200	89NW				Garnet bearing pegmatite cutting Curecanti	
Bird Shit Wall	0289107	4257982	157	57SW	258	56	S2	Foliation in migmatite	
Bird Shit Wall	0289107	4257982	171	38SW				Foliation in migmatite	
Bird Shit Wall	0289107	4257982	093	13NE				Pegmatite cutting migmatite and curecanti	
Very steep gully (pg 31 sketch)			240	14SE			S2	Foliation in migmatite	
Very steep gully (pg 31 sketch)			025	42SE			S2	Foliation in migmatite	
Very steep gully (pg 31 sketch)			153	46SW			S2	Foliation in migmatite	
Bird Shit Wall	0289107	4257982	124	33SW	288	15	S2	Foliation in migmatite	Well defined biotite mineral lineation
Bird Shit Wall	0289107	4257982	130	24SW	275	20	S2	Foliation in migmatite	Well defined biotite mineral lineation
Bird Shit Wall	0289107	4257982	330	82NE				Foliation in bt. Granite	Strike is +- 15 degrees
Lower Three - #3 (lower bridge contact)	0288695	4259495	305	15NE				Folation in Curecanti	Awesome sample of foliated Curecanti
Lower Three - #3 (lower bridge contact)	0288695	4259495	295	45NE				Biotite aggregate lenses with elongate garnet	Awesome sample of foliated Curecanti
Just off the edge of Pioneer Lookout	0288695	4259289	281	75NE				Curecanti/migmatite contact	

Appendix II (continued)

Outcrop	Latitude	Longitude	Strike	Dip	Plunge	Trend	Generatio	Description	Note
Just off the edge of Pioneer Lookout	0288695	4259289	280	85NE				Curecanti/migmatite contact	
Just off the edge of Pioneer Lookout	0288695	4259289	251	33NW	305	32	S2	Foliation in migmatite	
Just off the edge of Pioneer Lookout	0288695	4259289	216	51NW	305	51	S2	Foliation in migmatite	
Just off the edge of Pioneer Lookout	0288695	4259289	242	47NW	315	45	S2	Foliation in migmatite	
Across the river from lower bridge	0289068	4258593	206	90				Foliation in bt. Granite	
Across the river from lower bridge	0289068	4258593	202	73NW				Foliation in bt. Granite	
Offset veinlets near top of Curecanti Creek Trail	0288695	4259289	152	69SE	325	32	S2	Foliation in migmatite	
40m above upper bridge (west slope)	0288695	4259289	155	42SW	195	31	S2	Foliation in migmatite	Aluminous schist w/ good macro shear sense indicators
Curecanti Creek Trail	0289118	4258745	187	39NW	324	31	S2	Foliation in migmatite	
Curecanti Creek Trail	0289118	4258745	188	39NW			S2	Foliation in migmatite	
Curecanti Creek Trail	0289118	4258745	167	43SW	324	27	S2	Foliation in migmatite	
Curecanti Creek Trail	0289118	4258745	120	61SW			S2	Foliation in migmatite	
Curecanti Creek Trail	0289118	4258745	120	64SW			S2	Foliation in migmatite	
Curecanti Creek Trail	0289118	4258745	174	49SW	290	44	S2	Foliation in migmatite	
Curecanti Creek Trail	0289118	4258745	174	49SW	315	27	S2	Foliation in migmatite	
Curecanti Creek Trail	0289118	4258745	170	50SW	295	43	S2	Foliation in migmatite	Lineation uncertain
Curecanti Creek Trail	0289118	4258745	201	52NW			S2	Foliation in migmatite	
Curecanti Creek Trail	0289118	4258745	180	44W			S2	Foliation in migmatite	
Curecanti Creek Trail	0289118	4258745	280	68NE			S2	Foliation in migmatite	
Curecanti Creek Trail	0289118	4258745	145	52SW			S2	Foliation in migmatite	
Curecanti Creek Trail	0289118	4258745	148	48SW	294	28	S2	Foliation in migmatite	
Page 32 Gully	0289365	4258430	182	47NW	281	45	S2	Foliation in migmatite	
Page 32 Gully	0289365	4258430	160	61SW	272	56	S2	Foliation in migmatite	
Page 32 Gully	0289365	4258430	148	49SW			S2	Foliation in migmatite	
Page 32 Gully	0289365	4258430	148	57SW			S2	Foliation in migmatite	
Page 32 Gully	0289365	4258430	204	49NW	290	49	S2	Foliation in migmatite	
Page 32 Gully	0289365	4258430	207	29NW			G1?	Discordant pegmatite, agmatic texture	Bt. Schlieren present
Page 32 Gully	0289365	4258430	180	39W			S2	Foliation in migmatite	
Page 32 Gully	0289365	4258430	142	40SW	273	37	S2	Foliation in migmatite	
Page 32 Gully	0289365	4258430	173	56SW	281	49	S2	Foliation in migmatite	
Scary Den Outcrop - Curecanti Creeek	0289118	4258745	130	19SW			S2	Foliation in migmatite	S>>L
Scary Den Outcrop - Curecanti Creeek	0289118	4258745	070	39SE			S2	Foliation in migmatite	S>>L
Scary Den Outcrop - Curecanti Creeek	0289118	4258745	165	26SW			S2	Foliation in migmatite	S>>L
Scary Den Outcrop - Curecanti Creeek	0289118	4258745	076	44SE			S2	Foliation in migmatite	S>>L
Scary Den Outcrop - Curecanti Creeek	0289118	4258745	084	33SE			S2	Foliation in migmatite	S>>L
Scary Den Outcrop - Curecanti Creeek	0289118	4258745	185	43NW			S2	Foliation in migmatite	S>>L
Scary Den Outcrop - Curecanti Creeek	0289118	4258745	200	48NW			S2	Foliation in migmatite	S>>L
Scary Den Outcrop - Curecanti Creeek	0289118	4258745	211	49NW			S2	Foliation in migmatite	S>>L
Scary Den Outcrop - Curecanti Creeek	0289118	4258745	041	27SE			S2	Foliation in migmatite	S>>L
Scary Den Outcrop - Curecanti Creeek	0289118	4258745	133	30SW			S2	Foliation in migmatite	S>>L
North of Curecanti Creek Trail	0288695	4259495	170	51SW			S2	Foliation in migmatite	
North of Curecanti Creek Trail	0288695	4259495	188	40NW			S2	Foliation in migmatite	
North of Curecanti Creek Trail	0288695	4259495	199	61NW			S2	Foliation in migmatite	
North of Curecanti Creek Trail	0288695	4259495	223	63NW			S2	Foliation in migmatite	
North of Curecanti Creek Trail	0288695	4259495	236	49NW	324	49	S2	Foliation in migmatite	
North of Curecanti Creek Trail	0288695	4259495	299	90			S2	Foliation in migmatite	
North of Curecanti Creek Trail	0288695	4259495	131	56SW			S2	Foliation in migmatite	
North of Curecanti Creek Trail	0288695	4259495	135	53SW	311	14	S2	Foliation in migmatite	
North of Curecanti Creek Trail	0288695	4259495	131	88NW			S2	Foliation in migmatite	
North of Curecanti Creek Trail	0288695	4259495	112	90			S2	Foliation in migmatite	

Appendix II (continued)

Outcrop	Latitude	Longitude	Strike	Dip	Plunge	Trend	Generatio	Description	Note
W Blue Creek Curecanti Pavement	0289262	4257052	287	84NE			G2?	Pegmatite feeder	
W Blue Creek Curecanti Pavement	0289262	4257052	256	69NW			G2?	Pegmatite feeder	
W Blue Creek Curecanti Pavement	0289262	4257052	275	85NE			G2?	Pegmatite main	
W Blue Creek Curecanti Pavement	0289262	4257052	276	87NE			G2?	Pegmatite main	
W Blue Creek Curecanti Pavement	0289262	4257052	277	90			G2?	Pegmatite feeder	
W Blue Creek Curecanti Pavement	0289262	4257052	292	84NE			G2?	Pegmatite main	
W Blue Creek Curecanti Pavement	0289262	4257052	264	90			G2?	Pegmatite main	
W Blue Creek Curecanti Pavement	0289262	4257052	299	84NE			G2?	Pegmatite feeder	
W Blue Creek Curecanti Pavement	0289262	4257052	275	82NE			G2?	Pegmatite feeder	
W Blue Creek Curecanti Pavement	0289262	4257052	268	90			G2?	Pegmatite feeder	
W Blue Creek Curecanti Pavement	0289262	4257052	270	90			G2?	Pegmatite main	
W Blue Creek Curecanti Pavement	0289262	4257052	261	89NE			G2?	Pegmatite feeder	
W Blue Creek Curecanti Pavement	0289262	4257052	277	90			G2?	Pegmatite feeder	
W Blue Creek Curecanti Pavement	0289262	4257052	299	84NE			G2?	Pegmatite feeder	
W Blue Creek Curecanti Pavement	0289262	4257052	269	84NW			G2?	Pegmatite main	
W Blue Creek Curecanti Pavement	0289262	4257052	046	31SE				Biotite aggregate	
W Blue Creek Curecanti Pavement	0289262	4257052	061	51SE				Biotite aggregate	
W Blue Creek Curecanti Pavement	0289262	4257052	170	79SW				Biotite aggregate	
W Blue Creek Curecanti Pavement	0289262	4257052	035	74SE				Biotite aggregate	
W Blue Creek Curecanti Pavement	0289262	4257052	290	50NE				Biotite aggregate	
W Blue Creek Curecanti Pavement	0289262	4257052	310	86NE				Biotite aggregate	
W Blue Creek Curecanti Pavement	0289262	4257052	295	59NW				Biotite aggregate	
W Blue Creek Curecanti Pavement	0289262	4257052	040	27SE				Biotite aggregate	
Boat tour: near Pioneer Pt. lamprophyre	0285414	4258060	156	40NE			S2	Foliation in migmatite	
Boat tour: near Pioneer Pt. lamprophyre	0285414	4258060	110	46NE			S2	Foliation in migmatite	
W ridge of Curecanti Creek	0287607	4258499	187	46NW			S2	Foliation in qtzfld migmatite	
W ridge of Curecanti Creek	0287607	4258499	195	46NW			S2	Foliation in qtzfld migmatite	
W ridge of Curecanti Creek	0287607	4258499	206	37NW			S2	Foliation in qtzfld migmatite	
W ridge of Curecanti Creek	0287607	4258499	199	57NW			S2	Foliation in qtzfld migmatite	
W ridge of Curecanti Creek	0287607	4258499	227	26NW			S2	Foliation in qtzfld migmatite	
W ridge of Curecanti Creek	0287607	4258499	255	20NW			S2	Foliation in qtzfld migmatite	
W ridge of Curecanti Creek	0287607	4258499	256	20NW	305	29	S2	Foliation in qtzfld migmatite	
W ridge of Curecanti Creek	0287607	4258499			305	22	G1?	Axis of boudin neck	
W ridge of Curecanti Creek	0287607	4258499	260	30NW	307	20	S2	Foliation in qtzfld migmatite	
W ridge of Curecanti Creek	0287607	4258499	223	10NW			S2	Foliation in pearly migmatite	
Pioneer Point pavement	0288874	4259275	197	66NW	309	60	S2?	Foliation in nebulitic migmatite	
Pioneer Point pavement	0288874	4259275	090	90			G2?	4cm pegmatite vein	
Pioneer Point pavement	0288874	4259275	272	60NE			S2?	Foliation in nebulitic migmatite	
Pioneer Point pavement	0288874	4259275	338	83NE				Lamprophyre dike	
Pioneer Point pavement	0288874	4259275	107	90			G2?	5cm pegmatite vein	
Pioneer Point pavement	0288874	4259275	121	69SW			G2?	3cm pegmatite vein	
Pioneer Point pavement	0288874	4259275	200	65NW			S2?	Foliation in nebulitic migmatite	
Pioneer Point pavement	0288874	4259275	105	83SE			G2?	3cm pegmatite vein	

Appendix III

Thin section summary for samples collected in the Curecanti Needle area of the Black Canyon of the Gunnison

Collected during the 2010 and 2012 field seasons; UTM zone 13N

Sample	Location in pluton	Geographic location	Latitude	Longitude	Strike	Dip	Rock type	Major mineral	Accesory minerals	Note	Def. mech	Def. T °C
HBC10-25	Core	West ridge of CC	0287464	4258334			CMG	qtz, plg, k-spar, musc, gnt, bt	monazite, oxides	Kinked musc. and fld	BLG	280-400
HBC10-4	Host rock	West side of Nelson Gulch	38.44733	107.45123			pCgm	qtz, plg, k-spar, gnt, bt, sil	monazite, oxides		Beer-foam	>500
HBC10-39	Roof of pluton	East side of Nelson Gulch	0285486	4258064			CMG	qtz, k-spar, plg, bt	monazite	Brittle fractures filled with qtz; very complex grain boundaries	GBM	>500
HBC10-34	Roof of pluton	West ridge of BC	0289262	4257052			CMG	qtz, k-spar, plg, bt, gnt	monazite	Brittle fractures filled with qtz; relatively simple grain boundaries	submag	
HBC10-36	Floor of pluton	Confluence of CC and MPR	0289507	4258519			CMG	qtz, k-spar, plg, bt, musc, gnt	monazite, oxides	Relatively simple grain boundaries	BLG	280-400
HBC10-37	Floor of pluton	Confluence of CC and MPR	0289507	4258519			CMG	qtz, k-spar, plg, bt, musc, gnt	monazite, oxides	Myrmekite	BLG	280-400
HBC10-18A	CMG subpluton dike	Lower CC	0288881	4258678	305	15NE	CMG	qtz, k-spar, plg, bt, gnt	monazite, oxides	Bulging grain boundaries, fine grain mantling	BLG	280-400
HBC10-18B	CMG subpluton dike	Lower CC	0288881	4258678	orthogonal to A		CMG	qtz, k-spar, plg, bt, gnt	monazite, oxides	Enclave wedge convex toward CMG; euhedral plg; magmatic	BLG; magmatic	280-400
HBC10-18C	CMG subpluton dike	Lower CC	0288881	4258678	orthogonal to B		CMG	qtz, k-spar, plg, bt, gnt	monazite, oxides	Polygonal grains away from enclave; subhedral gnt; gnt grows over fol; flame perthite; myrmekite	magmatic	
HBC10-38	Floor of pluton	Chipeta Falls	0291001	4258465			CMG	qtz, k-spar, plg, bt		Poikilitic k-spar; plg embayed by qtz	BLG, undulose	280-400
HBC10-49	Roof of pluton	Chipeta Falls	0291124	4258423			CMG	qtz, k-spar, plg, bt	monazite, oxides	Complex grain boundaries; fractured plg; complex grain boundaries	submag; GBM	>500
HBC10-14	Floor of pluton	CC	0289321	4258620	257	55SW	CMG/pCgm	qtz, k-spar, plg, bt		Fractured qtz and plg filled with qtz/clay; myrmekite; simple grain boundaries	undulose	>280
HBC10-11	CMG dike	Hermit's Rest trail	0279972	4259799	097	28	pCqm	qtz, k-spar, musc, bt	monazite		SGR	400-500
HBC10-13	Floor of pluton	CC	0289321	4258620	141	76	CMG	qtz, k-spar, musc, bt	monazite	Thin section preserves floor contact of pluton	BLG	280-400
HBC10-3	Host rock	Nelson Gulch	38.44738	107.45195	012	65SE	amph	hbl, qtz, bt, plg		Bt defines C fabric, hbl defines S fabric		
HBC10-5	Host rock	Nelson Gulch	38.44733	107.45123	020	66NW	pCgm	bt, gnt, sil, qtz, fld	monazite		SGR	400-500
HBC10-9	Pegmatite	CC	0289345	4258440			pCp	bt, qtz, fld, k-spar		Border phase pegmatite on CMG dike below pluton (i.e. HBC10-18)	SGR	400-500
HBC10-12	Bt granitoid	CC	0289268	4258622	296	76SW	CMG	bt, qtz, fld, k-spar		Border phase bt granitoid on CMG dike below pluton (i.e. HBC10-18)		
HBC10-32	CMG dike	CC	0289365	4258430			CMG/pCgm	bt, qtz, fld, k-spar			BLG	280-400
HBC10-33	Host rock	BC	0289262	4257052	261	50NW	pCgm	bt, qtz, fld, k-spar	monazite	Ameaboidal qtz	GBM	>500
HBC10-52	Pegmatite	Myers Gulch	0284610	4259146	080	86NW	EW peg	qtz, k-spar, fld		Myrmekite	undeformed?	
HBC10-51	Host rock	Myers Gulch	0284598	4259100	184	25NW	amph	hbl, qtz, bt, plg		"Spotted rock"		>500
HBC10-21	Lamprophyre		0288695	4259495	304	77NE	lamp	hbl, bt, plg, qtz		amph fol. Grows over porphyroblasts		>500
HBC10-19	Host rock		0289068	4258593			bt grantoid	qtz, plg, k-spar, bt				>500
HBC10-46	Host rock		0289119	4258622	171	30SW	pCgm	qtz, plg, k-spar, bt	monazite			>500
HBC10-48	Host rock		0288764	4259325	130	47SW	pCgm	qtz, plg, k-spar, bt				>500

VITA

Gordon “Donnie” Leonard Hicks III was born in St. Louis Park, Minnesota, in May 1987 to Sandra K Hicks and Gordon Leonard Hicks Jr. He attended St. Louis Park High School, where he studied abroad in Germany for one semester, and graduated in 2005. He then attended The University of Minnesota, Morris, where he studied abroad in Scotland for one semester and graduated in 2009 with a Bachelors of Arts in Geology. He engaged in multiple undergraduate research projects, including a glacier volume survey using differential GPS in northern Sweden, and a mapping project of Proterozoic quartzite exposures in Phantom Canyon, Colorado. He began to pursue his Masters of Science at The University of Tennessee, Knoxville in August 2009. While at UT, he has the opportunity to be part of a structural geology team (including Micah Jessup and Bob Hatcher) that served as a great resource and phrontisterion. Gordon spent summer 2010 and 2012 performing MS-based research in the Black Canyon of the Gunnison region of Colorado.